Substrate-Dependence of the Ice Premelting at Heterogeneous Interfaces: An X-Ray Scattering Study

Von der Fakultät Mathematik und Physik der Universität Stuttgart zur Erlangung
der Würde eines Doktors der Naturwissenschaften (Dr. rer. nat.) genehmigte
Abhandlung

Vorgelegt von
SEBASTIAN PETER FERDINAND SCHÖDER
aus Stuttgart

Hauptberichter:	Prof. Dr. H. Dosch
Mitberichter:	Prof. Dr. J Wrachtrup
Eingereicht am:	9. Oktober 2007
Tag der mündlichen Prüfung:	7. April 2008

Institut für Theoretische und Angewandte Physik der Universität Stuttgart

2007

Contents

Deutsche Zusammenfassung

Eis Grenzflächen befinden sich überall in unserer Umgebung. Trotzdem ist ihre molekulare Struktur nur in groben Zügen verstanden. Dies liegt am hohen Dampfdruck von Eis, denn viele Techniken zur Untersuchung von Oberflächen benötigen ein sehr gutes Vakuum. Der hohe Dampfdruck macht die Verwendung dieser Methoden schwierig oder unmöglich. Bei Temperaturen, die dem Schmelzpunkt nahe kommen, nimmt auch die Dynamik der Eis Oberfläche stark zu. Weiterhin ist es schwierig Eisoberflächen zu präparieren und bei Normalbedingungen zu stabilisieren. Das Zusammenspiel dieser Eigenschaften führt dazu, dass das strukturelle Verhalten von Eisoberflächen bis heute nur ungenügend verstanden ist.

Oberflächenschmelzen ist ein Phänomen bei dem die ersten atomaren oder molekularen Schichten einer Kristalloberfläche an Ordnung verlieren wenn die Temperatur dem Schmelzpunkt nahe kommt. Bei den meisten Festkörpern wurde dieses Phänomen zumindest auf einigen Kristallfacetten nachgewiesen. Die Temperatur, bei der diese Unordnung einsetzt, wird als *Einsetztemperatur* bezeichnet. Die Dicke der ungeordneten Schicht wächst mit der Temperatur und divergiert bei Erreichen des Volumenschmelzpunktes des Festkörpers. Da sie räumlich auf wenige Nanometer eingeschränkt ist und Teile der Kristallstruktur erhalten bleiben können, verhält sich die Schicht nicht wie eine Volumenflüssigkeit. Ihre Eigenschaften sind daher unbekannt. Aus diesem Grund wird die Schicht auch als *quasi-flüssige* Schicht bezeichnet. Der mathemtaische Zusammenhang zwischen Schichtdicke und Temperatur wird als Wachstumsgesetz bezeichnet. Je nach Art der zwischen den Grenzflächen wirkenden Kräfte wächst die Schicht mit einem logarithmischen Wachstumsgesetz (kurzreichweitige Kräfte) oder mit einem Potenzgesetz (langreichweitige Kräfte).

Das Oberflächenschmelzen von Eis wurde zuerst 1860 von Michael Faraday beschrieben [1]. Dieses Phänomen wurde seither mit vielen weiteren Methoden untersucht. Heute ist seine Existenz allgemein unumstritten. Aufgrund der oben beschriebenen Probleme bei der Untersuchung von freien Eisoberflächen ist das quantitative Verhalten allerdings noch immer undurchsichtig. Verschiedene Gruppen und Methoden liefern stark unterschiedliche Werte für die Dicke der quasi-flüssigen Schicht bei bestimmten Temperaturen.

Noch weniger ist über das Verhalten von tief vergrabenen Grenzflächen bekannt, denn nur wenige experimentelle Methoden können diese Grenzflächen erreichen. In der vorliegenden Arbeit wurde die Reflektivität hochenergetischer Röntgenstrahlung benutzt um das Problem der begrenzten Eindringtiefe zu umgehen. Bei Reflektivitätsmessungen wird die Intensität eines an einer Grenzfläche reflektierten Röntgenstrahles als Funktion des vertikalen Impulsübertrages gemessen. Die Form der Reflektivitätskurve hängt vom Elektronendichteprofil senkrecht zur Grenzfläche ab. Dieses Elektronendichteprofile kann durch Inversionsalgorithmen, wie dem Parratt oder dem Master Formalismus, aus der Reflektivitätsmessung abgeleitet werden. Reflektivitätsmessungen werden gewöhnlich bei Röntgenenergien bis zu 20 keV eingesetzt. Um verborgene Grenzflächen zu beobachten sind allerdings höhere Energien erforderlich, da diese eine größere Eindringtiefe aufweisen.

Hochenergie-Reflektivitätsexperimente stellen hohe Ansprüche an die Genauigkeit und Stabilität der Positionierung von Probe und Detektor. Zu diesem Zweck wurde eine spezielle Messstation zur Streuung an Grenzflächen an der Europäischen Synchrotronstrahlungsquelle (ESRF) in Grenoble aufgebaut [2]. Das Instrument erlaubt es den für molekulare Auflösung nötigen hohen Impulsübertrag zu erreichen. Da die Reflektivität zu hohen Impulsüberträgen stark abfällt, ist es nötig unerwünschte Untergrundsignale stark zu unterdrücken. Diese wurde durch Fokussierung des Primärstrahles auf wenige Mikrometer erreicht. Damit ist im Idealfall ein dynamicher Bereich von zehn Größenordnungen in der Reflektivität zugänglich. Die für die Messungen nötige Brillanz steht derzeit nur am Hochenergiemessplatz ID15 der ESRF zur Verfügung.

Grenzflächen, die mit dieser Technik untersucht werden sollen, müssen eine sehr hohe Qualität aufweisen. Die mikroskopische Rauigkeit der Grenzfläche muss unkorreliert und deutlich unter 10 Å liegen. Die Oberfläche muss zudem komplett flach sein. Bereits leichte Krümmungen der Grenzfläche können dazu führen, dass eine quantitative Auswertung der Daten nicht mehr möglich ist. Hohe Anforderungen werden auch an die Qualität des Eises gestellt. Von der Verwendung polykristallinen Eises wurde abgesehen, da es nicht möglich war Proben mit ausreichender Reinheit und Reproduzierbarkeit herzustellen. Aus diesem Grund wurden Einkristalle verwendet, die von Jörg Bilgram (ETH Zürich) zur Verfügung gestellt wurden. Bei den für diese Arbeit verwendeten Proben wird das Substrat mit einem speziellen Verfahren in den Eiskristall eingeschmolzen. Dadurch soll die Kristallstruktur an der Grenzfläche so gut wie möglich erhalten bleiben und die Eigenschaften der Grenzfläche möglichst reproduzierbar sein.

Simon Engemann untersuchte bereits das Grenzflächenschmelzen von Eis in Kontakt mit dem natürlich gewachsenem SiO_2 auf Silizium (111) und (100) Oberflächem mit hochenergetischer Röntgenreflektivität [3]. Grenzflächenschmelzen konnte an diesen Grenzflächen nachgewiesen werden. Die quasi-flüssige Schicht weist eine überraschend hohe Dichte von $1.2\rho_{water}$ auf und ihre Dicke wächst bei steigender Temperatur mit einem logarithmischen Wachstumsgesetz. Die in dieser Doktorarbeit präsentierten Experimente bauen auf dieser Arbeit auf. Um den Einfluss der chemischen und morphologischen Eigenschaften des Substrates auf das Grenzflächenschmelzen besser zu verstehen, wurden Substrate mit verschiedenen Eigenschaften und aus unterschiedlichen Materialien verwendet.

Insgesamt wurden elf Proben im Rahmen dieser Arbeit untersucht. Nur in zwei Fällen konnte Grenzflächenschmelzen beobachtet werden. In den anderen Fällen wurde es zwar nicht nachgewiesen, kann aber auch nicht ausgeschlossen werden, da eine quasi-flüssige Schicht nur dann nachgewiesen werden kann, wenn sich ihre Dichte deutlich von der des umgebenden Eises unterscheidet. In einigen Fällen ist die Qualität der Daten nicht ausreichend um das Vorhandensein einer ungeordneten Schicht mit von Eis verschiedener Dichte auszuschließen.

Die Substrate, bei denen Grenzflächenschmelzen nachgewiesen wurde, waren aus einkristallinem Quartz und hoch reinem Silikatglas präpariert. In beiden Fällen wurde für die quasi-flüssige Schicht eine Dichte von $1.25\rho_{water}$ gefunden, welche gut mit der von Engemann et al. gemessenen Dichte überein stimmt. Bei Bestrahlung der Proben mit hohen Röntgnedosen wuchs die Dicke der ungeordneten Schicht an. Der Grund für dieses Wachstum ist unbekannt. Die Schichtdicke wächst etwa 11 Å pro 10^9 Gy Strahlendosis an der Eis-Glas Grenzfläche. An der Eis-Quartz Grenfläche wird der doppelte Wert beobachtet. Die Schichtdicke kann für nicht bestrahlte Proben extrapoliert werden. Leider kann das strahlungsinduzierte Wachstum nur ungenau bestimmt werden. Dadurch ergeben sich große Fehlerbereiche für die Schichtdicken nach Korrektur der Bestrahlungseffekte.

Durch diese Fehler ist es nicht möglich festzustellen ob die Schichtdicke logarithmisch oder mit einem Potenzgesetz anwächst. Da frühere Experimente an ähnlichen Systemen logarithmisches Wachstum feststellten, wurde auch in dieser Arbeit ein Gesetz der Form

$$L = \xi \ln \left(\frac{T_O}{(T_M - T)} \right) , \tag{1}$$

angenommen. Dabei beschreibt ξ die Korrelationslänge in der quasi-flüssigen Schicht, T_O die Einsetztemperatur (vom englischen *onset*) und T_M den Schmelzpunkt von Eis. Für die Eis-Glas Grenzfläche wurde eine Korrelationslänge von $\xi_{silica} = 5$ Å und eine Einsetztemperatur von $T_{O,silica} = -9$ °C bestimmt. Die Korrelationslänge der Eis-Quartz Grenzfläche ist mit $\xi_{quartz} = 7$ Å etwas höher. Ein großer Unterschied besteht in der Einsetztemperatur, die bei der Eis-Quartz Grenzfläche mit $T_{O,quartz} = -1$ °C deutlich höher ausfällt. Dies lässt darauf schließen, dass die Struktur des Substrats das Grenzflächenschmelzen beeinflußt. Die kristalline Quartzoberfläche stabilisiert möglicherweise das Eiskristallgitter und unterdrückt somit die Entstehung einer ungeordneten quasi-flüssigen Schicht.

Die Schicht erscheint daher erst bei höheren Temperaturen und weist eine größere Korrelationslänge auf.

Es ist bemerkenswert, dass in allen Reflektivitätsstudien die selbe hohe Dichte für die quasi-flüssige Schicht gemessen wird. Diese Dichte entspricht der von amorphem Eis sehr hoher Dichte (VHDA, aus dem englischen *very-high-density amorphous*; Dichte $\rho_{VHDA} = 1,25\rho_{water}$ [4]). Eine Dichteerhöhung dieser Größenordnung kann nicht durch Spannungen oder Verunreinigungen im Eis erklärt werden. Die wahrscheinlichste Erklärung ist, dass die Wassermoleküle in der quasi-flüssigen Schicht eine neue Wasserphase mit hoher Dichte bilden. In Wassereinschlüssen in Nanometer Grössenordnung in Zeoliten wurden bereits Wasserphasen hoher Dichte beobachtet [5]. Die Tatsache, dass die von uns gefundene Wasserphase die selbe Dichte aufweist wie VHDA deutet darauf hin, dass sie auch eine ähnliche Struktur besitzt. Einige moderne Theorien für Wasser [6] gehen davon aus, dass Wasser einen zweiten kritischen Punkt bei einer Temperatur von etwa 220 K aufweist. Unterhalb dieser Temperatur existieren möglicherweise zwei Wasserphasen, eine mit hoher (HDW) und eine mit niedriger (LDW) Dichte. Die Eigenschaften von Wasser bei Normalbedingungen sind demnach durch starke Dichtefluktuationen zwischen beiden Zuständen bestimmt. Es gibt daher Anlass zu Spekulationen ob die dichte Wasserphase in Einschlüssen stabilisiert werden kann. Die Resultate der Reflektivitätsmessungen können in diese Richtung interpretiert werden.

Der Schwachpunkt der vorgeliegenden Arbeit ist, dass es nicht möglich war die gemessenen Resultate zu reproduzieren. Viele der untersuchten Grenzflächen zeigten kein Grenzflächenschmelzen, selbst wenn ein Substrate verwendet wurde, welches identisch mit einem war, an welchem zuvor eine quasi-flüssige Schicht gefunden wurde. Zum Beispiel wurde eine zweite Eis-Silikatglas Grenzfläche gemessen, bei der kein Grenzflächenschmelzen beobachtet werden konnte. Es muss daher gefolgert werden, dass die Probenpräparation nicht reproduzierbar genug ist. Noch verwirrender ist eine zweite Tatsache. Die Eis-Silikatglas Grenzfläche, bei der Grenzflächenschmelzen beobachtet wurde, zeigte bei einem zweiten Experiment fünf Monate später kein solches Verhalten mehr. Dank des Strahlenschadens im Eis vom vorherigen Experiment war es möglich auf der selben Stelle der Probe zu messen, so dass räumliche Inhomogenitäten als Erklärung für diese Diskrepanz ausgeschlossen werden können. Daraus muss geschlossen werden, dass weitere unbekannte Parameter das Grenzflächenschmelzen beeinflussen. Leider konnten diese Parameter in der vorliegenden Arbeit nicht identifiziert werden. Die Experimente an der Eis-Silikatglas Grenzfläche zeigen aber, dass sie (oder ein Teil von ihnen) zeitabhängig sein müßen.

Es ist wahrscheinlich, dass die Wassermoleküle eine gewisse Beweglichkeit benötigen um die Struktur der quasi-flüssigen Schicht anzunehmen. Diese ist in natürlichen Grenzflächen immer hoch genug, da deren Rauigkeit groß ist und sich viele Verunreinigungen im Eis befinden. Im Gegensatz dazu sind die Grenzflächen der in dieser Arbeit verwendeten Proben fast perfekt. Fehlstellen im Kristall, die die Beweglichkeit der Moleküle erhöhen können, werden allerdings durch die Probenpräparation erzeugt, wenn das Substrat in den Eiskristall geschmolzen wird. Die zusätzlichen Verspannungen und Defekte, die dadurch erzeugt werden, reichen möglicherweise aus, um zusammen mit dem Strahlenschaden die Bildung einer quasi-flüssigen Schicht zu begünstigen. Zwischen den beiden Experimenten, die an der Eis-Silikatglas Grenzfläche durchgeführt wurden, wurde diese für fünf Monate bei 16 K unter dem Schmelzpunkt gelagert. Die Lagerung bei hohen Temperaturen kann dazu führen, dass Fehlstellen ausgeheilt und Verspannungen in der Probe abgebaut werden. Aus diesem Grund ist die Mobilität der Eismoleküle im zweiten Experiment geringer und eine quasi-flüssige Schicht erhöhter Dichte kann nicht mehr aufgebaut werden.

Offensichtlich sind weitere Untersuchungen notwendig um das Grenzflächenschmelzen von Eis zu verstehen. Am wichtigsten ist es bessere Methoden zur Probenpräparation zu finden. Dies kann zum Beispiel durch Kondensation von Wassermolekülen aus der Gasphase geschehen. Desweiteren ist es nötig die Bestrahlungszeiten zu verringern. Da Strahlenschäden eine große Fehlerquelle darstellen sollten die Synchrotronstrahlungsexperimente mit Methoden kombiniert werden, die keine ionisierenden Strahlen verwenden. Weitere Einblicke könnten von Experimenten an der Grenzfläche von Eis und organischen Flüssigkeiten (zum Beispiel Heptan) gewonnen werden. In diesen Experimenten könnte die Oberflächenstruktur des Eises mit Röntgenbeugung unter streifendem Einfall (Grazing incidence diffraction) beobachtet werden, da Eis eine höhere Dichte als Heptan hat. Dadurch lässt sich eine evaneszente Welle im Eis anregen. An der Eis-Dampf Grenzfläche werden diese Experimente durch Artefakte gestört, die von Sublimation und Kondensation an der Eisoberfläche kommen. Diese Artefakte können durch den Kontakt mit einer hydrophoben organischen Flüssigkeit vermieden werden.

Chapter 1

Introduction

Ice, and its liquid form water, belong to the most common materials on earth. 70% of the surface of the earth is covered with oceans and 10% of the land mass is covered with ice. These ice layers can reach depths of several kilometers. They contain most of the freshwater on earth. The melting and freezing points of ice are within the environmental conditions that we experience. The landmasses have been shaped by the transitions of liquid water to ice and vapor. The phase transitions of water are the only phase transitions most people ever experience. The climate of the earth critically relies on the distribution of the three phases of water. The beauty of snow flakes and winter landscapes has been admired by many artists.

Ice interfaces play an important role in the life of most humans. The first time a child forms a snowball, it makes use of the unique properties of the ice surface. Countless road accidents happen each year due to the low friction of ice surfaces. On the other hand, the low friction of ice and snow surfaces has lead to the growth of a huge winter sport industry. The strong adhesion of ice cause huge amounts of money and chemicals to be spend in order to defrost airplanes. In cold climates, infrastructure and buildings are damaged by frost heave. Even in warm climates, the physics and chemistry of ice surfaces impacts atmospheric chemistry, leading to dramatic phenomena, like thunderstorms.

Although interfaces of water and ice are omnipresent in our day-to-day life, their molecular structure is still under debate. One example is the disordering of the surface at temperatures close to the melting transition. This phenomenon, known as surface melting or premelting of ice, was long ago predicted by Michael Faraday [1]. Since then, many techniques have been used to investigate premelting on the solid-vapor interface of ice. Although this phenomenon is still hardly understood, the existence of surface melting of ice is accepted in the scientific community. Investigating the solid-solid interface of ice is much harder. However, for many processes in engineering and nature, this is the more important case. Unfortunately, until recently there were no experimental methods available to measure the interface melting of ice accurately.

X-ray reflectivity has become a standard tool for analyzing electron density profiles perpendicular to the surface of a sample. The advent of 3rd generation synchrotron sources made it possible to extend this method for the investigation of previously inaccessible systems, such as buried interfaces. High energy x-ray beams with focal spot sizes of only a few microns are needed to measure reflectivity curves with the quality needed for data analysis. Such experiments require high quality of the reflecting interface as well as the positional and angular accuracy and stability of the diffractometer.

The interface melting of ice has been investigated for the first time with high energy x-ray reflectivity in the course of the PhD thesis of Simon Engemann [3]. Its presence could be confirmed at the solid-solid interface of ice and silicon dioxide. The obtained reflectivities were of high quality and the results reproducible. The goal of the work presented here was to deepen the insight into premelting of ice by investigating the influence of different substrate properties. For this reason many different substrates were used, to observe the influence of chemistry, morphology, hydrophobicity and impurities. In the same time, the experimental technique was continuously improved by a better understanding of the substrate properties necessary for collecting high quality data and the development of better data collection and analysis techniques.

The second chapter of this thesis will discuss the physical properties of ice and its interface. It is also giving an overview over the work that has been done so far on this topic. The following chapter will explain the experimental method used. In the fourth chapter the sample preparation, experimental setup and data analysis is explained. The results of the measurements done for this thesis are shown in chapter 5 and discussed in chapter 6. The thesis ends with conclusions and outlook in chapter 7.

Chapter 2

Ice

The purpose of this chapter is to give an overview over the physical properties of ice that are important for this work and the work that has been done so far on the premelting of ice. At first the structure of the water molecule and the ice lattice, as well as the defects within, will be discussed. Then the special properties of the ice interface will be highlighted. The phenomenon, that is most important for this thesis, is the interface melting of ice. The theoretical work done on this topic will be described in section 5, followed by a section that describes the different results that are obtained by different experimental techniques. The last chapter discusses the environmental impact of interface melting of ice.

2.1 The water molecule

From the structural point of view, the water molecule is very simple. It consists of an oxygen atom that is covalently bound to two hydrogen atoms. The distance of an O—H bond is 0.9572 Å. The angle between the two O—H bonds is 104.52°[7]. Due to the big difference in electronegativity between the oxygen and the hydrogen atoms the water molecule exhibits a strong dipole moment of $6.186 \cdot 10^{-30}$ Cm (1.8546 debye) [8].

The high electronegativity of the oxygen atom allows the water molecule to form hydrogen bonds. In this type of bond the hydrogen stays covalently bound to one oxygen atom and forms a much weaker and longer length bond with another oxygen atom. The molecule to which the hydrogen atom is covalently bonded is sometimes called the “proton donor”, while the other molecule is called the “proton acceptor”. Each water molecule can accept and donate two protons. Since the acceptor sites are located in directions tetrahedrally opposite to the donor sites this produces tetrahedral bonding around the oxygen atom.

Although the water molecule has a very simple structure it can form an amazing wealth of different phases. Today we know 15 crystalline phases of ice. Water also shows polyamorphism. This is the ability to form more than one amorphous structure. The best overview over the crystalline and amorphous structures of ice can be found in [9]. Even the structure of liquid water is complicated and not solved (see the review paper of B. Winter and M. Faubel [10] and references therein).

There is only one ice phase that is stable under environmental conditions on earth. This phase is called iceIh. The other phases are out of the scope of this work. In the next section the structure of this phase will be discussed in detail.

2.2 IceIh

IceIh is the only stable solid phase of ice that can be found in the environment. The roman number has been introduced by Tammann [11] after the discovery of high pressure phases of ice. Until today ice phases are named with roman numbers which indicate the chronological order of the phase's discovery. The “h”, which stands for hexagonal, is usually added to distinguish it from the metastable cubic phase Ic.

The structure of ice has first been proposed by Pauling [12]. To understand it is helpful to consider the oxygen lattice and the hydrogen lattice separately. The oxygen atoms form a hexagonal lattice with the ’wurtzite’ structure. Each oxygen atom has four nearest neighbors at the corners of a regular tetrahedron. This leads to the formation of puckered rings perpendicular to the c-axis. The stacking order of this layers is *ABABAB*... This sequence resembles those of hexagonal close-packed metals. The lattice parameters are a = 4.519 Å and c = 7.357 Å at -20 °C.

While the oxygen atoms form a well ordered lattice there is no long-range order in the hydrogen network. Instead the hydrogen atoms follow the so called ice rules.

1. Each oxygen atom is covalently bound to two hydrogen atoms.
2. There is exactly one hydrogen atom per bond.

The first rule is a consequence of the structure of the water molecule which is the basic building block of the ice crystal. The second rule is a consequence of the hydrogen bond, which consists of a proton acceptor and a proton donor (see section 2.1). In a real ice crystal these rules are not always satisfied. This leads to protonic point defects (see next section).

Pauling realized that all the possible hydrogen configurations satisfying the ice rules are nearly equal in energy. At normal temperatures there is no configuration that is stabilized. This disorder gives ice an excess entropy. It was first experimentally discovered by Giauque and Ashley [13]. Pauling deviced his model to account for this and calculated the zero-point entropy $S_0 = 3.371 J\,(Kmol)$, which is in good agreement with the experiments.

It is possible to describe the ice structure with the average structure. In this model each bonding place is occupied by half a hydrogen atom. The space group of this average structure is P6_3/mmc. The average structure of IceIh is shown in Fig. 2.1.

At temperatures below 72 K the ordered phase of ice is stabilized [14]. It is called iceXI. It has an orthorhombic structure of space group Cmc2_1 [15] [16]. In reality this structure can not be obtained for pure ice since the mobility of the water molecules is too low to change to the new structure.

Recent theoretical work [17] has shown that above a critical temperature the proton lattice can undergo a phase transition into a completely disordered state, in which the ice rules are not valid anymore. The protons are distributed randomly over the possible lattice sites. For bulk ice this transition temperature lies above the melting point, so that it can not be observed. However, it is possible that this disordered phase appears in the vicinity of the ice interface (see section 2.5.2 for more detail).

2.3 Protonic point defects

Protonic point defects are defects that are special to ice. They are generated when one of the ice rules is broken. They have been first discovered by Bjerrum [18]. Breaking the first ice rule results in charged ions. These types of defects are therefore called ionic defects. When one proton jumps from its ideal lattice position to a neighboring oxygen atoms two defects are created. The former atom misses its proton and turns to an OH^- ion. The second oxygen atom has now an additional proton and turns to H_3O^+.

Special to ice are rotational defects. These are created when a water molecule is rotated on its ideal lattice position. This results in a violation of the second ice rule since now there is one empty bond and one bond with two protons. Empty bonds are called L-defects (from the German word “leer”). Double occupied bonds are called D-defects (from “doppelt”). Rotational defects are called Bjerrum defects. The model of a completely empty bond or a bond with two protons is highly oversimplified. In reality these defects encompass large perturbations of the lattice around them [19] [20].

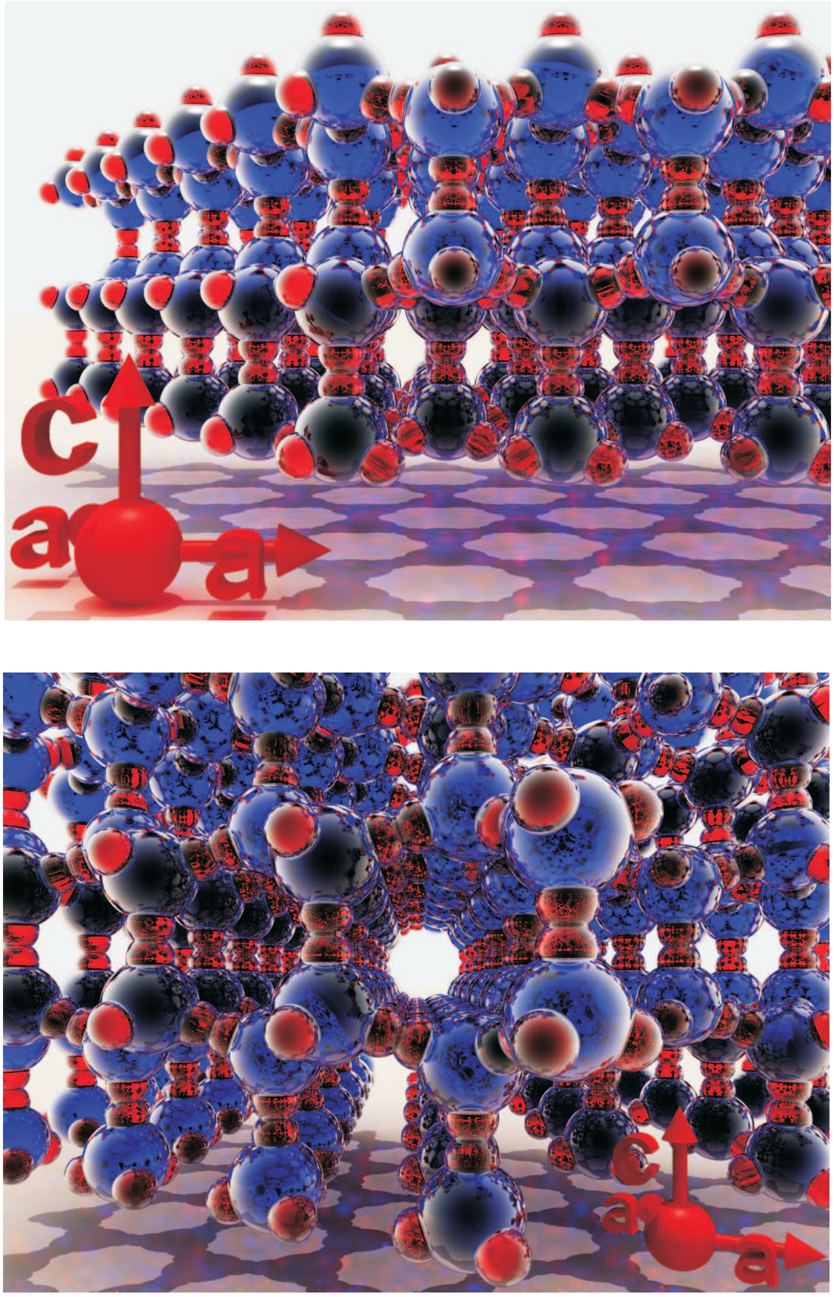

Figure 2.1: The average structure of IceIh. The blue spheres are oxygen atoms, while each red sphere stands for 1/2 average hydrogen atoms. The crystal lattice is shown from the $(10\bar{1}0)$ (top image) and the $(2\bar{1}\bar{1}0)$ (bottom image) direction. The illumination is parallel to the (0001) direction. This way the shadow on the bottom of the images depicts the projection of the lattice onto the basal plane.

2.4 The ice interface

The surface of ice has been under investigation almost since the advent of scientific culture in the western world. Already Descartes made observations about snowflakes and deduced the importance of the surface properties of ice [21]. Today the structure and the processes taking place on ice surfaces and interfaces remain unclear. This is partly because of the high vapor pressure of ice, which renders the application of most surface techniques impossible and partly because the results of surface experiments depend critically on the sample preparation and purity.

Experiments have shown that the surface of ice is positively charged. Petrenko showed in slider experiments [22] that the surface charge of polycrystalline ice is $q = \frac{Q}{A} \approx +1.6 \cdot 10^{-2}\ Cm^{-2}$. Petrenko and Colbeck confirmed this result for natural snow in an interesting field experiment where alpine skis where used as a probe [23]. The experimental findings correspond well with a model proposed by Fletcher [24]. Due to electrical interactions it is energetically more favorable for the main part of the water molecules to orientate themselves with the protons pointing out of the ice. Since the bulk ice is uncharged there must be a subsurface layer with a high amount of rotational disorder of the water molecules to screen the surface charge. Dosch et al. confirmed the existence of this layer by surface x-ray diffraction [25].

As the temperature of the surface approaches the melting point the first molecular layers of the crystal become disordered and loose their long-range order. This disordered layer is called a quasi-liquid layer. The phenomenon is called interface melting (or in the special case of the free surface melting) or premelting. The thickness of this layer increases as the temperature is raised to the melting point. In the following subsection model descriptions for the quasi-liquid layer will be discussed. Then, experimental evidence will be shown for the premelting at free surfaces and the solid-ice interfaces. The section will close with some remarks about the importance of this phenomenon for technical and environmental processes.

2.5 Theory of interface melting

At the beginning of this section it might be helpful to clearly define what is meant by interface melting. Under the definition of premelting fall all phenomena where part of the material forms a liquid equilibrium phase inside the solid region of the bulk phase diagram. This excludes non-equilibrium effects like supercooling, but includes premelting due to confinement and curvature. But in this work the term interface melting will be used to describe premelting effects that occur due to the presence of a non-curved interface. The material that is in contact with the ice will contain only one half space and therefore not confine the ice in any way. In the case that the other material is a gas or vacuum the term surface melting is also used.

Interface melting is a phenomenon that is not unique to ice. On the contrary, most materials show interface melting on some of their facets. Most of the fundamental work done on premelting has been done in the study of liquid metals. However this work will focus on the interface melting of ice. For works done on other systems see [26] and [27]. A recent theoretical work introduced a thermodynamical theory valid for all materials [28].

Obviously, premelting and melting are closely related. The microscopic mechanism that leads to melting is not clearly understood. Today it seems that the interface of a solid plays an important part as acting as a nucleus for the melting process. The *Lindemann criterion* [29, 30] states that melting starts when the root-mean-displacement of the molecules reaches approximately 15% of the intermolecular distance. Since the molecules at the surface, which lack up to half of their neighbors, are more loosely bound, they have much higher root-mean-displacements than bulk molecules at the same temperature. This implies that the Lindemann criterion is fulfilled much earlier for the interface layers. Of course the Lindemann criterion is an oversimplified view of the melting process. But it shows the importance of the interface contribution. The fact, that it is possible to supercool liquids, but very difficult to superheat solids, supports this idea. The few cases in which it has been possible to superheat solids are experiments in which the properties of the solid interface have been changed (for example by applying special coatings).

Interface melting can be complete or incomplete. It is called incomplete, or blocked, when the thickness of the premolten layer saturates at a finite thickness. The interface melting is complete when the layer thickness goes to infinity upon reaching the bulk melting temperature. Since this is assumed to be the "normal" case, the "complete" is most of the time dropped. In this work the term "interface melting" will refer to complete melting and in cases of blocked melting behavior we will use the term "incomplete interface melting".

2.5.1 Phenomenological theory

This theory describes the melting process by thermodynamic properties, i.e. the material is considered from a macroscopic viewpoint and as a continuum. Clearly, this theory must fail for layers with a thickness of just a few monolayers.

Solids that are wet by their own melt posses lower surface energy for the wet surface than for the dry surface. The wet surface consists of two interfaces. The solid-liquid interface and the liquid-vapor interface. For a solid surface to be wet by its own melt,

$$\gamma_{SV} \geq \gamma_{SL} + \gamma_{LV} \tag{2.1}$$

must be fulfilled. γ_{SV} is the free energy per area for the solid-vapor interface and γ_{SL}, γ_{LV} are the free energies per area for the solid-liquid and the liquid-vapor interfaces, respectively. In this case the free energy of the solid can be reduced by melting the first monolayers and thereby covering the surface with a quasi-liquid layer. For this process the latent heat of melting has to be procured. At temperatures close to the melting point this can still result in a reduction of the free energy of the solid.

The free energy per area, f, for a solid wet by a quasi-liquid layer is

$$f(L) = \gamma_{SQ} + \gamma_{QV} + LQ_m\rho_{qll}\frac{(T_M - T)}{T_M}. \tag{2.2}$$

Here, T is the temperature, T_M the bulk melting temperature, L is the thickness of the quasi-liquid layer, ρ_{qll} is its density, Q_m the latent heat of melting and γ_{SQ}, γ_{QV} the surface energies per area for the solid-quasi-liquid and the quasi-liquid-vapor interfaces. Note the approximation in Eq. 2.2 that the latent heat of melting is the same for the solid/quasi-liquid transition as for the solid/bulk liquid transition.

Since the physical properties of the quasi-liquid layer are different from a bulk liquid, the quantities γ_{SQ} and γ_{QV} are unknown. To replace them with the known surface energies γ_{SL} and γ_{LV} a certain structure of the disordered layer has to be assumed. Since there are no structural models for the quasi-liquid layer it will be assumed that the structure is that of a bulk liquid that still “feels”, due to its thinness, the underlying crystal lattice. Therefore it carries some of the properties of the solid and its physical properties will be in between those of a bulk liquid and a solid. The relevant order parameters for the melting transition are the Fourier components Ψ_i of the density having the periodicity of the crystal lattice. $\Psi_i = 1, i > 1$ for a perfectly ordered crystal and $\Psi_i = 0, i > 1$ for the completely disordered liquid. The free energy per area for the quasi-liquid-vapor interface γ_{QV} lies between the value for the liquid-vapor interface γ_{LV} and the dry interface γ_{SV}.

$$\gamma_{QV} = \gamma_{LV} + \Psi\left(\gamma_{SV} - \gamma_{LV}\right) \tag{2.3}$$

Similarly, the surface free energy per area for the solid-quasi-liquid interface γ_{SQ} will be smaller than the value of the solid-liquid interface γ_{SL}.

$$\gamma_{SV} = \left(1 - \Psi\right)\gamma_{SL} \tag{2.4}$$

For short-range forces, which have been shown to dominate in ice (see section 2.6), the order parameter decays exponentially with the correlation length ξ

$$\Psi = e^{-L/\xi}. \tag{2.5}$$

Substituting these values into Eq. 2.2, we get

$$f(L) = \gamma_{SL} + \gamma_{LV} + LQ_m\rho_{qll}\frac{(T_M - T)}{T_M} + (\gamma_{SV} - \gamma_{LV} - \gamma_{SL})\, e^{-L/\xi}. \tag{2.6}$$

The growth law of the premolten layer is obtained by minimizing Eq. 2.6 with respect to L.

$$\frac{\partial f}{\partial L} = LQ_m\rho_{qll}\frac{(T_M - T)}{T_M} - \frac{\Delta\gamma}{\xi}e^{-L/\xi} = 0 \tag{2.7}$$

with $\Delta\gamma = \gamma_{SV} - \gamma_{LV} - \gamma_{SL}$. This yields the growth law

$$L = \xi \ln\left(\frac{\Delta\gamma T_M}{\xi Q_M \rho_{qll}(T_M - T)}\right). \tag{2.8}$$

By introducing the onset temperature

$$T_O = \frac{T_M\Delta\gamma}{\xi Q_M\rho_{qll}} \tag{2.9}$$

at which the premelting starts, one can rewrite the growth law in a more simple way

$$L = \xi \ln\left(\frac{T_O}{(T_M - T)}\right). \tag{2.10}$$

From Eq. 2.9 it is clear that interface melting can only occur for materials where $\Delta\gamma = \gamma_{SV} - \gamma_{LV} - \gamma_{SL}$ is greater than zero. This is the constraint that the solid has to be wet by its own melt that we formulated in Eq. 2.1. Note that the interfacial free energies per area vary for the different facets of a crystal. This means that some of the facets of a crystal show interface melting and others not. In the case of ice it has been shown that the thickness of the premolten layer is much smaller on non-basal facets [31].

Recent experiments [3] have shown that for large layer thicknesses the system changes from short-range forces to van der Waals type forces. The same is expected for systems with a large amount of impurities [32]. In this case the order parameter decays with a power law. This leads to an algebraic growth law

$$L(T) \propto (T_M - T)^{-1/(n+1)}. \tag{2.11}$$

The exponential n depends on the type of interaction with $n = 2$ for non-retarded and $n = 3$ for retarded van der Waals forces.

2.5.2 Other theoretical approaches

Ice, with its network forming hydrogen bonds, is a very complex system. Hence, many theoretical methods used to investigate less complicated systems, like metals, fail for ice.

Electrical interactions

One of the first theoretical predictions for the surface melting of ice has been given by Fletcher [33]. He analyzed the electrical interactions between the water molecules. As shown in section 2.1, the water molecule features a strong dipole moment. There is no long range order in the hydrogen network and therefore in the orientation of the water molecules. Therefore the orientation of the dipole moment of the water molecules at the ice surface should be statistical. Half of the dipole moments will have a component reaching out of the surface, while the other half has a component reaching into the crystal.

The water molecule is not a symmetrical dipole and its electrical polarizability has quadratic nonlinearities. Because of this, the energy associated with both orientations of the surface water dipoles is not the same. The surface lowers its energy by adopting a structure where the main part of the surface molecules orient themselves with their protons pointing out of the ice surface, hence leading to the surface charge of ice (see section 2.4). This reorientation is only possible inside a disordered surface film.

Fletcher concludes that the transformation of the surface into a disordered, but orientationally polarized, quasi-liquid layer is favorable at temperatures between -30 °C to -13 °C and the bulk melting point. The thickness of the layer is in the order of “tens of angströms” close to the melting point.

Dispersion forces

Elbaum and Schick have applied the theory of dispersion forces to premelting [34]. A quasi-liquid layer can only form if the dry surface is wet by its own melt (see section 2.5.1). The Dzyaloshinskii-Lifshitz-Pitaevskii method used by the authors connects this constraint with the polarizablility of the material. The polarizability of water is favorable to interface melting at thin film thicknesses but suppresses it for large thicknesses, where retardation effects start to become important. Hence interface melting is incomplete. The maximum thickness for the quasi-liquid layer is 36 Å. Fluctuations can increase this value but can not change the scenario to complete wetting.

The DLP method was also used to evaluate substrate effects for premelting at the ice-solid interface [35]. It turns out that interface melting is favorable when the polarizability of the quasi-liquid layer lies between that of ice and the substrate. Unfortunately their paper deals mostly with the effect of van der Waals interactions. Recent experiments favor that the dominant interactions in pure ice are of short range nature [3]. Only for very thick quasi-liquid layers long range forces seem to dominate. Consequently, the layer thicknesses calculated by the theory are much smaller than the experimental values.

As the theory treats the premolten layer from a macroscopic point of view it is not applicable to very thin layer thicknesses.

Pressure melting

Another mechanism, unique to ice, was presented by Makkonen [36]. The density of ice is lower than the density of water. Therefore ice shows pressure melting. Increasing the pressure reduces the melting point of ice. The molecules in bulk ice are in a force equilibrium. The surface molecules miss half of their neighbors and therefore feel a net force pulling them into the bulk. The pressure resulting from this force is calculated and compared with the melting point reduction resulting from pressure melting.

According to the calculations the onset temperature of premelting is -13 °C. Note that this premelting mechanism is not limited to systems that are wet by their own melt but to all systems that show pressure melting. In the same publication contact angle data are presented that indicate that ice is non-wetting. In this case most other theoretical approaches cannot explain the premelting. However, it remains unclear if the contact angle data can be extrapolated to equilibrium conditions.

Thermodynamical theories

Henson et al. presented a thermodynamical theory that can treat all sorts of materials [28] and discussed the consequences specifically for ice [37]. They observed that the growth law for different materials falls into two groups if their layer thicknesses are not plotted against the temperature but against the chemical activity

$$x = \frac{P_{solid}}{P_{liquid}} \tag{2.12}$$

of the premolten layer, with the solid sublimation pressure P_{solid} and the liquid vaporization pressure P_{liquid}. One group contains all atomic materials, like metals, while the other contains all molecular materials, like organic molecules and ice. The thickness of the quasi-liquid layer is calculated using a lattice gas in the grand canonical ensemble. The calculated thickness agrees well with published results on ice. It is interesting to note that the theory does not contain any adjustable parameters. Note also that in this theory the quasi-liquid layer is thermodynamically identical to bulk water.

Proton disorder

Ryzhkin and Petrenko showed [17] that the proton sublattice can undergo a phase transformation into a completely disordered state. In this phase the protons do not follow the ice rules, but are randomly placed in the lattice. For bulk ice this phase transformation occurs at temperatures above the bulk melting point.

In a second work [38] this theory was applied to the interface of ice. In the case of a semi-infinite crystal there is a region close to the interface in which the order parameter is reduced. The phase transformation occurs therefore at lower temperatures. This leads to a region of complete hydrogen disorder at the interface of ice. The interface phase transformation temperature is approximately -30 °C. However, only the hydrogen lattice becomes disordered at this temperature. At higher temperatures this disorder can lead to the melting of the oxygen sublattice. In this model the premolten layer consists of two layers. A layer of complete disorder, which is closer to the normal definition of the quasi-liquid layer, and a second layer underneath where only the protons are disordered.

Molecular dynamics simulation

One of the first molecular dynamics simulations on ice was done by Weber and Stillinger [39], the melting behavior of clusters of 250 water molecules in contact with a potential wall was investigated. The water molecules were simulated in the ST2 potential, which treats them as rigid asymmetric rotors with hydrogen bonding. The simulation was able to reproduce the bulk structure of ice. Upon increasing the temperature in the simulation, melting was observed. The clusters started to melt at the surface and the melting front moved inwards.

In a later work Kroes [40] examined premelting at an infinite ice (0001) surface, employing the more advanced TIP4P model for the water molecules. This model features positive charges at the hydrogen atoms and a negative charge at the oxygen atom. Dispersion and short-range repulsion between the molecules is described by a Lennard-Jones potential, which is centered on the oxygen atom. The ice surface was modeled with several layers of fixed water molecules as a bulk substrate on which twelve layers of unrestrained water molecules were placed. The simulation results confirmed that melting starts at the surface of the ice. The mobility of the water molecules is greatly increased while the order parameters are reduced. This effect is strongest in the top layer and decays toward deeper layers. The disordered layers do not become completely liquid-like, but remain with some of their solid properties.

Simulations on similar systems have been done by Nada and Furukawa [41], employing a modified TIP4P potential and eleven layers of water molecules on top of a fixed ice lattice. In addition to the basal surface of ice, the properties of the prism surface were investigated. The onset temperature is higher on the prism face and the thickness of the premolten layer is smaller than on the basal face. These observations agree well with experiments.

Note, that all of these simulations neglect quantum effects, which have been shown to play a role in ice [42]. Unfortunately, only quantum mechanical simulations of bulk systems exist, showing that the simulated melting temperature can shift by about 80 K when including quantum effects [42].

2.6 Experimental evidences of interface melting of ice

A lot of experimental work has been carried out to find interface melting effects, mainly on metals. For an overview see [26, 27, 43]. In contrast, only few experiments have been performed on the premelting of ice leading to very different results depending on the experimental technique and the physical quantity that is probed in the experiment. An overview about the work done on ice surfaces can be found in [9] and [44]. Most of the work has been done on the free surface of ice and only very few experiments have investigated buried interfaces.

2.6.1 Ellipsometry

In ellipsometry linear polarized light is reflected from the probed interface (for a short introduction see [45]). The ratio of the complex Fresnel coefficients of reflection for light polarized parallel (R_p) and perpendicular (R_s) to the incident plane contains the information about the sample

$$\rho = \frac{R_p}{R_s}. \tag{2.13}$$

ρ is called the ellipticity. In the experiment the relative amplitude attenuation of the reflection $\tan\Psi$ and the relative phase shift Δ are measured. They are related to the sample properties by

$$\rho = \tan\Psi \cdot e^{(i\Delta)}. \tag{2.14}$$

Equation 2.14 can be solved analytically only for pure substrates. For more complex systems models are employed where the free parameters are fitted to the data. It is possible to determine film thicknesses from 1 Å to 100 μm with this method with an accuracy as high as 0.1 Å [45]. Ellipsometry is one of the few interface techniques that can be used to investigate buried interfaces provided that one of the solid materials is transparent for light. Although ice is transparent at optical wavelengths, it has been impossible to prepare the ice surface with a quality that is high enough to allow the beam to penetrate from the ice side. This limits ellipsometry measurements to investigations of transparent solid-ice interfaces.

Furukawa et al. [46] used ellipsometry to investigate the surface melting of ice at the basal and prism planes of ice. A strong change in the relative phase shift at –4 °C for the prism face and at –2 °C for the basal plane was found which was addressed to the formation of a transition layer. The change in the refraction index was not strong enough to determine the growth law quantitative. The layer thickness grows with increasing temperature. The index of refraction of the transition layer is close to the value of water.

Beaglehole and Wilson [47] performed ellipsometry measurements on the ice-glass interface, with ice single-crystals frozen onto plates of float glass. The float glass plates were treated in different ways before freezing the ice to them. Using clean and smooth glass substrates no interface melting was detected. A change in ρ was found only for temperatures higher than -0.005 °C, but this vanished for etched glass plates. Therefore the authors concluded that there is no evidence for premelting at smooth and clean glass interfaces.

Some glass substrates were roughened by etching in HF/nitric acid solutions. Subsequent characterization with AFM shows height fluctuations of 40 Å. Freezing these plates onto the ice samples, premelting could be detected at temperatures higher than –5 °C. A power-law type growth-law with an exponent of –2 was found. The thickness of the molten layer is 1000 Å at –1 °C.

Another set of premelting experiments were performed with glass substrates contaminated with salt (NaCl). Changes in the ellipticity were found for temperatures higher than –1 °C to –2 °C. Since the index of refraction of water changes with increasing amount of impurities, modeling of the data is very difficult. Treating the premolten layer as bulk water and using the tabulated refraction index the thickness of the premolten region was calculated for three temperatures. From these they derive a power-law growth with an exponent of –1.

Finally, a rough glass substrate covered by a thick hydrophobic layer was investigated. No change in the ellipticity was found. However, when the experiment was repeated with a smooth hydrophobic glass substrate some evidence for premelting was found. This was somewhat contradictory since interface melting was not expected for smooth substrates.

There are some limitations to ellipsometry measurements that have to be taken into account. Ideally it is possible to probe layer thicknesses in the sub-nanometer regime. However, the ice-quasi-liquid layer interface hardly presents such conditions. The refractive index of water is close to exhibit of ice but the quasi-liquid layer is not expected to have the properties of bulk water. One has to assume that the index of refraction will be between the value for ice and water. Another strong assumption is that the quasi-liquid layer is well-defined with a uniform index of refraction. It is much more likely that the real ice-quasi-liquid interfaces exhibit a gradual change of the index of refraction. Neither of these effects has been taken into account in the studies discussed above. The greatest weakness of the ellipsometric studies is that they only allow to determine two parameters. From these a complicated model of the index of refraction profile is deduced. Clearly, this is only possible by employing some assumptions. This might well explain why ellipsometric studies give consistently higher values for the onset temperature than other techniques.

2.6.2 Sum-frequency vibrational spectroscopy

This technique is a second-order nonlinear optical spectroscopy method. The sample is illuminated by two laser beams of different frequencies ω_1 and ω_2. Due to non-linear effects in the sample the photons can mix and produce an outgoing beam of frequency $\omega_1 + \omega_2$. The output signal is proportional to the square of the effective non-linear susceptibility $\chi^2_{eff}(\omega_o = \omega_1 + \omega_2)$. The method gains its interface sensitivity from the fact that the symmetry of the surface layer is different than the bulk. In bulk systems with inversion symmetry, such as ice, $\chi^2_{eff} = 0$. At the interface this symmetry is obviously broken. The sum frequency $\omega_o = \omega_1 + \omega_2$ is only generated at the top interface layer. This allows the measurement of vibration modes of the surface molecules only, which are not accessible with any other technique. The drawback is that only one monolayer is probed and no information is obtained about properties of the subinterface layers. Depth profile or the thickness of the quasi-liquid layer can not be measured.

Shen and Wei have applied the technique to the surface [48, 49] and interface [50] melting of ice. All experiments were performed on the basal plane of ice. For the free surface the disordering of the topmost layer starts at $T = 200K$. It is not surprising that that this temperature is much lower than the onset temperatures measured by other techniques, where the quasi-liquid layer has already been created at the onset temperature, thus replacing the original solid-vapor interface by two new interfaces (see section 2.5.1). Partial disorder in the topmost layer of ice molecules is likely to occur at much lower temperatures. Since information is obtained only for the topmost layer it is impossible to determine how the disorder penetrates into the subsurface region. The authors compare the spectrum of ice with that of supercooled water surface. There are clear differences in the spectrum demonstrating that the surface structure of the quasi-liquid layer is different than the bulk water surface structure.

The interface melting was measured with a hydrophobic and a hydrophilic substrate. An OTS coated fused silica plate was used for the hydrophobic experiment. The authors observe that the interface monolayer is highly disordered at all temperatures. The hydrophobic interaction inhibits any orientationally ordered structure of the OH bonds of the water molecules.

An uncoated and clean fused silica substrate was used for the hydrophilic interface with a strong interaction between the silanol (SiOH) groups of the substrate surface and the water molecules. Therefore the water molecules show no disorder up to –1 °C. Measurements were performed while heating the sample above the melting point. A flipping of the orientation of some water molecules can be observed. It seems that the OH bonds at the silica/ice and the silica/water interface are orientated in opposite directions. This suggests that interface melting is absent or occurring only very close to the bulk melting point or that the surface structure of the quasi-liquid layer is more ice-like than water-like for the hydrophilic interface.

2.6.3 Atomic force microscopy

The atomic force microscope measures forces between the sample surface and a sharp tip. The bending of the cantilever due to the forces is measured by the deflection of a laser beam from the backside of the cantilever. A set of piezoelectric actuators allows the AFM tip to raster-scan the sample. The essential part of the measured signal originates from interatomic repulsion forces. Since these forces are extremely short-ranged it is possible to obtain atomic resolution [51]. Long-range forces, which can be repulsive or attractive, decrease the resolution and can complicate the analysis of the force signal dramatically. Long-range forces can originate from Coulomb forces between charges, van der Waals interaction, capillary forces and other sources. Special care has to be taken when imaging soft materials, since they can easily be damaged by the tip.

Unfortunately ice has most of these negative properties. It is soft and easily damaged by the tip [52]. The premolten layer is a source of capillary forces. This renders AFM measurements on ice very difficult and unreliable. The results on premelting from different groups differ not only quantitatively but also qualitatively. It is unclear whether the signal is influenced by pressure melting and how much heat is transferred from the laser into the ice. The most difficult part in the analysis of the data is to account for squeezing of the quasi-liquid layer and the plastic creep of the soft ice. Lastly, the AFM does not measure a free surface, but an interface between the AFM tip and the ice. This surface is strongly curved (radius of curvature around 10 to 100 nm), with unknown roughness and geometry. Eastman and Zhu address some of these problems [53], resulting in a modified growth law for rounded tips. Calculating the heat flow into the ice from the laser, the temperature rise was found to be significant.

Measurements have also been performed by Döppenschmidt and Butt on polycrystalline ice that has been frozen onto mica sheets [54]. The upper limit for the thickness of the quasi-liquid layer was calculated to be 12 nm at –24 °C and 70 nm at –0.7 °C. They also performed experiments on ice with salt impurities [55] detecting a strong increase of the layer thickness. In addition to the above mentioned problems of AFM experiments on ice, the samples used by this group were very rough with peak-to-valley distances of the order of 100 nm. The authors write that ”This might be a problem when determining the thickness of the quasiliquid layer”. Furthermore the sample was subject to sublimation since no measures had been taken to control the humidity of the air. Interpretation of the data is thus very difficult. The authors give the best proof since in the same year they publish a paper that explains the results by plastic deformation [56].

Bluhm et al. [57] measured the friction coefficient on polycrystalline ice at low temperatures (–40 °C to –24 °C) without observing a premolten layer in the temperature range of the experiment.

Petrenko conducted AFM experiments on ice single crystals [52] with some of the sample surfaces covered with a thin decane layer. This reduces capillary forces and renders the ice surface much more stable since it prevents evaporation. It was found that even under the decane film the surface stays very mobile. Damage by the tip was healed within minutes. From the data it was concluded that a quasi-liquid layer forms at the ice-air interface for temperatures greater than –13 °C with a thickness of 3.5 nm at –10.6 °C. He did not observe a premolten layer for the ice-decane interface.

Several experiments have been performed by Pittenger et al. [58] studying the plastic flow under the AFM tip and electric effects for a charged tip [59]. In a later and careful study [60] they investigated the properties of the quasi-liquid layer at temperatures between –17 °C and –1 °C. Premelting was detected at temperatures greater than -10 °C. Assuming that the quasi-liquid has the viscosity of supercooled water and can be described by a viscous flow continuum model, they calculate layer thicknesses of 2.6 Å for –8.28 °C and 11 Å for –1.01 °C. They also did experiments with a hydrophobically covered tip. In this case the thickness of the quasi-liquid layer is reduced to 7 Å at –1.01 °C.

In conclusion, the more careful studies agree on the existence of interface melting for hydrophilic tips at temperatures higher than –10 °C to –15 °C. Hydrophobic coatings of the tip or the sample suppress premelting.

2.6.4 Quartz crystal microbalance

Tsionsky et al. used a quartz microbalance in order to investigate interface melting in frozen water and aqueous solutions of perchlorid acid and Na_2SO_4 [61, 62]. The quartz crystal vibrates at its resonant frequency in a surrounding medium. This frequency is influenced by the properties of the medium close to the crystal. The thickness probed is about 100-300 nm hence giving the method interface sensitivity. In the experiment the admittance (the inverse of the complex resistance) is measured. It shows characteristic resonance curves at the resonance frequency of the crystal. Changes in the medium change the position and shape of the resonance.

With this method a quasi-liquid layer could be detected in pure ice for $T > -3$ °C. In aqueous solutions the layer could be detected between –5.5 °C and –2 °C. The method does not allow any direct measurement for the thickness of the premolten layer. For the aqueous solutions the authors use viscoelastic and viscous models of the premolten layer to calculate layer thicknesses. At –5 °C a thickness of 16 nm for a 0.1 M Na_2SO_4 solution and 54 nm for a 0.1 M perchlorid acid solution was calculated. Upon heating the solution above –4 °C the behavior of the quasi-liquid layer changes from viscoelastic to viscous.

In a later publication [63] the thickness of the quasi-liquid layer was measured in parallel by laser interferometry. The resolution of the interferometer was 10 nm. The measurements were performed with a third aqueous solution (10 mM $K_4Fe(CN)_6$ + 10 mM $K_3Fe(CN)_6$) at different pressures. The measurements from the interferometer agree reasonably well with the calculated layer thicknesses.

This method lacks the resolution to detect very thin quasi-liquid layers, which explains the high onset temperature. It is important to note that the measurements have not been done in pure ice. Impurities are expected to increase the thickness of the premolten region and even change the growth law [32]. Therefore, the data can not be compared with values for pure ice.

2.6.5 X-ray diffraction and refraction

The free surface of ice has been studied with glancing angle x-ray scattering (GAXS). The sample surface is illuminated by an x-ray beam at glancing incidence. The angle of incidence is smaller or close to the angle of total reflection of the material. This leads to the creation of an evanescent wave in the surface region of the sample. The penetration depth of the evanescent wave field and hence the surface sensitivity can be tuned by varying the incident and exit angle. This method is very powerful for investigating the solid-liquid transition since it probes directly the long range order of the crystal. Since the phase velocity of light for x-rays is higher in materials than it is in vacuum, the index of refraction is smaller than one. In contrast to visible light, optically denser materials exhibit a lower index of refraction. Total reflection occurs for probing beams passing through the interface from the lo (electron) density side to the high (electron) density side. Therefore this method can be used to investigate any free surface. Buried interfaces, however, can be probed only on the high density side of the interface. Since it is difficult to find a material that has a smaller electron density than ice, it is not possible to probe the ice interfaces with this method.

Premelting of the ice-vapor interface has been investigated by Lied et al. [31, 64] using single crystals of different orientations in the experiments. The data confirm a logarithmic growth law. The loss of long-range sets in at –13.5 °C for basal and –12.5 °C for non-basal surfaces. For the basal surface a surprisingly high correlation length of 84 Åwas obtained for the quasi-liquid. This leads to a layer thickness of approximately 160 Å at –2 °C. The non-basal surfaces exhibit approximately half that layer thickness. At temperatures $T > -1$ °C a strong increase in layer thickness can be found. This could be caused by a change from short-range to van der Waals dominated forces (see section 2.5.1).

As discussed above GAXS can not be used to study the structure of buried ice interfaces. A very effective tool to study these systems is high energy x-ray reflectivity (XRR). Since this technique has been used in this work it will be discussed in detail in chapter 3. Engemann et al. investigated the interface of naturally grown amorphous silicon dioxide with the basal plane of an ice single crystal [3, 65] and found premelting at this interface according to

$$L = 3.7\,\text{Å} \ln\left(\frac{-47\,°\text{C}}{(T_M - T)}\right). \tag{2.15}$$

The correlation length of 3.7 Å is much closer to the value expected for water. The interface between the quasi-liquid layer and the bulk ice appeared to be very smooth. The density of the quasi-liquid layer is 20% higher than the density of water. This was interpreted as the signature of a new phase instead of a simple loss of long-range order decaying with depth.

The influence of roughness on the premelting was also investigated [3, 66]. For this experiment a sample with correlated roughness was used. The thickness of the quasi-liquid layer increases much faster with temperature compared to the smooth sample. For high temperatures, the growth law seems to change from logarithmic to power-law behavior.

2.6.6 Other methods

The motion of metal wires charged with a weight through ice has been studied by Gilpin [67]. At low temperatures this motion is due to premelting. At the interface with the wire the surrounding ice is turned into quasi-liquid. The wire travels then through this premolten region, which recrystallizes after the passage of the wire. The wire diameter was ranging from ten to several hundred micrometers. The experiments were performed at temperatures between –35 °C to –0.005 °C. Gilpin found that the viscosity of the quasi-liquid layer is equal to bulk water. The thickness of the quasi-liquid layer grows with a power law.

Golecki and Jaccard investigated the premelting of ice with proton channeling [68] measuring the energy and angular distribution of 100 keV protons that were backscattered from an ice surface. This technique is sensitive to structural disorder in the surface region since disorder reduces the ability of the crystal to channel the incoming protons along the open channels in the high symmetry directions of the crystal lattice [69]. The onset of surface disorder can be detected by a sudden reduction of the scattering depth of the protons. Ice shows surface disorder at temperatures higher than –30 °C. The disordered region grows with a logarithmic growth law. The thicknesses obtained with this method are very large compared to other methods with 94 nm at –1 °C. The results can also be interpreted by anomalously large amplitudes of molecular vibration near the surface. The large layer thicknesses and the low onset temperature are probably produced by a combination of both effects.

Photoelectron spectroscopy has been used by Bluhm et al. [70]. It is difficult to use this technique to investigate ice, since it relies on ultra-high vacuum (UHV) conditions [71]. A differentially pumped sample chamber was used, in which the polycrystalline ice sample was in equilibrium with its vapor. The onset temperature was determined as approximately –20 °C and a layer thickness of 20 Å at –2 °C. Due to the high element sensitivity of this technique the effect of organic contaminants could be measured. High amounts of organic impurities turn the obtained spectrum more water- and less ice-like.

Another spectroscopic technique was used by Sadtchenko and Ewing [72] examining the extinction spectra of an infrared beam. The beam passes through a germanium prism which is covered on one surface by a thin ice film. An evanescent wave propagates through the ice and its extinction is measured. The authors conclude that the spectra of the ice interface region are in good agreement with liquid water. A layer thickness of 15 nm at –0.03 °C was deduced with an onset temperature of –10 °C. From the data it was not possible to distinguish the nature of the growth law (logarithmic versus power-law). Additional effects from impurities or grain boundaries could not be excluded. The thickness measured in the experiment is the sum of the quasi-liquid layer thickness of the ice-vapor and the ice-prism interface. Unfortunately it is not possible to separate both contributions.

2.6.7 Ice in porous media

Confining liquids in porous hydrophilic materials leads to a reduction of the melting point. For a cylindrical pore of radius R this reduction ΔT_m can be calculated by the Gibbs-Thomson equation [73]

$$\Delta T_m = \frac{2T_m \gamma v_m}{H_m R} \propto \frac{1}{R} \tag{2.16}$$

with the bulk melting temperature T_m, the interface energy γ, the molar volume v_m and molar Enthalpy H_m. The reduction of the melting point is due to the curvature of the interface and confinement. It is not premelting in the context used in this work. However, recently it has become possible to create materials with very small pore sizes. For pore radii smaller than 2 nm deviations from Eq.

2.16 could be measured. The melting behavior can be accurately reproduced for all pore sizes by modifying Eq. 2.16 with a reduced radius $R - d$

$$\Delta T_m = \frac{2T_m \gamma v_m}{H_m(R-d)}. \tag{2.17}$$

d is interpreted as the thickness of a layer of unfrozen water that covers the walls of the pore. Differential-scanning-calorimetry (DSC) measurements [74] give a value of $d \approx 4$ Å. The water layer stays liquid down to –50 °C. It is unclear whether this layer is structurally equivalent to quasi-liquid layers occurring on flat interfaces.

2.6.8 Summary

Almost all of the experiments that have been discussed in the previous sections confirm the existence of surface melting of ice at the ice-vapor and ice-air interface. Interface melting seems to be present at hydrophilic ice-solid interfaces while hydrophobic coatings decrease the thickness or inhibit the formation of a quasi-liquid layer.

While there is an agreement on the qualitative properties of premelting, the quantitative results of the experiments scatter strongly. This has different reasons. The free surface of ice is very unstable. Molecules from the surface are in constant exchange with molecules in the gas phase. Undersaturation of water vapor leads to pit etching while oversaturation leads to the formation of islands. In both cases the surface roughens.

The premelting of ice is very sensitive to contamination of the interface. It is very difficult to rule out any form of contamination during the preparation and handling of the sample and during the experiment. The major share of accidental contamination probably comes from organic compounds that are floating in the air.

Since the thickness of the quasi-liquid layer depends on the crystal orientation, experiments performed on polycrystals should show different results for the melting behavior than experiments employing single crystals. Roughness plays an important role in premelting, yet most of the experimental techniques do not allow to measure the roughness on an atomic scale.

The limitations mentioned above are mostly to imperfect samples. But even with perfect samples a scattering of the observed melting behavior would be expected since the different methods measure different physical properties of the sample. Interface melting is a complex phenomenon. Different material properties are likely to change at different stages of premelting. It seems reasonable to assume that the enhanced vibrational activity detected by sum-frequency vibrational spectroscopy and proton channeling sets in before the long-range order, which is detected by x-ray diffraction, is lost in the subsurface area.

2.7 Environmental effects of ice premelting

A large range of natural phenomena is influenced by the premelting of ice. Only a short discussion of a few selected phenomena can be presented here. The interested reader can find more details in the review papers by Dash et al. ([44] and more recently [75]).

Repeated freezing of the ground in fine-grained soils may lead to an upwards displacement of the surface. This phenomenon is known as frost heave. It arises from the formation of so-called ice lenses below the surface. This are layers of ice that contain no or very few soil particles. The particles are pushed up instead during freezing, leading to the rise of the ground surface.

To understand this phenomenon, it is important to identify the mechanism that pushes the soil particles out of the freezing ice lens. For a propagating freezing front it is thermodynamically favorable to repel particles that are poorly wet [76]. Dash could show [77] that the presence of premelting at the solid surface leads to a negative thermodynamic pressure. Thus, the propagating ice front has two effects: It pushes away the soil particles. Due to the negative pressure more moisture is sucked below the repelled particle. If the grain size is small enough and the freezing is slow enough this leads to a stable and continuous motion.

The freezing front can propagate continuously as long as water can be sucked through the porous soil to feed the ice growth. The soil is displaced upwards, leading to a deformation of the ground. Due to interface melting and confinement (see section 2.6.7) quasi-liquid water will be present in the soil even in sub-zero temperatures, further enhancing the effect.

Frost heave can lead to serious damage to roads and railways, displace foundations, crack masonry and jam doors. Over several years it can also lead to the formation of patterned grounds, where stones become organized in circular rings.

The weathering of rocks is caused by a related process. Many textbooks claim that this process is due to the expansion of ice during freezing. However, the water in rocks is never perfectly confined, allowing the forming ice to expand to the outside of the stone. Instead, the rocks are cracked by additional water sucked into the rock during freezing.

Thunderstorms belong to the most dramatic weather phenomena. The charging of a thunderstorm cloud is caused by charge transfer between ice particles. The exact mechanism of this transfer is still under debate and might depend on the physical and chemical conditions of the cloud. The availability and type of ions present as impurities in the ice particles might play an important role in the

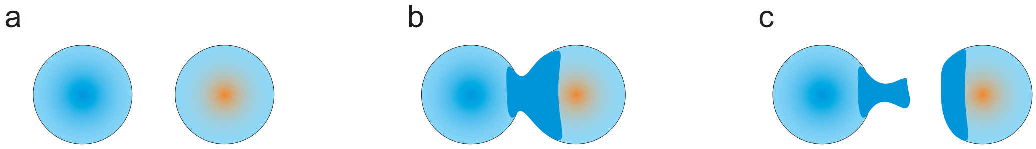

Figure 2.2: Mass transfer between two colliding particles in a thunderstorm cloud. a: Particles before the collision. b: Particles during the collision. The energy deposited during the collision creates a shared quasi-liquid layer. The warmer particle (right particle) contributes more to this collisional layer. c: After collision. The particles separate, each taking half of the shared layer. This results in a mass transfer from the hotter to the colder particle.

sign and magnitude of the charge transfer [78].

Ions are transferred between ice particles in the thunderstorm cloud during collisions. Dash et al. [79] proposed a model of this process. Upon colliding, a quasi-liquid layer is formed between the particles as a combination of premelting and the deposition of kinetic energy. Ions have a high diffusion coefficient within the shared quasi-liquid. When the particles separate, each particle is assumed to take half of the shared premolten region. However, if the particles have different temperatures before the collision, the warmer particle contributes more mass to the shared layer, since it exhibits a thicker quasi-liquid layer. This leads to a mass transfer from the warm to the cold particle. A sketch of this process is shown in Fig. 2.2. Due to the high diffusion speed of ions, this is accompanied by a charge transfer between the particles.

Clearly, many assumptions have to be made in this model. For example, the amount of energy deposited during the collision is mostly unknown. In addition, data of processes in natural thunderstorms is scarce and laboratory experiments often face limitations upon scaling to the natural phenomenon.

It is since long known that the friction coefficient of ice is strongly temperature-dependent. Arctic expeditions noticed that at very low temperature, the ice became more sand-like. This is because the low friction on ice comes from a lubricating (pre-)molten surface film. There are two processes leading to its formation, and both are temperature-dependent.

At high sliding speed, the lubrication is mainly produced by *frictional heating*. The heat produced by the friction is melting the ice surface and leads to the formation of a thin water film. This is evident by experiments performed by Evans et al. [80] measuring the friction coefficient for different sliding speeds and materials on ice. The study showed that insulating materials exhibit lower friction coefficients than good heat conductors owing to the heat lost by conduction in the sliders. Using thermally insulated sliders all the produced frictional heat stays at the interface and melts the ice surface, thus producing a thicker molten layer, with a lower friction coefficient. These findings are confirmed by Colbeck [81].

However, ice is also slippery at slow sliding speeds. Interface melting can produce films of significant thickness for temperatures $T > -10$ °C, depending of the purity of the ice and the quality of the surface. Since the thickness of the premolten layer is independent of the sliding speed, it offers a good explanation for the low friction at low speeds. In addition, Koning reports [82] that chemical impurities can further lower the friction coefficient even at high sliding speed. Since frictional heating is not supposed to be influenced by impurities, this indicates that the quasi-liquid layer also plays a role at high speeds.

Chapter 3

X-ray refraction

X-ray reflectivity is a powerful tool for examining density profiles at interfaces. This chapter introduces the theoretical background of x-ray refraction and the formalisms used to analyze reflectivity data. The following chapter will discuss the experimental setup in detail. More detailed introductions into x-ray refraction can be found in [83, 84].

3.1 Refraction of light

Refraction is a phenomenon occurring when a beam of light impinges at an interface between two materials with different speed of light c_i (see Fig. 3.1). The incoming beam is split into a reflected beam and a transmitted beam. The change in velocity leads to a change in direction for transmitted rays that are not normal to the interface. The relation between incident (θ) and refracted angle (θ') can be calculated by Snell's law

$$\frac{\cos\theta}{\cos\theta'} = \frac{n_2}{n_1}. \tag{3.1}$$

n_1 and n_2 are the *index of refraction* for the materials and are defined as

$$n_i = \frac{c_0}{c_i} \tag{3.2}$$

with the velocity of light in vacuum c_0 and in the material c_i. For visible light the index of refraction is always greater than 1. For x-rays the index of refraction is smaller than 1, indicating a *phase* velocity of light greater than the vacuum velocity. The difference to unity is very small and n can be written as

$$n = 1 - \delta + i\beta. \tag{3.3}$$

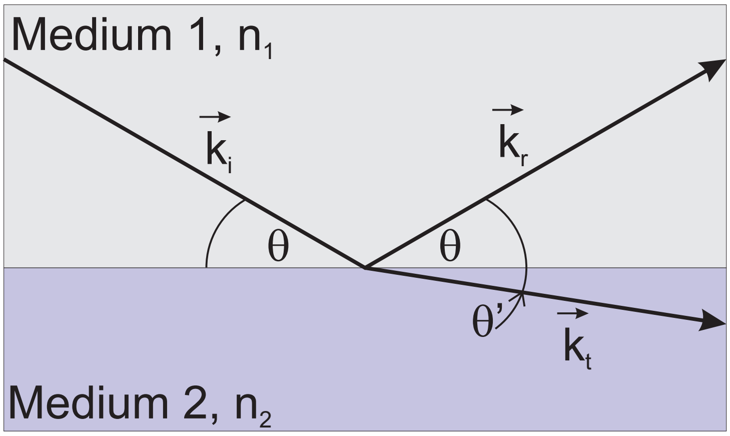

Figure 3.1: A x-ray beam is reflected from a perfect interface. The beam is split into a reflected and a transmitted beam.

The terms δ and β depend on the wavelength λ and the x-ray form factor

$$f = f^0 + f'(\lambda) + f_{NT} + if''(\lambda). \tag{3.4}$$

The anomalous term $f'(\lambda)$ accounts for dispersion corrections and is negligible for x-ray energies far away from any absorption edges. $f''(\lambda)$ accounts for absorption. f_{NT} is the nuclear Thomson correction. The form factor can also be expressed by the functions f_1 and f_2

$$f' = f_1 + f_{rel} - Z \tag{3.5}$$
$$f'' = f_2 \tag{3.6}$$

Tabulated values for f_1, f_2, f_{NT} and f_{rel} can be found in [85]. Z is the atomic number. With Eq. 3.4 and the number density of atoms or molecules n_a, δ and β can be expressed as

$$\delta = \frac{\lambda^2}{2\pi} r_e n_a \Re(f) \tag{3.7}$$
$$\beta = \frac{\lambda^2}{2\pi} r_e n_a \Im(f). \tag{3.8}$$

For non-elemental materials the total form factor is given as the weighted sum of the form factors of the different elements in the compound. The number density n_a can be calculated from the (mass) density ρ, the molar mass M_{mol} and Avogadro's number N_A

$$n_a = \frac{\rho N_A}{M_{mol}}. \tag{3.9}$$

For x-ray energies far from absorption edges $\Re(f) \approx Z$. Therefore δ can be expressed in terms of the electron density

$$\rho_e = \sum_{i=1}^{N} Z_i n_{a,i} \tag{3.10}$$

for N different elements i, giving

$$\delta = \frac{\lambda^2}{2\pi} r_e \rho_e . \tag{3.11}$$

3.2 Reflection from a perfect, infinite substrate

In this section the case of a x-ray beam reflected from an infinitely thick substrate with a perfect interface (no roughness) is considered. The x-ray beam can be described by an electromagnetic plane wave

$$\vec{E}(\vec{r}) = E e^{(i\vec{k}\vec{r})} \tag{3.12}$$

with the Amplitude E and the wave vector $\vec{k}$. When the incident wave (denoted by indexes i) impinges at the interface it is split into a reflected (r) and a transmitted (t) part. At the interface the transverse component of the electric wave field must be continuous. This requires

$$\begin{aligned} E_i + E_r &= E_t & (3.13)\\ E_i\vec{k}_i + E_r\vec{k}_r &= E_t\vec{k}_t . & (3.14) \end{aligned}$$

In medium 1 the norm of the wave vector is $k_i = k_r = n_1 k_0$ and $k_t = n_2 k_0$ in medium 2 (see Fig. 3.1). Equation 3.14 can be split into the part parallel and the part perpendicular to the interface with the angle of incidence θ and the refracted angle θ'

$$\begin{aligned} (E_i + E_r) n_1 k_0 \cos\theta &= E_t n_2 k_0 \cos\theta' & (3.15)\\ (E_r - E_i) n_1 k_0 \sin\theta &= -E_t n_2 k_0 \sin\theta' . & (3.16) \end{aligned}$$

Inserting Eq. 3.13 into Eq. 3.15 reproduces Snell's law (see Eq. 3.1). Combining Eq. 3.13 with Eq. 3.16 we find

$$\frac{E_i - E_r}{E_i + E_r} = \frac{n_2}{n_1}\frac{\sin\theta'}{\sin\theta} . \tag{3.17}$$

Form this equation the Fresnel formulas can be calculated

$$r = \frac{E_r}{E_i} = \frac{n_1 \sin\theta - n_2 \sin\theta'}{n_1 \sin\theta + n_2 \sin\theta'} \tag{3.18}$$

$$t = \frac{E_t}{E_i} = \frac{2n_1 \sin\theta}{n_1 \sin\theta + n_2 \sin\theta'} \tag{3.19}$$

with the *amplitude* reflectivity r and transmittivity t.

The difference between the wave vector of the incident $\vec{k}_i$ and the reflected wave $\vec{k}_r$ is called the *momentum transfer* $\vec{Q}$

$$\vec{Q} = \vec{k}_r - \vec{k}_i. \tag{3.20}$$

In reflectivity measurements, the momentum transfer is always perpendicular to the interface and a vector description of the momentum transfer is not needed. It can be calculated from the incident angle

$$Q = \frac{4\pi \sin\theta}{\lambda}. \tag{3.21}$$

The function

$$R(Q) = |r(Q)|^2 \tag{3.22}$$

is called the (intensity) *reflectivity* of the interface. The reflectivity from a perfect interface is called *Fresnel reflectivity* R_F of the interface. For large momentum transfers (high angles) the amplitude of the Fresnel reflectivity can be approximated by

$$r_F \approx \left(\frac{\theta_c}{2\theta}\right)^2. \tag{3.23}$$

A wave penetrating from an optically dense medium into a less dense medium undergoes total reflection for small incident angles. Since the index of refraction for x-rays is smaller than unity, total reflection is observed for reflecting from a material with higher electron (and therefore mass) density. Total reflection occurs when the refracted angle θ' is zero. This critical incident angle can be calculated from Snell's law (Eq. 3.1)

$$\theta_c = \arccos\left(\frac{n_2}{n_1}\right) = \arccos\left(\frac{1-\delta_2}{1-\delta_1}\right) \approx \sqrt{2(\delta_2 - \delta_1)}. \tag{3.24}$$

For incident angles $\leq \theta_c$ no radiation is transmitted through the interface. Instead an evanescent wave field propagates through the substrate. Apart from absorption of this evanescent wave all the intensity is reflected.

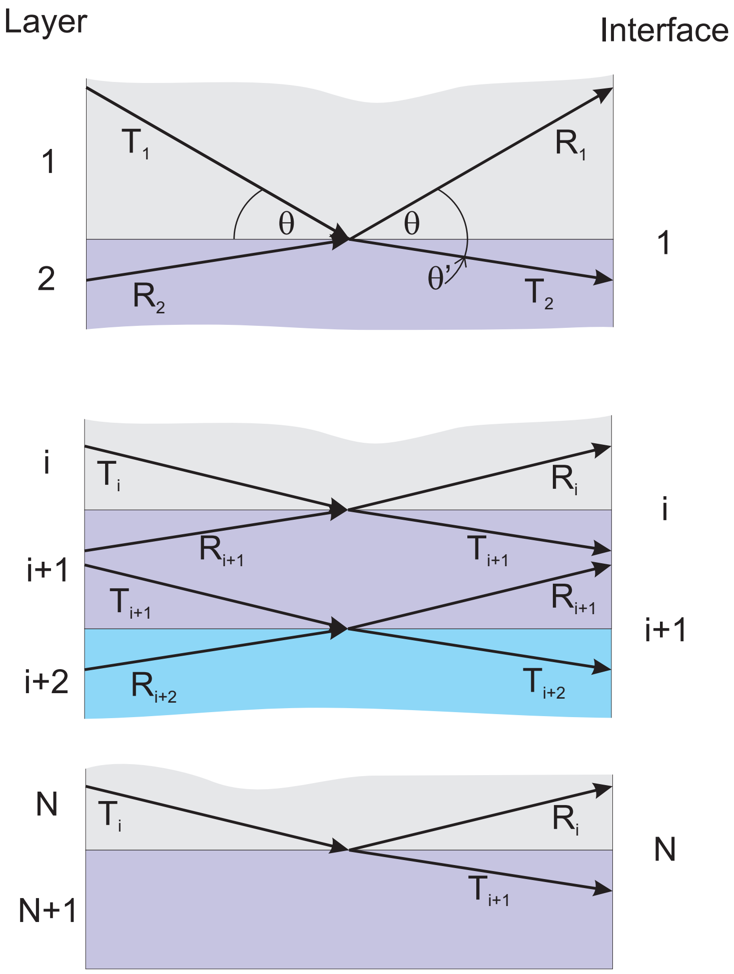

Figure 3.2: Reflection from N interfaces. At each interface a transmitted wave and a reflected wave are created. These wave fields interfere with the incoming waves, transmitted from the interface above and reflected from the interface below.

3.3 Reflectivity from perfect layered structures

This section examines the case of a semi infinite substrate (see section 3.2) covered by one ore more perfect slabs of finite thickness. Each interface splits the beam into a reflected and a transmitted part. In addition, except for the interface of the infinite substrate, beams reflected from lower interfaces interfere with the wave fields coming from the top. At certain reflection angles θ the wave fields will be in constructive interference, leading to high intensities, while in other angular regions destructive interference occurs. This leads to oscillations (so called *Kiessig fringes*) in the reflectivity curve.

Figure 3.2 shows the case of a system of $N-1$ layers i. $i=1$ denotes the semi-infinite material through which the incident wave is propagating. The wave field is transmitted through $N-2$ layers of thickness d_i until it is reflected from the substrate of infinite thickness $i=N+1$. At each interface i between the layers i and $i+1$, the transmitted wave T_i separates into the reflected wave R_i, propagating through the layer i and the transmitted wave T_{i+1}, propagating through the layer $i+1$. In addition, the wave R_{i+1}, reflected from the interface $i+1$, interferes with those waves.

The reflectivity of perfect multilayer structures can easily be calculated with Parratt's recursive method (see 3.5.2). However, in real systems the interfaces are never perfect. The following sections show how systems that can not be modeled by thick uniform slabs of constant electron density can be formally treated.

3.4 Arbitrary dispersion profiles

Many systems can not be described by simple box models with constant electron density within the boxes. In this case the interface has to be described by a function $\delta = \delta(z)$, the dispersion profile of the system ($\delta \propto \rho_e$, see Eq. 3.11). z is defined as the direction perpendicular to the interface plane. In the following interface roughness will be expressed in terms of dispersion functions.

Real interfaces between two materials are never atomically smooth. At a rough interface the position z_i of the interface is a function of the lateral coordinates

$$z_i = z_i(x, y). \tag{3.25}$$

This height function will fluctuate around the average height in the area A

$$\bar{z}_i = \frac{1}{A} \int \int z(x, y) dx dy. \tag{3.26}$$

The height fluctuations are defined as

$$h(x, y) := z(x, y) - \bar{z}. \tag{3.27}$$

Two important values to characterize an interface are the root-mean-squared (rms) roughness

$$\sigma := \sqrt{\frac{1}{A}\int\int h^2(x,y)dxdy} \tag{3.28}$$

and the correlation function

$$\xi(\chi,\psi) := \frac{1}{A}\int\int h(x,y)h(x+\chi,y+\psi)dxdy. \tag{3.29}$$

The correlation function describes how strongly the height fluctuation of the interface at (x, y) is influenced by the fluctuation at $(x+\chi, y+\psi)$. Notice that for every value of (χ, ψ) a full integration of the area has to be performed. In the case of a laterally isotropic interface, Eq. 3.29 simplifies to

$$\xi(\rho) = \frac{2\pi}{A}\int h(r)h(r+\rho)rdr. \tag{3.30}$$

Correlations in the interface fluctuations are a source of off-specular diffuse scattering. For strong correlations a Lorenzian diffuse background appears on which the (resolution limited) specular signal is superimposed. Very strong correlations lead to the vanishing of the specular reflection and only a very broad and diffuse signal is obtained. A way to treat reflectivity from strongly correlated interfaces has recently been published in [66]. More literature can be found in [83, 3].

In this work only non-correlated interfaces ($\xi(\rho) \approx 0$) have been investigated. It will be assumed that the height fluctuations follow a Gaussian distribution

$$h(z) = \frac{h_0}{\sqrt{2\pi}\sigma}e^{-\frac{z}{2\sigma}}. \tag{3.31}$$

The dispersion profile $\delta(z)$ for a perfect interface between materials 1 and 2 is a step function

$$\delta(z) = \begin{cases} \delta_1 & \text{for} z \le z_0 \\ \delta_2 & \text{for} z > z_0 \end{cases} \tag{3.32}$$

The roughness of the interface leads to a blurring of this dispersion profile since the effective index of refraction at a certain z-value is a mixture between the values of the two interface materials, since the index of refraction of a compound is the average of the refraction index of the constituents. The dispersion profile is therefore given by

$$\delta(z) = \delta_1 \cdot f(z) + \delta_2 \cdot (1 - f(z)) \tag{3.33}$$

with the distribution function $f(z)$ with

$$\int_{-\infty}^{+\infty} f(z)dz = 1. \tag{3.34}$$

For Gaussian fluctuations we find

$$f(z) = \frac{1}{\sqrt{2\pi}\sigma} \int_{-\infty}^{z} e^{-\frac{z}{2\sigma}} dz = \frac{1}{\sqrt{2\pi}\sigma} \text{erf}\left(\frac{z}{2\sigma}\right). \tag{3.35}$$

with the error function erf as the integral of the Gauss function. Gaussian roughness blurs the step function of the perfect interface to an error function dispersion profile.

3.5 Formalisms to calculate the reflectivity

In the following, two formalisms for the calculation of the reflectivity from multilayer structures and dispersion profiles are introduced. The master formalism uses the kinematic approximation. Parratt's recursive method is a full dynamical calculation.

3.5.1 The master formalism

Within the kinematic approximation multiple scattering events are neglected. Therefore, reflectivity curves calculated with this formalism are only correct for momentum transfers far greater than the momentum transfer values Q

$$Q \gg Q_c = \frac{4\pi}{\lambda} \sin\theta_c. \tag{3.36}$$

For the derivation of the master formula the dispersion profile of the interface is decomposed into infinitesimaly thin slabs. The reflectivity of one slab is calculated. The reflectivity of the entire interface is then obtained by integrating over all slabs multiplied by the appropriate phase factor. The full derivation can be found in Appendix A. The *master formula* is given by

$$R(Q) = \frac{R_F(Q)}{\delta_{-\infty} - \delta_{+\infty}} \left| \int \frac{d\delta(z)}{dz} e^{iqz} dz \right|^2. \tag{3.37}$$

R and R_F are the intensity reflectivities of the interface and the Fresnel reflectivity. $\delta(z)$ is the dispersion profile, $\delta_{\pm\infty}$ the values of δ for $z \to \pm\infty$. The second term in Eq. 3.37 is a Fourier transform of the derivative of the dispersion profile. It yields the deviations from the Fresnel reflectivity.

As mentioned before the kinematical approximation is not valid close to the edge of total reflection. However, it offers several advantages in comparison to a fully dynamical description. It is fast and easy to implement into fitting algorithms. The closed form allows to predict and understand the effect of dispersion profiles on the reflectivity curve. It is intrinsically able to deal with arbitrary dispersion profiles.

3.5.2 Parratt's recursive method

The Parratt formalism is a fully dynamic and exact calculation. It was introduced by L.G. Parratt [86] in order to calculate the reflectivity of multilayer interfaces. However, it can also be used to treat arbitrary dispersion profiles.

At first a perfect multilayer structure as described in section 3.3 and shown in Fig. 3.2 will be discussed. An electromagnetic wave of amplitude $T_1 = 1$ impinges at the multilayer structure. At each interface it is split into the transmitted wave T_{i+1} and the reflected wave R_i that interfere with the waves coming from the top (T_i) and bottom (R_{i+1}) layer. Parratt's recursive method links the reflectivity and transmittivity coefficients, for the layer j to the coefficients of the layer $j+1$ below

$$X_j = \frac{R_j}{T_j} = e^{-2ik_{z,j}z_j} \frac{r_{j,j+1} + X_{j+1}e^{2ik_{z,j+1}zj}}{1 + r_{j,j+1}X_{j+1}.e^{2ik_{z,j+1}z_j}} \tag{3.38}$$

The reflectivity coefficients are calculated employing the change in the z-component of the wave vector ($k_{z,i} = \vec{k}_i \cdot \vec{e}_z$)

$$r_{j,j+1} = \frac{k_{z,j} - k_{z,j+1}}{k_{z,j} + k_{z,j+1}}. \tag{3.39}$$

Since the substrate has infinite thickness, there is no incoming reflected wave R_{N+1}. It follows that $X_{N+1} = 0$. With this starting point Eq. 3.38 can be applied recursively to retrieve all the coefficients X_i until the total reflectivity of the multilayer can be calculated after N iterations

$$R = |R_1|^2, \tag{3.40}$$

since $T_1 = 1$.

So far the calculated reflectivity is exact only for a multilayer system with *perfect* interfaces. It does not include roughness. For a small (rms roughness $\sigma \ll d$, see section 3.4) and uncorrelated ($\xi \approx 0$) roughness the effect of the roughness of the interfaces can be approximated by multiplying the reflectivity coefficients of each interface with an exponential damping factor

$$\tilde{r}_{j,j+1} \approx r_{j,j+1}e^{-q_z^2\sigma^2}. \tag{3.41}$$

It is important to keep in mind that this approximation is only valid for $\sigma \ll d$. If this is not the case the roughness has to be treated as an arbitrary dispersion profile (see section 3.4).

An arbitrary dispersion profile $\delta(z)$ can be solved by the Parratt formalism by slicing it into small slabs of thickness dz. The dispersion of the slab i at depth z_i is $\delta(z_i)$. Then this multilayer of small, but perfect slabs is recursively solved. This approach is exact for uncorrelated interfaces under the condition that the thickness of the slices is small enough for a good representation of the dispersion profile. The disadvantage of this approach is that it is comparably slow.

Chapter 4

Experimental setup

The experiments performed in the framework of this thesis are challenging in three ways. The properties of the interface have to be controlled on the molecular level. For this reason great care has to be taken in choosing high quality substrates and fusing them to the ice crystal in the most controlled way. During the experiment, special sample chambers have to guarantee accurate temperature control, while giving access to the x-ray beam. The methods to achieve these goals will be presented in the first part of this chapter.

High energy x-ray reflectivity is a new method that has high requirements on the precision of the beamline and diffractometer setup. The experimental setup will be described in detail in the second part. The third part is dedicated to the methods of data analysis.

4.1 Sample preparation

All samples used in this work were prepared from substrates with a high quality surface finish that have been molten into an ice single crystal. The first two subsections will discuss the properties of the substrate and the ice, respectively. Then the melting process will be described. Finally the various chambers for a controlled sample environment will be presented.

4.1.1 The substrates

A broad spectrum of samples has been used for the work presented here. Since the experimental method used is new, part of this investigation is aimed to understand which substrates are useful for high energy x-ray reflectivity experiments. This will be discussed later. Most substrates are oxide materials, but also thin metal layers and self assembled monolayers (SAM) have been investigated. Table 4.1

gives an overview of the properties of the different substrates. The roughness of the substrates was measured with x-ray reflectivity, using a laboratory x-ray tube using copper radiation ($\lambda = 0.14$ nm).

Sample	**Material**	**Structure**	**Size [mm]**	**Thickness**	**Roughness**
1	Float Glass	Amorphous	20 x 20	10 mm	10 Å
2	Sapphire	Hexagonal	20 x 20	1 mm	6 Å
3	Silver	FCC	20 x 20	160 Å	5 Å
4	Quartz	Hexagonal	20 x 20	1 mm	4 Å
5	Quartz	Hexagonal	20 x 20	2 mm	3 Å
6	Silica	Amorphous	Ø25.4	12.7 mm	6 Å
7	Silica	Amorphous	Ø25.4	12.7 mm	6 Å
8	Quartz	Hexagonal	12.7 x 25.4	12.7 mm	5 Å
9	MgO	Cubic	20 x 20	10 mm	6 Å
10	FAS	*SAM*	25 x 10	19 Å	4 — 7 Å
11	OTS	*SAM*	25 x 10	31 Å	10 Å

Table 4.1: Overview over the substrates used in this work.

Interface melting of ice was already successfully observed at the native oxide layer on silicon substrates [3]. The substrates for this work were selected in order to systematically investigate the influence of different substrate properties on premelting. For this reason substrates that are chemically identical, but structured differently, e.q. quartz and silica, were investigated, as well as chemically different substrates.

Float glass

Glass is an interesting substrate, because it consists of amorphous SiO_2 similar to the substrates used in [3]. Unlike the samples measured before, it is not pure, but hosts additional elements inside. This allows the determination of the influence of impurities on premelting.

Float glass was chosen because it has been used for diffraction surface experiments before [64]. It is known to exhibit very small roughness and is easy to clean. It consists of 80% SiO_2 mixed with 12.5% B_2O_3 and small amounts of Al_2O_3, Na_2O and K_2O. XPS measurements have been performed on the glass to confirm the composition. The observed elements agree well with the expectations, except for large amounts of tin (Sn) present on the surface. This contamination originates from to the manufacturing process, where the glass is cooled in a tin bath.

Before fusing the ice crystal, the substrate was cleaned in an ultrasonic soap and acetone bath. Then it was cleaned in chromium sulfuric acid for several hours and finally rinsed with pure water with resistance of at least 12 MΩ·cm. The sample was kept in the pure water until the start of the bonding process in order to avoid surface contamination by organic pollutants.

Sapphire

Sapphire is chemically different to the samples measured in [3]. Like quartz, it crystallizes in a hexagonal lattice. The main motivation behind the investigation of this sample is the isolation of the chemical impact, when comparing the results for the sapphire sample with the quartz sample. Obviously, their atomic structures are different, but at least the influence of the lattice can be reduced since both materials share the same crystal lattice type.

The sapphire (Al_2O_3) substrates were bought from *Crystec*. The surface was oriented parallel to the (0001) plane of sapphire with a precision of ± 0.5%. The roughness was 6 Å. The sapphire was cleaned in an ethanol ultrasonic bath before melting it into the ice crystal. No etching was applied, in order to avoid roughening. Due to the small thickness of the sapphire it was put on a block of pure (purity > 99.99%) aluminum. To reduce the roughness of the surface, the substrate was baked for 12 hours at 1000 °C.

Silver

All the work done on interface melting of ice so far investigated ice-insulator interfaces. However, for technical applications, the ice-metal interface is very important. Substantial differences in the melting behavior between metals and insulators could also shed light on the processes behind premelting. One problem when working with metals is that the formation of an oxide layer has to be avoided. For this reason, a noble metal was chosen. Noble metals have very high electron densities, which makes it difficult to observe thin, low-contrast structures at their interface. Silver was chosen as a compromise between nobility and electron density.

Since it is very difficult to polish soft metal crystal surfaces to subnanometer roughness, thin silver layers were grown on a sapphire substrate by molecular beam epitaxy (MBE). The growth of these layers was done by Dr. Thomas Wagner from the MBE service group of the Max-Planck-Institute for Metals Research. The sapphire substrate was the same as described before. On the sapphire a small buffer layer (≈ 8 Å) of aluminum was grown on which the silver layer is deposited. The thickness of the silver layer is 160 Å. Due to the buffer layer the surface of the silver film was very smooth ($\sigma \approx 5$ Å) [87].

The thin silver layer can easily be damaged during sample preparation. Therefore the surface was only cleaned by wiping it with a soft tissue using ethanol.

Quartz

Quartz is crystalline SiO_2. It is therefore chemically identical to the samples measured in [3]. This allows the isolation of the structural influence on premelting.

The substrates were supplied by *Crystec*. They were oriented with a (0001) surface normal, with the same accuracy as the sapphire substrates (see above). The first two samples are small plates of 20 mm length and a thickness of 1 mm and 2 mm respectively. Since the experiments revealed that thin samples are easily bent during the freezing of the ice, tick quartz substrates were employed. The sample that was used in the main experiment was a block of 25.4 mm x 25.4 mm length and 12.7 mm thickness.

All the quartz samples were cleaned by ultrasonic baths of soap, ethanol and acetone, followed by a several hours lasting bath in chromium sulfuric acid. They were rinsed and kept in pure water until they were frozen into the ice. The thin plates were put on a block of high purity aluminum before contacting the ice.

Silica

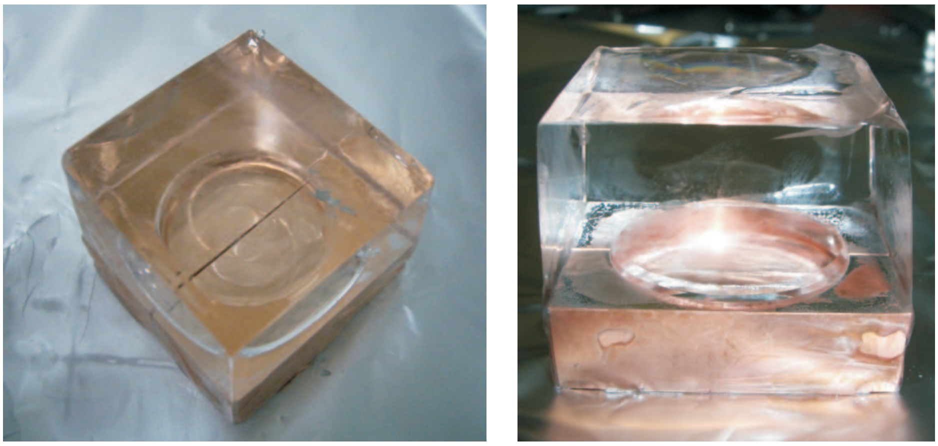

Figure 4.1: Photo of one of the fused silica substrates. The silica disc is in the middle, surrounded by the copper clamps. The substrate has already been fused into the ice single crystal.

Silica, also called *fused silica*, is a high purity glass that consists of 100% SiO_2. It is chemically identical and structurally similar to the samples investigated by Engemann et al. . For this reason similar results are expected. This allows to check for the reproducibility of the setup and the sample preparation.

The disk-shaped substrate (diameter 25.4 mm, thickness 12.7 mm) used was supllied by *Wave Precision*. Since the sample chamber was designed for block-shaped samples an adapter piece was needed. The shape was adapted by two

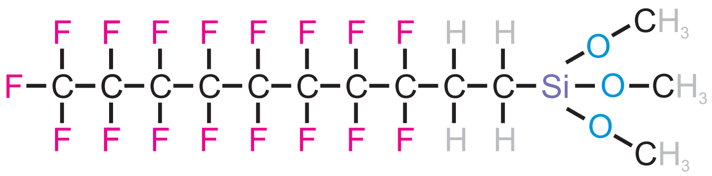

fluoroalkylsilane

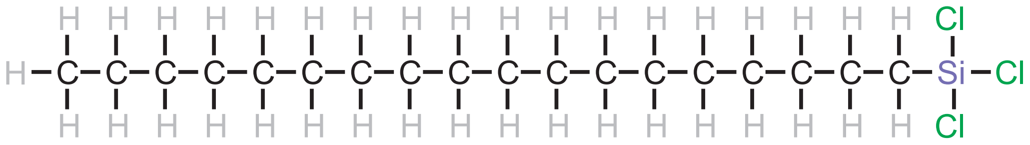

octadecyl-trichlorosilane

Figure 4.2: Chemical structure of the self-assembled monolayers used in this work.

copper clamps that ensure a sufficient heat contact between the peltier elements of the chamber and the substrate. A photo of one of the samples after contacting it with the ice can be seen in Fig. 4.1. The silica samples were cleaned in the same way as the quartz samples.

Magnesiumoxide

Magnesium oxide crystallizes with a cubic structure. It was chosen to investigate an isolator with non-hexagonal structure. The substrate with (100) surface normal was supplied by *Crystec*. Since the MgO surface is not stable against water, it was only cleaned with acetone.

Self-assembled-monolayers

In order to investigate the structure of ice at hydrophobic interfaces, two substrates covered with self assembled monolayers were prepared. The two molecules were octadecyl-trichlorsilane (OTS) with a pure hydrocarbon tail, and fluoroalkylsilane with a fluorinated tail. The chemical structure of the two molecules is shown in Fig. 4.2.

The self assembled monolayers were grown on silicon (111) substrates. The substrates were cleaned in ultrasonic baths of ethanol, acetone and chloroform before being cleaned in fresh Piranha solution (H_2SO_4 and H_2O_2 in relation 2:1). In a last cleaning step the substrates were irradiated with intense UV-radiation in a thin pure water bath. The UV light cracks organic contaminations and creates OH radicals that attack organic molecules. After cleaning the samples they were carefully rinsed with pure water and dried in a high purity argon jet.

The OTS film was grown by depositing the substrate in a 3:1 solution of n-hexane and chloroform mixed with 1 mM OTS. The OTS was supplied by *Aldrich* with a purity of 90%. The sample was kept in the solution for three hours and subsequently rinsed with n-hexane and toluene. After this procedure it was fused into the ice.

The self-assembled monolayer of FAS was prepared by evaporating 15 mg of FAS from the bottom of a dried glass container. The substrate was kept on a glass plate above the FAS. To evaporate the FAS, the container was sealed air-tight and left overnight in an oven at 110 °C. After that, the sample was removed and immediately put into a bath of n-hexane to prevent the polymerisation of the FAS-molecules. Finally, the sample was cleaned in ultrasonic baths of hexane and water.

4.1.2 The ice crystals

Growth

The ice single crystals were grown by Jörg Bilgram from the ETH Zürich. Water is supercooled in a plastic tube. A seed crystal of the desired orientation is used as a nucleus for the freezing process.

The quality of the crystal is further enhanced by repeated zone refining where a thin melting zone is slowly moved along the crystal. The cooling material freezes preferably in the direction of the material surrounding it. Since most of the material is oriented in the direction of the seed crystal the domains oriented in the desired direction grow at the expense of the domains with other orientations.

The quality of the crystal can be determined by x-ray diffraction. High quality crystals exhibit a low *mosaicity* describing how well the lattice planes of the crystal are aligned with each other. The mosaicity leads to broadening of the Bragg reflections of the lattice. The mosaicity of the ice samples has been measured with a diffractometer in a cold room using copper radiation. Typical Bragg reflections are shown in Fig. 4.3. The FWHM of these reflections ranges from 0.03°to 0.1°, although some crystals can have Bragg reflections that are sharper than the resolution of the diffractometer (0.01°). Since Cu K_α radiation is strongly absorbed in the ice, only a thin surface layer could be probed. The value provided by the experiment is an upper limit for the mosaicity of the ice single crystal, since the quality of the surface is lower than the quality of the bulk crystal.

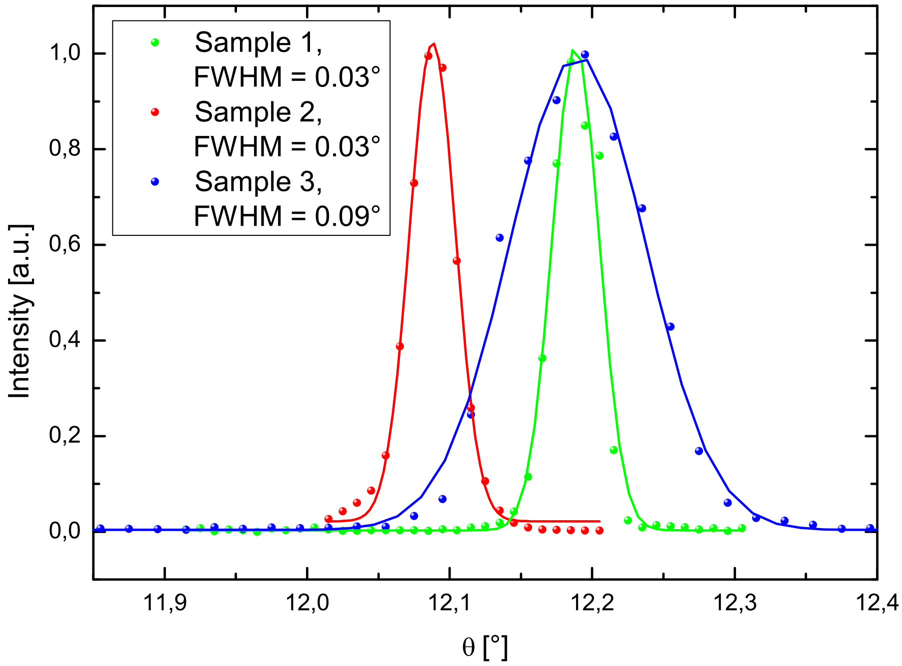

Figure 4.3: Rocking scans of different ice samples cut from the same single crystal. The data were taken with a copper sealed tube.

Handling and orientation

The storage and handling of the ice crystals was done in a walk-in cold room. The base temperature of the room was -16 °C. The ice room underwent two de-icing cycles per day (at 6 am and 22 pm), when the temperature went up to -10 °C. To avoid the transport of humidity, a smaller cold room at -10 °C allowed access to the main cold room. Since this entrance was the only air exchange for the room, the humidity could be kept at very low levels.

Since impurities influence the interface melting of ice [32], care was taken to work in the cleanest possible conditions. All parts in direct contact with the ice were manufactured from aluminum and cleaned by etching with NaOH. Since it was not possible to work under clean room conditions, the exposure time of the ice crystal surfaces to air was kept to a minimum.

The single crystals produced by J. Bilgram are frozen into a plastic tube (see Fig. 4.4). To release them, the ice crystals are heated to +10 °C for 15 minutes.

Figure 4.4: Photo of an ice single crystal inside the plastic tube in which it was grown.

After that they are exposed to room temperature until the surface of the ice crystal starts melting and the crystal slides out. This procedure minimizes thermal and mechanical shocks to the crystal structure. The free ice crystal is returned to the cold room.

The first step in shaping a sample consists of cutting a disk-shaped piece of approximate 15 mm thickness from the crystal. Mechanical treatments like sawing are known to create a large amount of defects. For this reason the crystal was cut by heating it with hot wires. The drawback of this technique is that the ice is refreezing behind the wire if the cutting is done at sub-zero temperatures. This was solved by using a metal frame holding four parallel wires. In this way, the area of the ice crystal refreezing behind a wire is immediately cut by the following one. To maximize the heat production a high resistance wire was used for this purpose. Figure 4.5 shows two photos of the device.

A drawback of this technique is that a contamination of the fresh cut surface with particles from the wire can not be excluded. Therefore a large part of the crystal surface was molten with a hot aluminum plate and removed. Since most impurities are solvable in water, but not in ice, this treatment should remove all residues from the cutting process. The temperature of the aluminum plate was kept below +10 °C to reduce thermal gradients in the crystal. Applying higher temperatures can lead to the creation of large scale defects.

The samples were oriented on a two-circle x-ray diffractometer, operating with a sealed copper tube. The diffractometer was installed inside the cold room. The low penetration depth of the copper radiation makes the alignment of the ice crystals very difficult, since these are often covered by a layer of refrozen melt. This polycrystalline layer has large domains that are tilted with respect to the orientation of the bulk crystal rendering it often difficult to find the Bragg reflection of the bulk crystal. Because of this, the alignment of the crystal takes typically 24

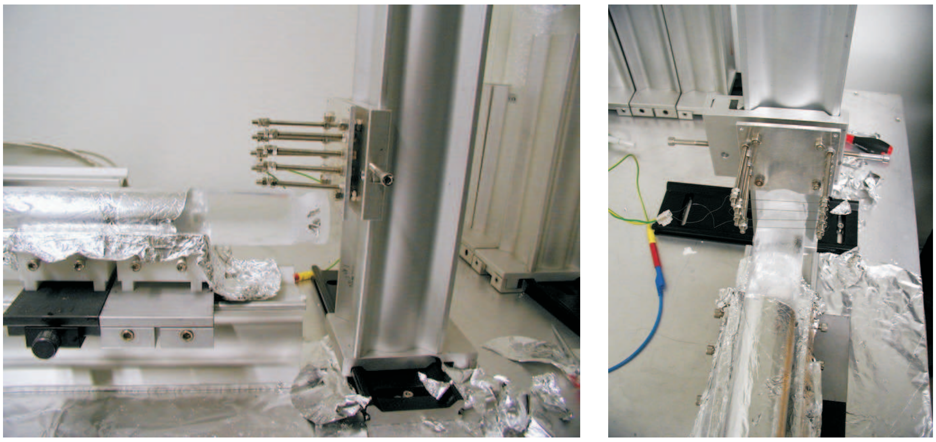

Figure 4.5: Photo of the device used to cut the ice single crystals. Since thermal cutting causes less stress to the crystal lattice a new tool was developed, that allows cutting at sub-zero temperatures.

hours. During this time the surface of the ice crystal is exposed to air and might be contaminated by dust and organic residues settling on the surface. The impurities were removed again by melting the exposed surface with a hot aluminum plate. The treatment was done in the same way as after the cutting (see above). A mechanical, non-motorized goniometer head is used to hold the ice crystal which allows to align the ice crystal within ±0.05°.

Bonding the substrate

The most critical part of the sample preparation is the fusion of the ice with the substrate. The resulting interface must be homogeneous and clean. The crystal lattice of the bulk ice should be retained at the interface. The microscopic parameters of the interface should be as similar as possible between different samples. This is accomplished by slowly melting the substrate into the ice crystal.

The substrate was placed on a clean aluminum plate that was mounted on an optical bench. The temperature of the aluminum plate was controlled by a peltier element. The plate could be translated with a micrometer screw. The goniometer head with the oriented ice crystal was mounted above the substrate on the same bench. The temperature of the aluminum plate was measured with a Pt-100 sensor.

The current of the peltier element was adjusted such that the temperature of the substrate surface was slightly higher than zero when contacting the ice. In this way only a very thin layer of ice touching the substrate surface, is molten. The substrate was slowly pushed into the crystal while taking care that the molten layer remained thin. When the substrate surface was completely immersed in the ice, the heating current was slowly decreased until the ice was completely refrozen. During this time the substrate was continuously translated further into the ice to keep the thickness of the molten ice small. This procedure ensures that the substrate surface is always hotter than the surrounding ice. Therefore, the recrystallisation of the molten layer starts from the ice single crystal side and the formation of polycrystalline domains at the interface is suppressed.

The optimum translation speed and temperature profile depend on the thermal conductivity of the substrate, which ranges from 1.36 $\frac{\mathrm{W}}{\mathrm{m \cdot K}}$ for silica glass [88] to 42 $\frac{\mathrm{W}}{\mathrm{m \cdot K}}$ for the sapphire substrate [89]. Due to these differences of more than an order of magnitude each sample behaves differently upon heating. Generally, substrates with low heat conductivity need high temperatures (the aluminum plate was heated up to +10 °C for the glass substrates) and slow translation speeds. Good heat conductors, like sapphire, fused quickly into the ice even at temperatures of only +3 °C.

4.1.3 Experimental chambers

Chamber with peltier cooling system

With the exception of the last experiment using self assembled mono layers, all samples were measured with the experimental chamber constructed by Simon Engemann. Sketches and photos of the chamber are shown in Fig. 4.6. The chamber consists of a hollow cylinder of aluminum. Inside the cylinder, the sample is held on an elevated platform. The platform is thermally insulated against the chamber by elevating it on struts produced from materials with low heat conductivity. The sample is clamped from two sides by copper sheets to ensure a stable position of the sample and good heat conductivity. The temperature of the sample is controlled by heating the copper clamps.

Heating and temperature control is achieved by peltier elements. Peltier elements are a fast and very accurate heating and cooling source. The heating power is controlled by a *Lakeshore 340* temperature controller, providing a temperature stability of ±1 mK. The backside of the heat producing peltier elements is chilled by a 1:1 water/glykol mixture through large aluminum heat exchangers. This fluid has the advantage of being cheap and non-toxic with an operating temperature range from -20°C to +50°C. Another advantage of glycol is that it is water solvable. The cooling fluid accumulates moisture from the air over the time of an experiment. Oil based cooling fluids suffer from the formation of ice particles, since the water can not be dissolved in the fluid. These particles may block pumping system and cause a failure of the cooling system. In glycol cooling fluid this only leads to a reduction of the glycol concentration, which can be corrected by refilling the cooling system with pure glycol. However, since the temperature of

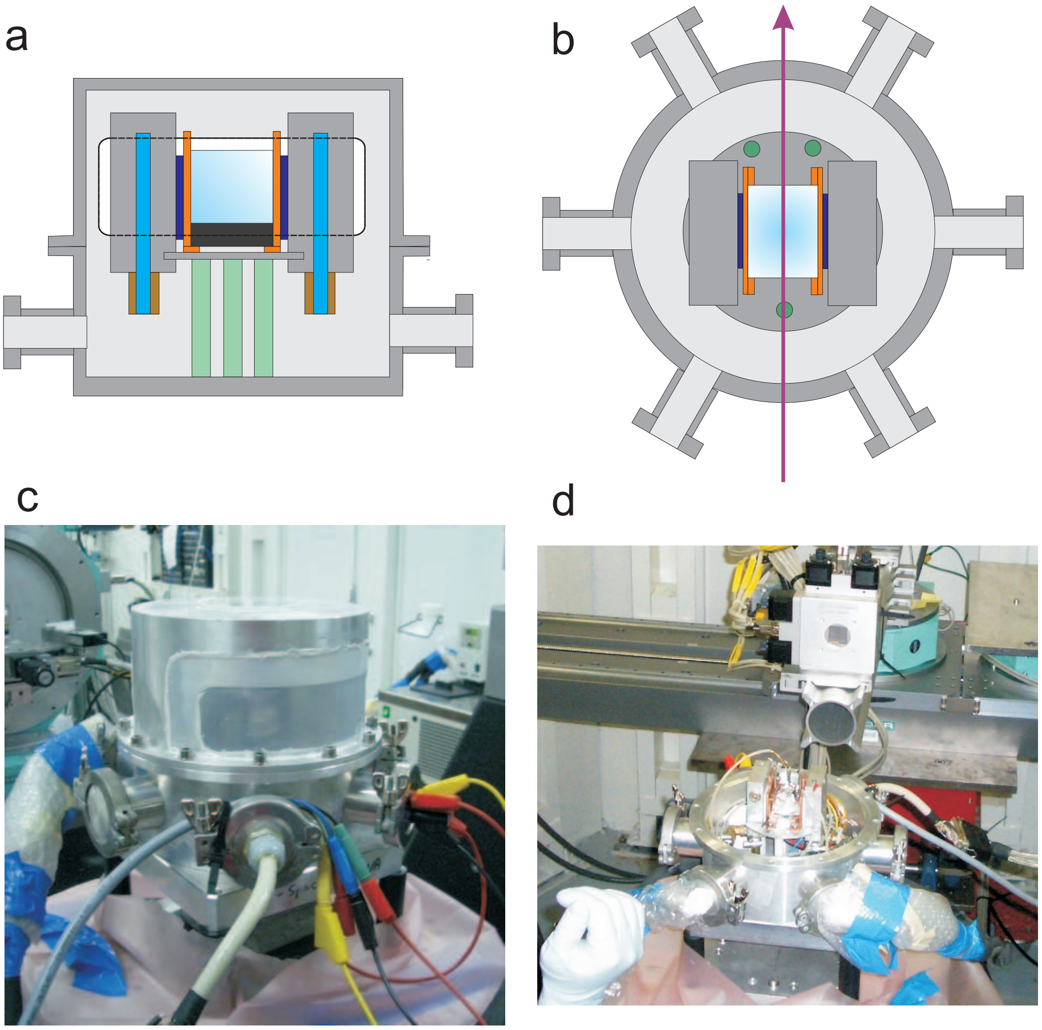

Figure 4.6: Sketch (top) and photos (bottom) of the sample chamber used in most of the experiments. a: Front view of the chamber. The ice crystal is on top of the substrate (brown). It is clamped from both sides by copper sheets (orange), that are in contact with the peltier elements (purple). A aluminum heat exchanger transfers the heat produced by the peltier elements to a closed cycle cooler. b: Top view. The arrow indicates the direction of the x-ray beam. The flanges are used for electrical and fluid feedthroughs. c: Photo of the chamber with the cover mounted. d: Photo of the open sample chamber.

the samples was close to zero during most of the experiment, refilling is necessary only once a week. The disadvantage of glycol is its high viscosity, which limits the cooling power of the closed cycle refrigerator.

Several Pt-100 sensors were attached at different places inside the chamber, allowing a careful monitoring of the temperature profiles inside the chamber. These sensors were calibrated to an absolute accuracy of approximately ±10 mK. An additional sensor was molten into the ice.

The chamber can be sealed with an aluminum top. Two large windows allow the beam to enter and exit the chamber. These windows are made of plastic to keep the absorption of the x-rays low while keeping moisture out of the chamber.

The advantage of this chamber is the large temperature range that can be covered, since the peltier elements can be used to cool or heat the sample beyond the temperature of the cooling liquid. In the experiments presented in this work the closed cycle refrigerator was set to -12°C. The peltier elements can produce a temperature gradient of up to 20 K, giving access to temperatures as low as -30°C. Using different cooling agents, it is possible to lower the temperature of the closed cycle refrigerator down to -30°C. Thus, sample temperatures as low as -50°C can be reached. Furthermore, the peltier elements allow an accurate control of the temperature, allowing measurements up to -0.005°C without melting the sample.

The main drawback of this chamber design is that large temperature gradients can occur inside the chamber. The heat conductivity of the aluminum housing is high increasing the air temperature inside the chamber up to +10°C. Since the sample is cooled only from two adjacent sides and the heat conductivity of the ice is low, temperature gradients may be established inside the sample. Employing this design it is difficult to accurately estimate the temperature of the ice interface. The presence of a sensor inside the ice does not change the situation since the heat conductivity of the ice is low and it remains unclear how much heat is transported through the interface. The error bars for the temperature measurements are discussed in detail in chapter 6.1.2.

Chamber with liquid cooling

The limitations mentioned above led to a different chamber design. The goal was to completely immerse the sample inside a fluid bath of homogeneous temperature, thereby eliminating any temperature gradients.

Photos and a sketch of the glass chamber can be seen in Fig. 4.7. The sample sits inside a primary cooling bath of n-heptane, which is not solvable and does not dissolve ice. The flow rate was small in order to keep the temperature around the sample as homogeneous as possible. All parts in contact with the heptane, including the tubing and the pump, are manufactured from materials which are easy to clean, like glass, stainless steel and teflon.

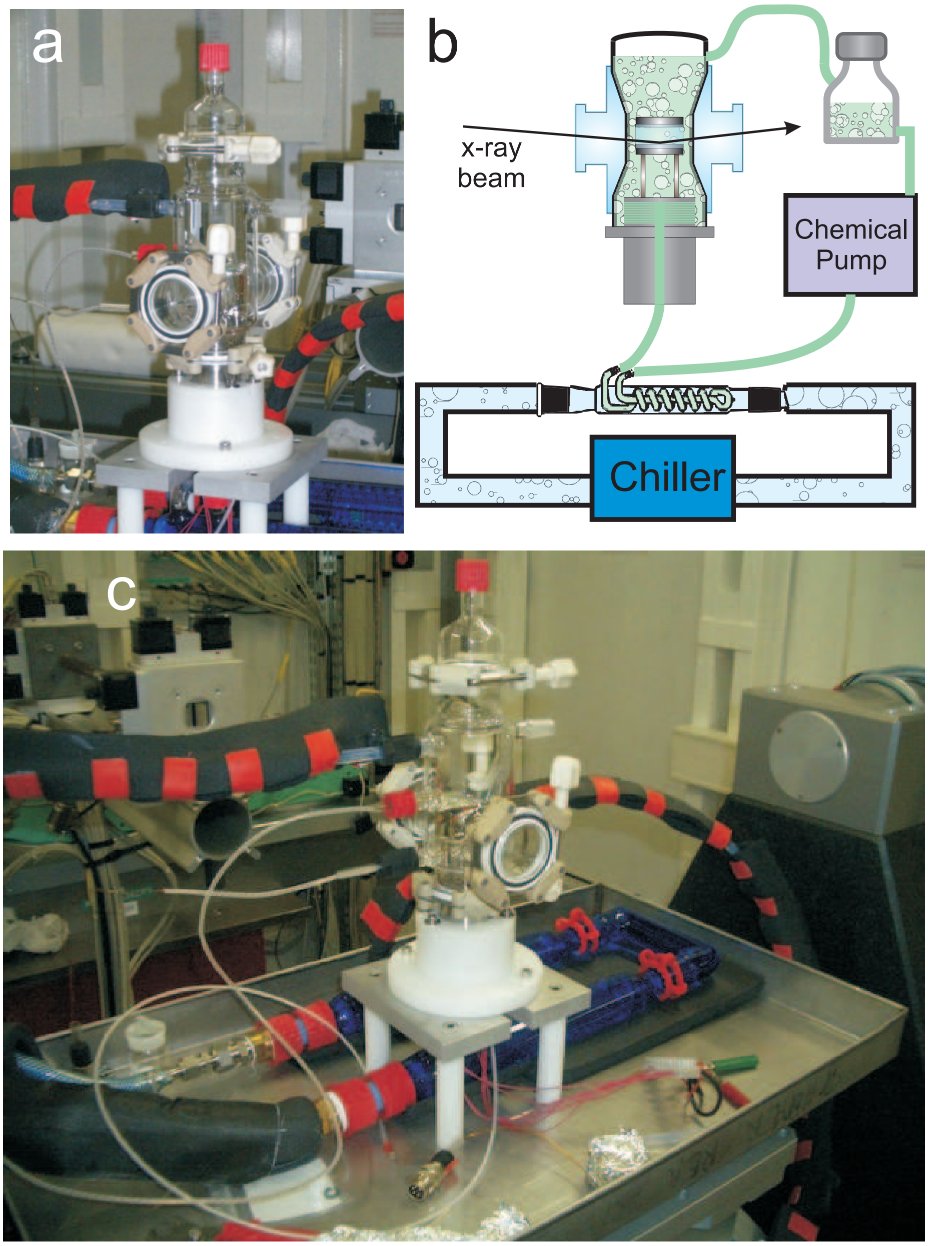

Figure 4.7: a,c: Fluid chamber used in the experiments on self assembled monolayers. The sample is completely immersed in liquid heptane (green in the sketch b). The temperature of the heptane was adjusted via a heat exchanger that is cooled by a secondary cooling circuit.

A secondary cooling cycle is used to control the temperature of the primary cycle. Since the fluid in this cycle is never in contact with the sample, a broad range of refrigerants can be used. For the measurements on self assembled monolayers, a glycol-water mixture was used. The heat is exchanged with the primary cooling cycle inside a glass heat exchanger. A Dimroth cooler was used for this purpose. The secondary cooling fluid is flowing around a glass spiral that contains the primary cooling fluid (heptane).

In addition, the temperature of the sample could be controlled by resistive heating of the stainless steel block where the heptane enters the chamber. Due to the large heat capacity and low thermal conductivity of the block, this method was too slow to accurately control the temperature. Therefore, only the heat exchanger was used to control the temperature. Two Pt-100 sensors monitor the temperature of the heptane before and after the sample. The temperature difference between the sensors was smaller than 0.5 K. The average value was taken as sample temperature. Even without electric heating it was possible to control the temperature up to ±0.1 K stability.

The glass chamber containing the sample and cooling fluid is surrounded by a second glass chamber that can be evacuated. This improves thermal isolation and inhibits the formation of ice on the outside of the chamber. The samples are inserted from the top of the chamber and can be replaced without draining the cooling fluid. A set of four alignment bolts allows quick, accurate and stable positioning of the sample, allowing sample exchanges in less than five minutes.

The main drawback of this chamber is the limited thermal range covered. It is not possible to reach temperatures below -20°C because the heat transfer between the two cooling cycles is not good enough. At high temperatures the low thermal stability limits access to temperatures above -0.1°C to avoid melting the sample.

4.2 High energy x-ray reflectivity

4.2.1 Beamline setup

White beam setup

All the data taken for this work have been measured at the high energy beamline ID15A of the European Synchrotron Radiation Facility (ESRF, Grenoble, France). The layout of the beamline is shown in Fig. 4.8. The synchrotron radiation is produced by an insertion device and passes the front end to enter the optics hutch 1, where the low energy part of the spectrum is removed. This reduces the heat load on the optical elements and increases the stability of the beam. Two Laue monochromators split off monochromatic beams into the side stations ID15B and ID15 C. This monochromators rest in a water cooled bath of indium-gallium to

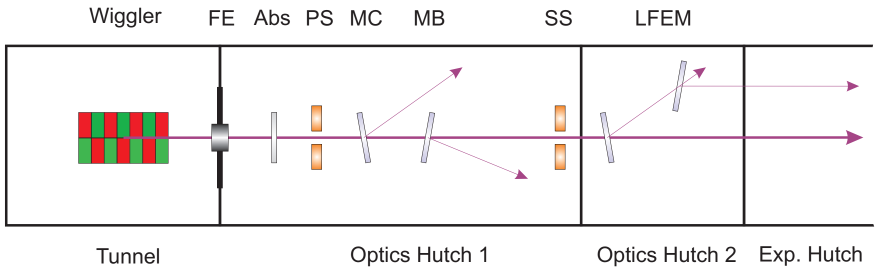

Figure 4.8: Schematic layout of the high energy beamline ID15. The radiation produced by the wiggler travels through the front end (FE). A water cooled Al-absorber (Abs) removes the low energy part of the spectrum. The primary slits (PS) define the beamsize for all experimental end stations. The beams for the side stations ID15C and ID15B are split from the main beam by the monochromators MC and MB, respectively. The secondary slits (SS) define the beam entering the second optics hutch. For experiments using a monochromatic beam a Laue fixed exit monochromator (LFEM) is installed in optics hutch 2.

avoid thermal drifts due to radiation heating. The primary slits define the size of the beam entering the hutch. The secondary slits define the beam size of the main beam in the hutch of ID15A. Experiments in this hutch can use either or simultaneously the white beam and a monochromatic beam that is produced by the Laue fixed exit monochromator in the optics hutch 2 (see Fig. 4.10). Due to the low absorption of high energy x-rays in air, only the tunnel and the optics hutch 1 use vacuum beampipes.

The x-ray source used in all the experiments is an asymmetric multipole wiggler (AMPW). The photon flux $\Phi(E)$ is defined as the number of photons that are emitted in one second into a solid angle of 1 milli steradian, normalized for 100 mA of electron beam current and 0.1% bandwidth. The spectrum of the radiation emitted by the wiggler along the beam axis is shown in Fig. 4.9. The opening cone of the radiation from the high energy wiggler is large, producing a large beam at the sample position 70 m from the source. Defining the beam size by a small gap in the secondary slits renders a spatially uniform beam profile. A 0.4 mm thick, water cooled aluminum filter is used to remove the low energy part of the spectrum. The resulting flux after transmission through the front end window (Beryllium window), the aluminum filter and the monochromator crystals for the B and C hutches is shown in Fig. 4.9. The integrated flux of the white beam is

$$\varphi = I \mathrm{d}\Omega \int \Phi(E) T(E) \,\mathrm{d}E. \tag{4.1}$$

$T(E)$ denotes the transmission of the beamline optics for that energy. I is the storage ring current, $\mathrm{d}\Omega$ is the solid angle under which the radiation is emitted.

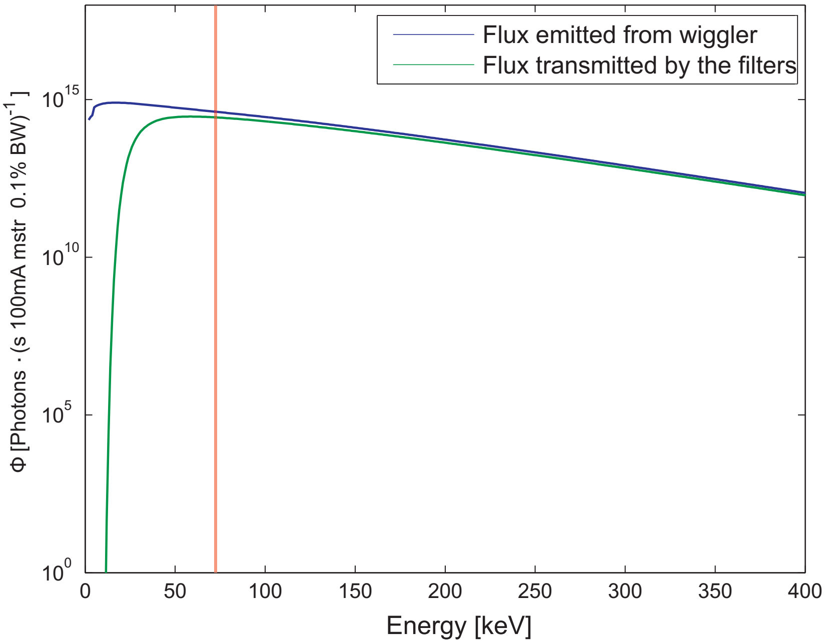

Figure 4.9: Photon flux at beamline ID15A. The blue line shows the flux emitted from the wiggler source. The green line shows the flux that is transmitted through the filters. The filters remove the low energy part of the radiation, while leaving the high energy radiation unchanged. The red line marks the energy 72.5 keV, at which the experiments presented in this work have been performed.

It is defined by the height (H) and the width (W) of the secondary slits and their distance (D) to the source, thus $d\Omega = \frac{H \cdot W}{D^2}$.

From the beam lifetime τ, the time between refills T_{refill}, and the current after refill I_0, the average storage ring current

$$\bar{I} = \frac{1}{T_{refill}} \int_0^{T_{refill}} I_0 e^{-\frac{t}{\tau}} \mathrm{d}t = \frac{I_0 \tau}{T_{refill}} \left(1 - e^{-\frac{T_{refill}}{\tau}}\right) \tag{4.2}$$

can be calculated. In uniform mode, with 1 mm^2 secondary slit gap, the average integrated white beam flux is

$$\bar{\varphi} = 1.73 \cdot 10^{16} \, \frac{\text{Photons}}{s}. \tag{4.3}$$

Note that for large openings of the secondary slits, the spatial profile of the white beam is not uniform. For the experiments presented in this work the secondary slit opening was always smaller than 1 mm x 1mm, producing a uniformly flat beam in experimental hutch A.

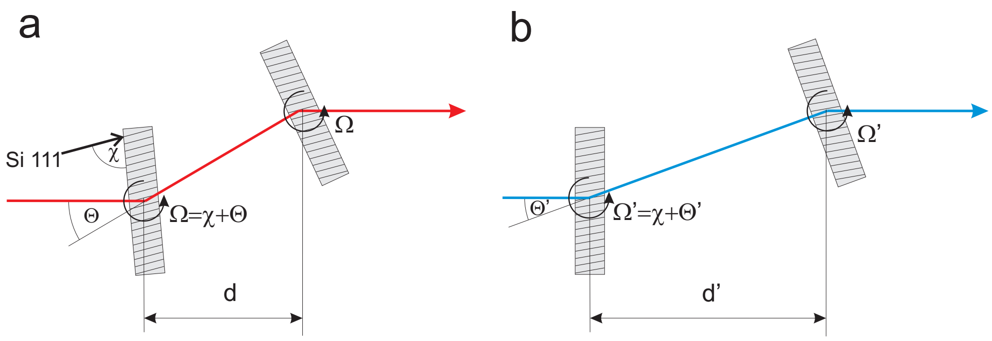

Figure 4.10: Sketch of the Laue fixed-exit monochromator used in ID15A. The energy is changed by rotating the two monochromators and changing the distance between them, thereby keeping the position of the monochromatic beam constant.

Monochromator

The reflectivity experiments were carried out with a monochromatic beam, at an energy $E = 72.5$ keV. Two asymmetrically cut and bent Laue monochromator crystals are used in fixed-exit Laue geometry (see Fig. 4.10). Unlike Bragg monochromators, Laue monochromators are used in transmission geometry. The Si (111) reflection was used for the experiments. The asymmetric cut χ, denoting the angle between the lattice planes and the crystal surface, of the Si (111) planes is $\chi = 36.74°$. The lattice spacing for silicon (111) is $2d$ = 6.2712 Å[90], resulting in a Bragg angle of the monochromators of 1.5626° for 72.5 keV radiation.

The primary intensity can be increased by increasing the energy bandwidth. For asymmetrically cut and bent crystals the energy bandwidth $\Delta E/E$ is given by [91, 92]

$$\frac{\Delta E}{E} = \frac{D\tan\chi}{\rho\sin 2\theta}\left[2 + (\cos 2\theta + \cos 2\chi)\left(1 - \frac{s_{23} + s_{34}\cot\chi}{s_{33}}\right)\right] \qquad (4.4)$$

with the crystal thickness D, the bending radius ρ and the crystallographic orientation dependent elastic compliances s_{ij}. By optimizing the free parameters in Eq. 4.4 the bandwidth can be increased to find an acceptable compromise between the monochromaticity $\frac{\Delta\lambda}{\lambda}$ of the beam and the transmitted intensity. The contribution of the energy bandwidth to the resolution of the measurement will be discussed in section 4.2.2. In the configuration used for the reflectivity experiments, the energy bandwidth has been set to $\frac{\Delta E}{E} = 3\cdot 10^{-3}$.The fixed-exit geometry allows to change the energy without changing the direction or the position of the monochromatic beam by rotating and translating the two Laue monochromator crystals. Note, that the optics setup described above does not allow to suppress higher harmonic radiation ($\lambda/3$, $\lambda/4$, ...).

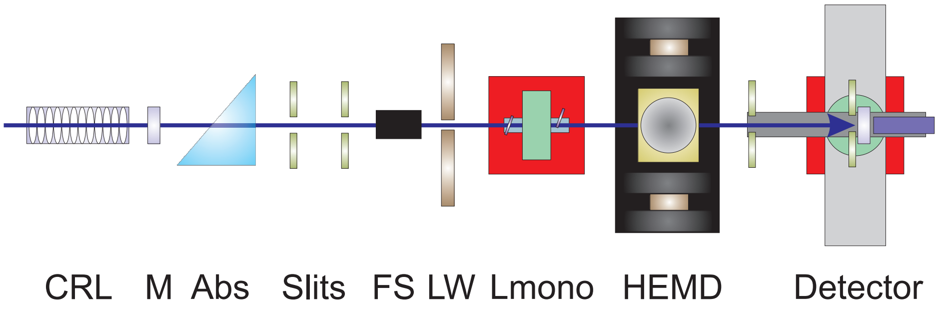

Figure 4.11: Sketch of the experimental setup used in high energy x-ray reflectivity experiments.

4.2.2 High energy reflectivity setup

A sketch of the reflectivity setup is shown in Fig. 4.11. The monochromatic beam enters the experimental hutch ID15A. The first optical element there is a compound refractive lens (CRL) that focuses the beam on to the sample. A semiconductor diode is used to monitor the beam transmitted by the lenses (M). At low angles the intensity of the beam reflected from the sample is too high for the detector. For this reason a continuous wedge absorber (Abs) is used to attenuate the beam. Two 4 sector tungsten slits (Slits) and a lead wall with a pin hole (LW) remove the background radiation produced by the optical elements. A fast shutter (FS) can be brought into the beam. This device ensures that the sample is only illuminated when the detector is counting thereby minimizing the dose on radiation sensitive samples.

The heart of the setup is the High Energy Microdiffractometer (HEMD), which was designed by Harald Reichert and installed in the experimental hutch of ID15A in January 2005. It is designed for high energy surface and interface scattering experiments. The use of an additional set of monochromator crystals (Lmono) allows to investigate liquid surfaces and liquid-liquid interfaces by inclining the primary beam in the vertical plane, which is not possible at standard surface diffraction beamlines using a fixed incident beam. This additional monochromator was not used in the experiments presented in this thesis. The reflected beam is detected by a scintillation counter mounted on a separate detector stage behind the diffractometer (Detector).

Compound refractive lenses

The surface are of the sample illuminated by the beam is called the *footprint*. The width of this area is equal to horizontal beam size. The length of the footprint f

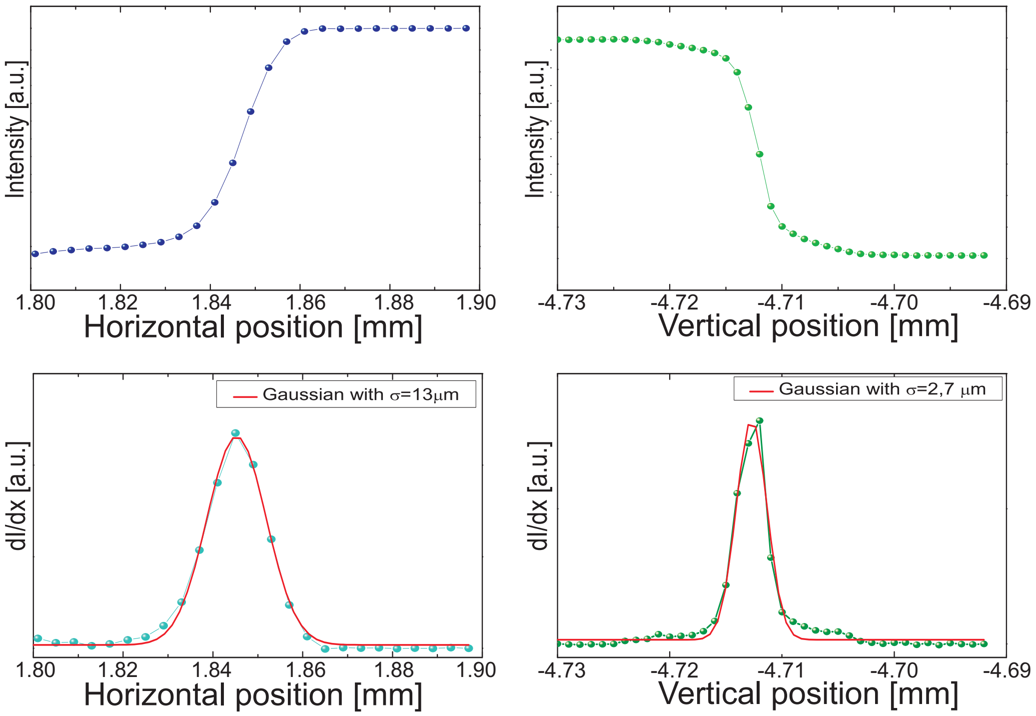

Figure 4.12: Horizontal (left) and vertical (right) beam profile. The top row shows the results of knife-edge scans. The bottom row shows the derivatives of the intensity and fits with a Gaussian, indicating a beam size of 15 $\mu\mathrm{m}$ horizontally and 3 $\mu\mathrm{m}$ vertically.

depends on the vertical beam size ζ_v and the incident angle θ_i

$$f = \frac{\zeta_v}{\sin\theta_i}. \tag{4.5}$$

The part of the x-rays that do not illuminate the sample are lost and only contribute to the background. For this reason, it is important to keep the footprint smaller than the sample surface. However, since high energy x-ray reflectivity experiments are performed at small incident angles (the edge of total reflection appeared at incident angles of approximately $0.02°$), microfocusing is needed.

An aluminum CRL composed of 218 lenses with a focal length of 4.7 m allows to focus the beam in two dimensions. The CRL is mounted on a translation stage that allows to move it in and out of the beam without loosing alignment. The size of the focal spot depends on the size and stability of the electron beam in the storage ring. The measurements have been performed with horizontal spot sizes of 20 $\mu\mathrm{m}$ and vertical spot sizes of up to 3 $\mu\mathrm{m}$ (see Fig. 4.12). 4 $\mu\mathrm{m}$ spot sizes have routinely been obtained.

Figure 4.13: Low-Z absorbers used in x-ray reflectivity experiments, including a bucket of water (left) and a plexiglass wedge (right).

Absorber

The signals measured in x-ray diffraction and refraction often span a large dynamic range. A typical reflectivity measurement carried out at the HEMD diffractometer covers nine to ten orders of magnitude. This is much higher than the dynamic range of any single photon counting detector. Attenuators need to be used to cover the full experimental data range. Several types of absorbers have been tested, ranging from lead plates to leaded glass, aluminum wedges and simple buckets filled with water (see Fig. 4.13). There are three criteria that an absorber should fulfill.

1. The attenuation should be reproducible.
2. The whole dynamic range of the incident beam should be covered.
3. Beam hardening (the ratio of higher harmonic radiation to the fundamental radiation) should be avoided.

The first two requirements can be fulfilled with most well-designed absorbers. The third requirement can be satisfied by the use of materials with low atomic numbers, for which the ratio of absorption between the different wavelengths ($\lambda/3$, $\lambda/4, \ldots$) in the primary beam does not change significantly. After encouraging results were obtained with a bucket of water, a Plexiglas wedge was inserted in the beam. Consisting mainly of carbon and hydrogen, this absorber causes negligible beam hardening. The disadvantage of this absorber is the large dimension resulting from the large absorption length of these materials (see Fig. 4.13).

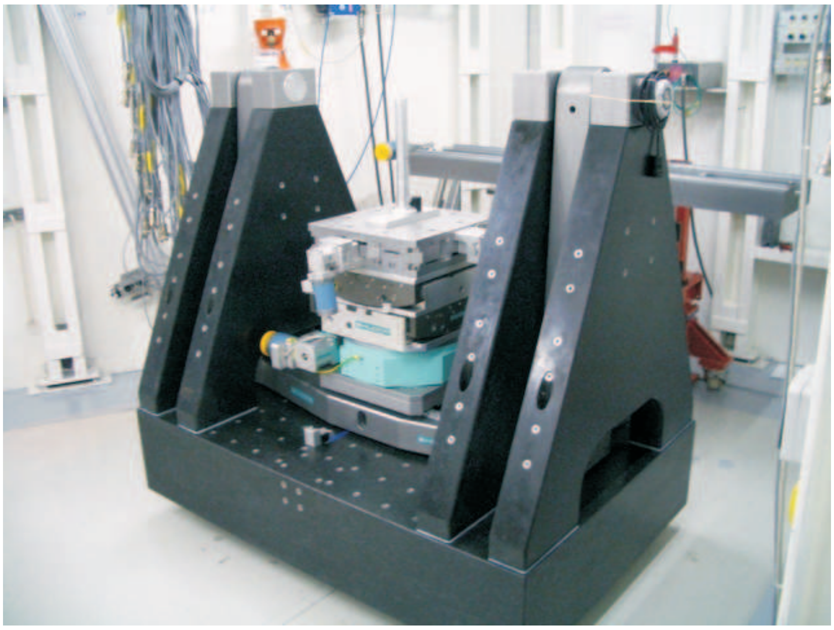

Figure 4.14: Photo of the HEMD diffractometer. The vertical translation table is not mounted. The four granite towers hold on their top the bearing for the cradle.

High Energy Microdiffractometer

Figure 4.14 shows a photo of the diffractometer. The base consists of a granite block with four granite towers. The motorized positioning devices are mounted on a large swing which is resting on top of the granite towers in four precision bearings. The swing is used to define the angle between the surface of the sample and the incoming beam, Θ. The precise value of the angle Θ is very important for all grazing incidence surface diffraction experiments, since it defines the penetration depth of the x-ray wavefield into the sample. Furthermore, high precision in Θ is needed to follow the specular reflection of the sample in x-ray reflectivity. The high precision is obtained by a high resolution linear translation pulling or pushing the swing. The precise value of the diffractometer inclination is then measured by an encoder. This technique allows to control Θ within $10^{-4\circ}$.

Several motorized positioning devices are mounted on the base plate of the swing in stack. Each of these stages has been especially designed for this instrument. The lowest motor stage is a linear translation that allows to translate the whole tower horizontally to the beam with an accuracy of 0.1 μm.

The second device rotates the sample around the vertical axis. This rotation stage can access the full 360° with an accuracy of 0.005°. Two tilt stages are mounted on the top of this rotation that allow alignment the sample surface with respect to the beam with an accuracy of $10^{-3\circ}$ in a range of ±3°.

Two horizontal linear translations allow to positioning of the sample in a range of ±25 mm within a micron. The top most device is a high precision vertical translation used to position the sample surface in the beam. The instrument can be operated with microbeams (see section 4.2.2). This forces a vertical positioning of the sample with sub-micron resolution. Since the instrument is designed for heavy duty sample environments up to 500 kg, a special design for the vertical translation is needed. This is accomplished by a pair of wedges. The horizontal translation of these wedges is converted into a high-resolution vertical translation. The motion is monitored by an encoder, allowing a vertical positioning of the sample assembly within 200 nm.

For highest flexibility in the experiments the diffractometer has to accommodate different sorts of sample environments. Especially in the case of ultra-high-vacuum (UHV) chambers, these setups can be very heavy. Therefore, the diffractometer has been designed to take loads up to 500 kg without loss of accuracy.

The heavy design of the diffractometer as well as the heavy shielding of the ID15A hutch act as effective passive vibration dampers. For most surface experiments no additional active vibration damping is needed. For particular vibration sensitive experiments, like observations of liquid surfaces, the diffractometer tower can be equipped with a vibration isolation stage (Model TS-150 from *Table Stable*). This module dampens all translational and rotational vibrations actively in a frequency range from 0.7 Hz to 1 kHz and passively beyond [93].

Detector table

The position of the detector in respect to the incident beam on the sample defines the momentum transfer probed in the experiment. It is obvious that it requires high accuracy to conduct high quality experiments. The HEMD setup is designed to work with two sorts of detectors, scintillation counters and 2D area detectors.

Point counters measure the amount of radiation scattered by the sample into a defined solid angle. The solid angle is equal to the resolution of the instrument. The detection area is defined by two pairs of tungsten blades (detector slits, 4.16). A resolution of $5 \cdot 10^{-4\circ}$ can be obtained. Two additional pairs of blades (collimator slits) are mounted 50 cm in front of the detector slits. Collimator slits reduce the background by stopping radiation not originating from the sample. In high energy scattering experiments a high level of secondary Compton scattering is produced which is not originating from the sample. Since this radiation can hit the detector from all sides, additional lead shielding elements are installed on the detector arm. Figure 4.15 shows a photo of the detector arm.

The detector should move on a circle around the center of rotation of the diffractometer. Since the detector can not be mounted on and positioned by a circular diffractometer arm with sufficient accuracy, the detector motion is instead

Figure 4.15: View of the detector arm. The detector elements are mounted on a X-95 rail. The lower part of the picture shows the rotation stage and the linear translation, which are combined to mimic the horizontal scattering angle.

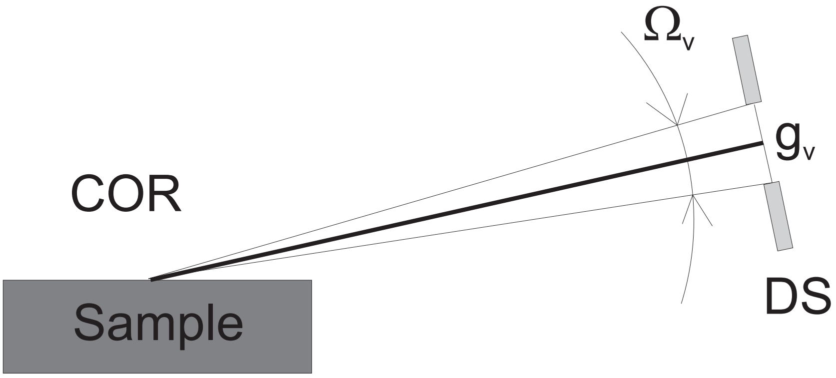

Figure 4.16: The angle Ω_v, i.e. the vertical resolution, is defined by the slit gap g_v of the detector slit blades (DS) and the distance to the center of rotation (COR) at the sample position.

realized in a different way. The detector is mounted on a table, where the front and back legs can be moved independently with a high accuracy. High energy scattering experiments cover typically only a small angular range. In this range tilting the table in combination with a change of the table height is a good approximation of the circular movement. The horizontal movement of the detector is realized by a horizontal translation on a rail and a rotation of the detector around the detector slits. It is important to know the sample-detector distance very accurately to calculate the movements correctly.

For the actual detection of the x-rays two different point counters are employed. For high flux ($> 10^6$ cps) a solid-state diode is used, where the x-rays create electron-hole pairs in the pn-junction inducing a current that is measured by a high accuracy ampere meter. The diode suffers from an intrinsically high dark current and does not provide energy resolution.

For low count rates ($< 10^5$ cps) a single photon scintillation detector can be used. Applying a deadtime correction count rates up to $2.5 \cdot 10^6$ cps are acceptable. The energy resolution of the detector allows to electronically filter the higher harmonics. Exposure of the scintillation center to a high flux can damage the detector. An absorber (see section 4.2.2) must be used to attenuate strong signals.

The momentum transfer range accessible in an experiment is limited by the angular range of the detector arm. The HEMD detector stage offers a vertical angular range from -2° to +7°. At a typical energy of 70 keV this corresponds to a momentum transfer range of up to 4.3 Å^{-1} (reflecting to positive detector angles). Some experiments require measurements in negative direction, where the specular beam is deflected downwards. In this case a vertical momentum transfer of only 1.2 Å^{-1} is accessible.

A two-dimensional detector can be mounted on the rail next to the detector arm. This allows easy transfer between the two detectors without loosing alignment. High energy scattering experiments are especially suited for the use of 2D detectors, since the Ewald sphere is almost flat. This allows to map planar sections and lines in reciprocal space in a single exposure.

Instrumental resolution

The resolution is a very important property of a reflectivity experiment. Details of the reflectivity curve that are smaller than the instrumental resolution will be washed out. Care must be taken to insure that the resolution is better than the highest frequency oscillations on the reflectivity curve. On the other hand a resolution element which is smaller than the smallest details on the curve reduces only the signal without gaining new information.

The momentum transfer probed by a reflectivity experiment ($\Theta_i = \Theta_e = \Theta$)

is

$$Q = \frac{2\pi}{\lambda}\left(\sin\Theta_i + \sin\Theta_e\right) = \frac{4\pi}{\lambda}\sin\Theta, \tag{4.6}$$

with the wavelength λ and the angle of incidence of the incoming and exit beams Θ_i and Θ_e, respectively. In high energy reflectivity experiments the incident and exit angle are very small. Therefore the approximation

$$Q = \frac{2\pi}{\lambda}\left(\Theta_i + \Theta_e\right) \tag{4.7}$$

is valid. The resolution is obtained by taking the total derivative of the momentum transfer

$$\Delta Q = \left(\Delta\lambda\frac{\partial}{\partial\lambda} + \Delta\Theta_i\frac{\partial}{\partial\Theta_i} + \Delta\Theta_e\frac{\partial}{\partial\Theta_e}\right)Q, \tag{4.8}$$

with $\frac{\Delta\lambda}{\lambda} = \frac{\Delta E}{E}$ being the energy bandwidth of the radiation, $\Delta\Theta_i$ the divergence of the incoming beam and $\Delta\Theta_e$ the detector resolution. Using Eq. 4.7, the total resolution is given by

$$\Delta Q = \frac{\Delta\lambda}{\lambda}Q + \frac{2\pi}{\lambda}\left(\Delta\Theta_e + \Delta\Theta_i\right). \tag{4.9}$$

The first term in Eq. 4.9 depends on the energy bandwidth which is determined by the properties of the monochromator crystals (see Eq. 4.4). An optimum has to be found between intensity and monochromaticity of the beam. In the experiments presented in this work the bandwidth was typically $\frac{\Delta\lambda}{\lambda} \approx 3 \cdot 10^{-3}$, giving a momentum transfer resolution of $5 \cdot 10^{-3}$ Å^{-1} for the highest momentum transfers probed.

The divergence $\Delta\Theta_i$ of the incoming beam depends on the x-ray optics used. The strong focusing of the beam leads to an increased divergence (see Fig. 4.17). The divergence of the beam can be measured by scanning the detector around the primary beam. Using the focusing optics, the beam divergence is approximately five millidegrees (see Fig. 4.18), giving a resolution element of $2.1 \cdot 10^{-3}$ Å^{-1}.

The detector resolution $\Delta\Theta_e$ is defined by the gap of the vertical detector slits (see above)

$$\Delta\Theta_e = 2\arctan\left(\frac{g_v}{2L}\right). \tag{4.10}$$

Setting a narrow detector slit gap makes the instrument more vulnerable to misalignment. If the surface of the investigated sample is not perfectly flat, i.e. rounded or bent, the exit angle of the reflected beam broadens. In this case the detector gap has to be opened enough to fully integrate the reflected beam at all positions. The reflectivity curves shown in this work were measured with a vertical detector gap of 0.1 mm, leading to a resolution of $1.5 \cdot 10^{-3}$ Å^{-1}.

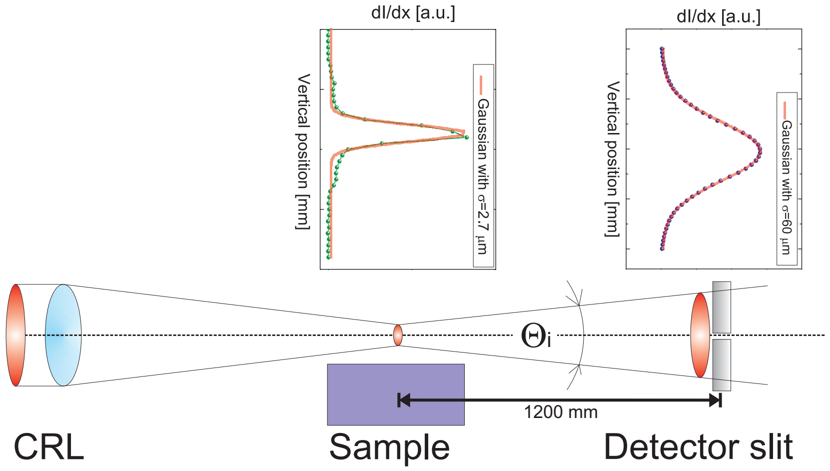

Figure 4.17: Divergence of the beam. The CRL focuses the beam to a vertical spot size of 2.7 $\mu\mathrm{m}$ at the sample position. At the position of the detector slit, 1.2 m away, the beam has broadened to 60 $\mu\mathrm{m}$.

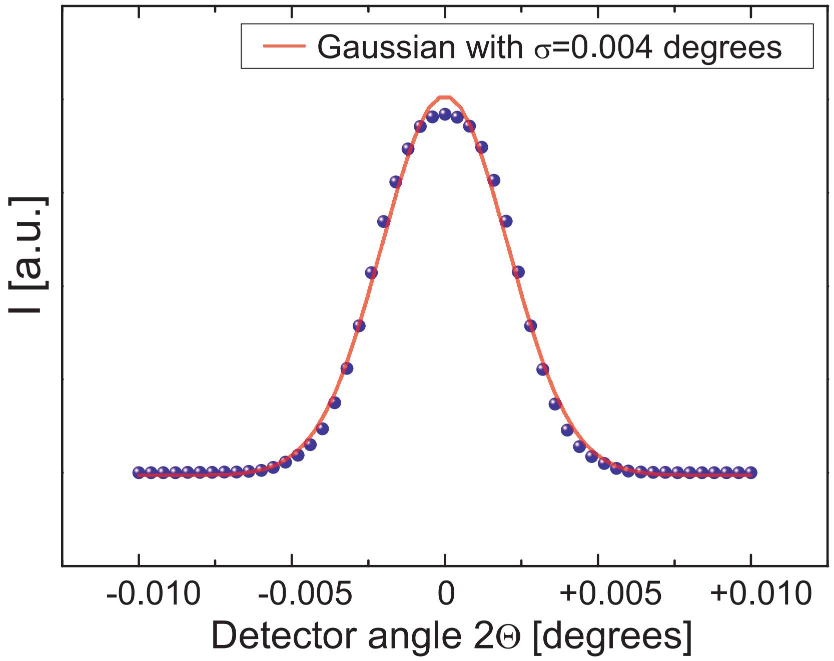

Figure 4.18: Measurement of the angular beam divergence. The detector is scanning the primary beam.

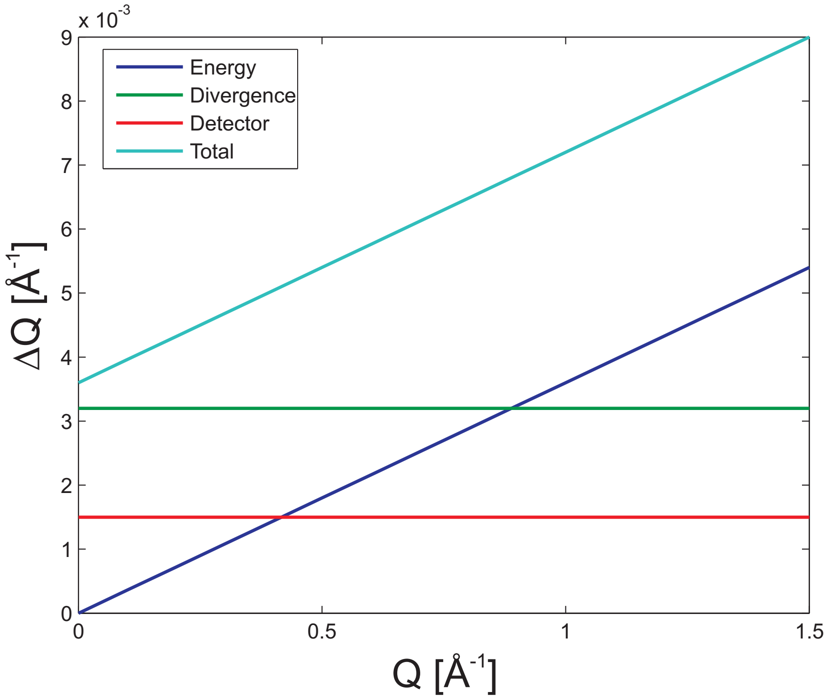

Figure 4.19: Total resolution and the three contributions of the HEMD setup as a function of the vertical momentum transfer.

The total resolution element is shown in Fig. 4.19 as a function of the momentum transfer Q. For low momentum transfers the total resolution is mostly defined by the beam divergence and the choice of the detector slit gap. For momentum transfers greater than 0.5 $Å^{-1}$ the resolution element coming from the polychromaticity of the beam becomes the largest element. The instrumental resolution becomes decreases with increasing momentum transfer, up to a value of 10^{-2} $Å^{-1}$ for the largest momentum transfers probed.

4.3 Data analysis

High energy x-ray reflectivity is the only technique that can probe the electron density profile of deeply buried interfaces. This opens the technique of x-ray reflectivity to new classes of systems such as the ones presented in this work. The drawback is that one has to deduce the physical properties of the system without access to complementary techniques.

The reflectivity curve of a given electron density profile can be uniquely calculated by the algorithms described in chapter 3.5. However, it is not possible to uniquely derive the electron density profile from a given reflectivity curve. For reflectivity curves without pronounced features many different electron density profiles can be found, that reproduce the data set. Uncertainties in the data, such as the height of the plateau of total reflection, can cause serious misinterpretation of the data.

In traditional surface science this drawback of reflectivity analysis can often be compensated by using complementary techniques, like grazing incidence diffraction or electron spectroscopy. However, for a buried interface these techniques are not available. For these reasons the analysis has to be done in two steps.

1. Find an electron density profile that fits the reflectivity data and is not unphysical.

2. Exclude all other density profiles that can be fit to the data.

For one-layer systems, like the interface melting between ice and oxide substrates, the second point is easy since the data can be analyzed in a straight forward way. For complex, multi-layered systems, like the self-assembled monolayers, the second condition is very hard to fulfill.

The complete data analysis has been done using the program language *matlab*. All the fitting routines and raw data processing was done with self-written programs. The first step is the raw data analysis, assembling the full reflectivity curve from the measured intensities during the experiment. The second step consists of fitting different electron density profiles to the reflectivity curve.

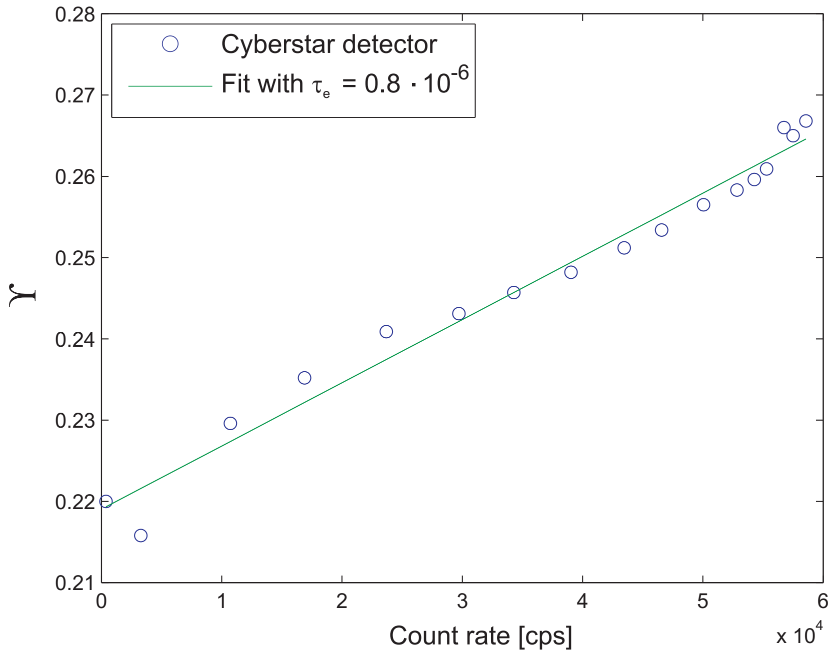

Figure 4.20: Determination of the detector dead time. A signal is measured with (N_a) and without (N_0) attenuation. The ratio $\Upsilon = \frac{N_a}{N_0}$ is plotted as a function of N_0. The slope of the line fitted to the data is equal to the time constant of the detector τ_e.

4.3.1 Raw data analysis

Due to the limited dynamic range of the detector (see section 4.2.2) the reflectivity curve can not be taken in a single scan. Parts with high intensities need to be measured with attenuators, while parts with low intensities need higher counting times. In the raw data analysis the complete reflectivity curve is assembled from these individual scan files. Furthermore, the background has to be subtracted from the data, the detector has to be corrected for dead time effects and geometrical effects at low angles have to be taken into account.

Dead time correction

Quantum detectors suffer from dead time effects when they are exposed to high count rates. The detector dead time is the time after the detection of a photon, during which the detector is unable to detect new photons. This leads to a non-linear detection function (the number of detected counts N_0 as a function of the incident counts N_t), where the number of photons that is detected is smaller than the photons that have actually reached the detector. This effect can be corrected

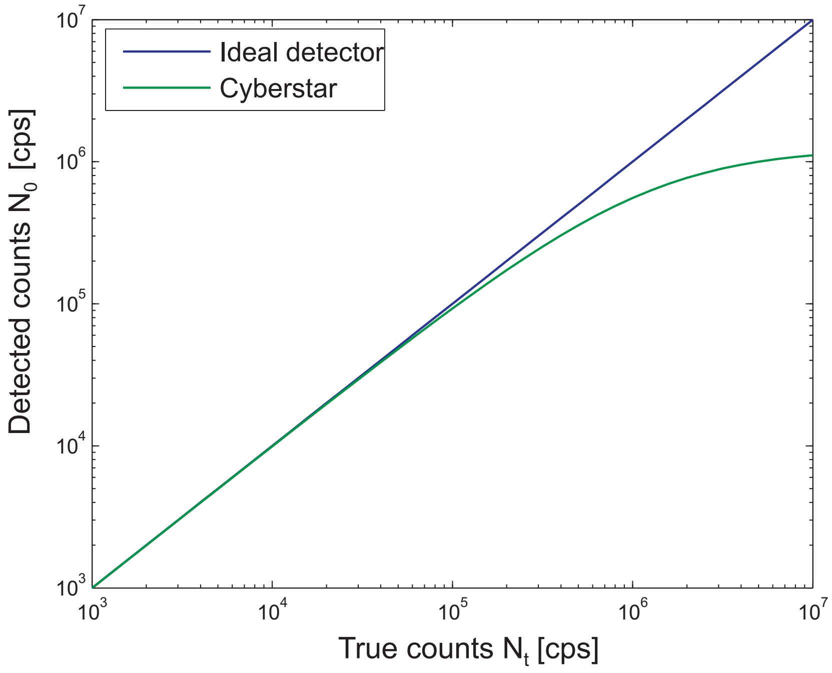

Figure 4.21: Calculated detection function for an ideal detector (blue) and a detector with time constant $\tau_e = 0.8 \cdot 10^{-6}$ (green). At high intensities the detector with dead time begins to saturate.

by

$$N_t = \frac{N_0}{1 - N_0 \tau_e}, \tag{4.11}$$

with the time constant of the detector τ_e. For the detector used in this work the time constant is $\tau_e = 0.8 \cdot 10^{-6}$ (see Fig. 4.20). The detection function for this time constant is shown in Fig. 4.21. The detector can be operated without correction (this means $N_t \approx N_t$) up do 80 000 counts per second (cps). Equation 4.11 is valid up to 200 kcps. At count rates above 1 Mcps the detector becomes unreliable and the counting electronics can be damaged.

Background subtraction

There are two types of background that have to be taken into account in a scattering experiment. External background describes the general background in the experimental hutch generated by radiation scattered in air or from optical elements. Internal background is produced inside the sample by inelastic (fluorescence and Compton scattering) and elastic (diffuse scattering) scattering processes.

A number of optical elements are installed in the experimental setup in order to prevent external background radiation from entering the detector (see section 4.2.2). The background can be suppressed to values as low as a few counts per second. Nevertheless, for faint signals at high momentum transfers it is necessary to carefully measure the background and subtract it from the signal.

The internal background was measured by misaligning the horizontal detector angle (measuring at non-zero in-plane momentum transfer) or misaligning the sample tilt to avoid the specular reflection. The background was directly subtracted from the reflectivity signal. In cases where the number of background points was not the same as the number of points in the reflectivity curve spline interpolation was used for subtraction.

Assembly of the reflectivity curve

The best way to account for the effect of attenuators in the beam is to accurately measure the attenuation factors and correct the raw data accordingly. Unfortunately, the attenuators used in the experiments presented in this work did not allow to deduce reproducible attenuation factors. For this reason segments of the reflectivity curve measured with different attenuators were measured with overlapping parts. The scaling factors between different segments of the reflectivity curve were then determined manually to produce the optimal overlap between two scans.

Problems at low momentum transfer values

It was not always possible to reproducibly measure the edge of total reflection. At high energies and with the low-Z materials used in these experiments, the edge of total reflection is shifted to very small angles. This region of the measurement is especially prone to misalignments and sample imperfections. The intensity of the edge can vary by a factor of two between two scans because the beam is not hitting exactly the same spot on the sample. For this reason the low momentum transfer part of the reflectivity curve was excluded from the fitting.

For small angles of incidence Θ a so-called illumination correction (also called footprint correction) has to be applied taking into account that at low angles the footprint of the incident beam is larger than the sample and consequently only part of the incident beam is reflected. This leads to a reduced intensity observed in the detector. Assuming a simplified box shaped beam profile this effect can be corrected for by dividing the measured intensity by

$$\Xi = \begin{cases} \frac{L}{h_v}\sin\Theta & \text{for } \frac{L}{h_v}\sin\Theta < 1 \\ 1 & \text{else} \end{cases} , \tag{4.12}$$

with the vertical beam size h_v and the sample length L. For a 20 mm sample and a vertical beam focus of 5 $\mu\mathrm{m}$, the beam is fully illuminating the sample at 0.02 Å^{-1}. Since this part of the reflectivity curve has to be excluded from the fitting because of the above mentioned problems, the illumination correction is not needed.

4.3.2 Fitting algorithms

The goal of a fitting algorithm is to find the electron density profile that fits best to the measured data. Fitting reflectivity data is difficult because the function χ^2, which measures the quality of the fit, has many local minima and strong correlations between different fitting parameters. Two completely different approaches have been used in this work, a simulated annealing algorithm and a genetic algorithm.

Simulated annealing algorithm

Simulated annealing algorithms were developed especially for systems exhibiting many local minima [94]. The basic idea is to perform a random walk in the parameter space. After each step the algorithm checks the quality of the fit χ^2 at its new position. If the quality is better, the new position serves as a starting place for the next step. If it is worse, the step is only done with a certain probability p, allowing the algorithm to overcome hills in the χ^2 landscape to find the global minimum.

Taking an analogy from physics, the quality difference between two steps can be interpreted as an energy difference. Therefore, a Boltzmann distribution is used to calculate the probability p

$$p = \exp\left(\frac{\chi^2_{n-1} - \chi^2_n}{k_B T}\right). \tag{4.13}$$

This probability depends on the virtual temperature of the system T. The Boltzmann constant k_B is written into Eq. 4.13 only for the physical analogy and can be set to an arbitrary value. The algorithm starts with a high temperature value. The probability of moving to higher χ^2 values is high and the algorithm can easily pass hills in the parameter space. Iterating the algorithm the temperature is slowly decreased, forcing the fit to converge in a minimum.

To get optimum results, an appropriate temperature profile has to be found for the fit. In this work, the temperature was held constant for the first 1000 iterations and then reduced by one percent per iteration. The total number of iterations done for each fit was 10000 times the number of free parameters. Figure 4.22 illustrates the temperature profile.

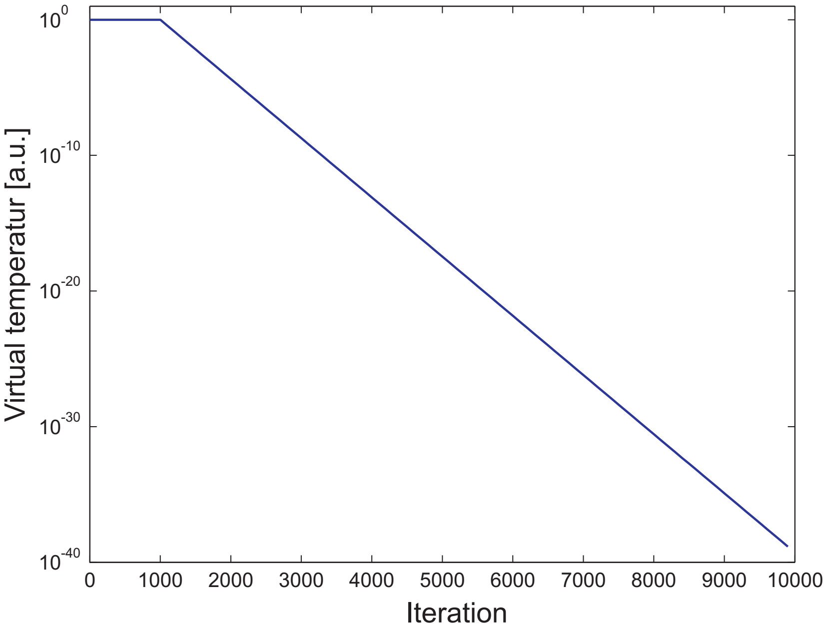

Figure 4.22: Temperature profile of the simulated annealing algorithm. The temperature is kept constant for the first 1000 iterations and then decreased by 1 % per iteration.

The reflectivity curve was calculated from the parameter set with the master formalism described in chapter 3.5.1. Due to the many orders of magnitude spanned by a reflectivity measurement it is useful to measure the quality of the fit logarithmically [95]

$$\chi^2 = \frac{1}{N}\sum_{i=1}^{N}\left(\ln \alpha R_i^{calc} - \ln R_i^{exp}\right)^2 . \tag{4.14}$$

The scaling factor α is needed due to the fact that the absolute intensity of the edge of total reflection could not be determined in a reproducible manner in our experiments (see above). An important advantage of the logarithmic method is that the scaling factor α can be determined analytically by minimizing χ^2 with respect to α. Equation 4.14 can be rewritten as

$$\chi^2 = \frac{1}{N}\sum_{i=1}^{N}\left(\ln\left(\frac{R_i^{calc}}{R_i^{exp}}\right) + \ln\alpha\right)^2 \tag{4.15}$$

$$= \frac{1}{N}\sum_{i=1}^{N}\left(\ln\left(2\frac{R_i^{calc}}{R_i^{exp}}\right) + 2\ln\left(\frac{R_i^{calc}}{R_i^{exp}}\right)\ln\alpha + \ln 2\alpha\right) . \tag{4.16}$$

Minimizing with respect to $\ln \alpha$

$$\frac{\mathrm{d}(\chi^2)}{\mathrm{d}(\ln \alpha)} = 0 \Longrightarrow \frac{-1}{N} \sum_{i=1}^{N} \ln \left(\frac{R_i^{calc}}{R_i^{exp}} \right) = \ln \alpha, \tag{4.17}$$

yields the scaling factor

$$\alpha = \exp \left(\frac{-1}{N} \sum_{i=1}^{N} \left(\ln R_i^{calc} - \ln R_i^{exp} \right) \right). \tag{4.18}$$

A well adjusted simulated annealing algorithm should find the global minimum independently from the starting position of the fit and the limits of the parameter space. However, in the implementation used in this work, this could not always be achieved. For this reason, the same data set was fitted several times with different starting parameters.

Another advantage of the simulated annealing algorithm is that it can be used to fit functions that can not be differentiated (like the Parratt formalism). Deterministic algorithms employ the derivative to find the direction of fastest improvement in parameter space, while the simulated annealing algorithm performs a random walk.

Genetic algorithm

This algorithm is very simple, but created surprisingly good results. Similar the simulated annealing algorithm, it mimics a principle from natural science. In one iteration, a large number of random individuals (fit models) are created. The algorithm tests the quality of each fit. In analogy to evolution, the best fitting models are then used to create the next generation.

In the implementation used in this work, the first generation of individual models is randomly generated from the whole allowed parameter space. For each parameter, a rectangular distribution is used from the low to the high limit. The value of each parameter is then determined randomly. Depending on the complexity of the model between 10^5 and 10^6 parameter sets were created in this way. From each model a reflectivity curve was calculated with the Parratt method for arbitrary electron density profiles described in chapter 3.5.2. The quality of the fit was then determined with the same approach as for the simulated annealing algorithm (see above).

For the second and later generations of parameter sets, only parameter values from the twenty best models of the previous generation were used. The number of parameter sets created in each generation is reduced by a factor of ten. For each set, each parameter is determined by taking randomly the value from one of the twenty best models of the last generation. The quality of the fits is calculated and the twenty best models determined.

The algorithm is stopped when the next generation would have less then twenty individuals and the parameter set with the lowest χ^2 value is taken as fit result.

The genetic algorithm has several advantages:

- Similar the simulated annealing algorithm, it is not necessary to know the derivative of the fit.
- Since the algorithm does not take a path through the parameter space, it can not be trapped by local minima.
- In the first generation the whole parameter space is probed, so that it does not depend on the starting position (in fact, there is no starting position).
- No additional parameters, such as a temperature profile, enter the algorithm. Thus, the algorithm can be readily applied by unexperienced users.

The main disadvantage is that only random spots of the parameter space are probed and the algorithm has no ”awareness” of the structure of the space surrounding a probed parameter set. A rather straightforward improvement is to combine the genetic algorithm with a deterministic algorithm, which finds the next local minimum to the probed position. However, for the data presented here, the simple algorithm proved to be sufficient.

Chapter 5

Results

Eleven samples have been investigated in the course of this Thesis (see table 4.1). Interface melting of ice could only be observed at the interface of ice with amorphous and crystalline SiO_2 substrates. The first three parts of this chapter will therefore be dedicated to these two types of samples. The remaining samples will be presented in the fourth section. The final section will show the results for the interface between ice and self assembled monolayers.

5.1 Silica substrates

The sample consists of a high purity silica glass substrate fused to an ice single crystal. The ice single crystal is aligned with its c-axis perpendicular to the interface. The properties of the sample can be found in table 4.1, sample number six. The sample was measured in June 2005 with the peltier cooling chamber (see chapter 4.1.3). Figure 5.1 shows two photos of the experimental setup.

Due to the high quality of the substrate surface, reflectivities could be measured up to almost 1 $Å^{-1}$. No broadening of the specular reflection could be observed (see Fig. 5.2), indicating the absence of correlated surface roughness (see chapter 3.4).

Reflectivity measurements have been performed from –20 °C to –0.1 °C. The temperature profile applied during the experiment is shown in Fig. 5.3. The temperature was increased and decreased in cycles in order to check the reversibility of the obtained results. A summary of the experiment is found in table 5.1.

Figure 5.4 shows the reflectivity curves obtained. The highest curve shows the reflectivity for -0.1 °C. Lower temperatures are divided by 100 per curve for clarity. The colors of the curves represent the temperature, low temperatures being blue and high temperatures being red. The experimental data are shown as circles while the solid lines indicate the fits. Due to experimental problems the low angle

Figure 5.1: Photos of the experimental setup during the beamtime June 2005. The peltier cooling chamber is mounted on the diffractometer. Top: Setup during the measurements. Bottom: Setup during sample change. The sample is wrapped in aluminum foil to prevent ice sublimation. It is clamped between the copper plates in the center of the chamber.

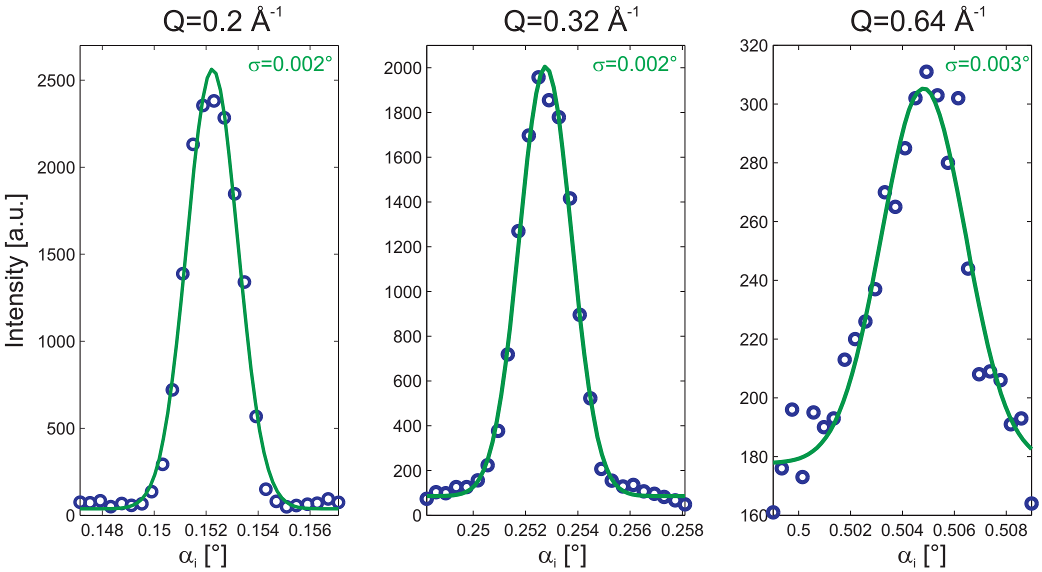

Figure 5.2: Rocking scans of the ice-silicon interface. The green lines show Gaussian fits to the data. The broadening of the specular reflection is negligible.

Number	**Temperature**	**Irradiation time**
1	-20 °C	4 hours
2	-4 °C	13 hours
3	-2 °C	18 hours
4	-1 °C	24 hours
5	-0.5 °C	29 hours
6	-0.5 °C	0 (new spot)
7	-0.3 °C	36 hours
8	-1 °C	40 hours
9	-1 °C	55 hours
10	-0.1 °C	60 hours
11	-2 °C	72 hours
12	-9 °C	77 hours
13	-2 °C	81 hours
14	-0.2 °C	82 hours
15	-1.5 °C	92 hours

Table 5.1: Summary of the reflectivity measurements on the ice-silica interface.

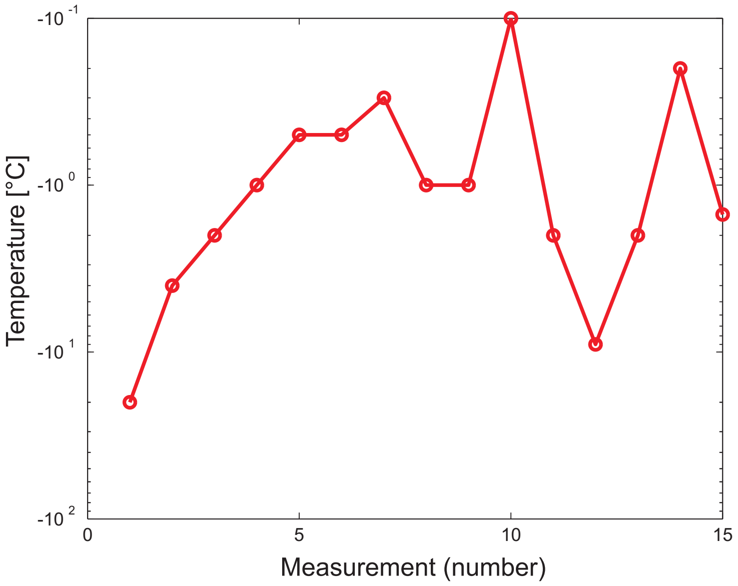

Figure 5.3: Temperature profile for the measurements of at the ice-silica interface.

part of the reflectivities taken at -20 °C and -4 °C could not be obtained. However, the quality of the experimental data remains low in the small angle range. The shape and the height of the edge of total reflection do not agree with the theoretical values (see the fits). This is due to the sensitivity of the measurements against small imperfections of the substrate surface at shallow angles.

Increasing the temperature of the sample leads to the appearance of oscillations on the reflectivity curve. This is a clear indication that at least one layer has formed that has an electron density different from both the substrate and bulk ice. Since the temperature agrees with the behavior predicted for premelting it is assumed that this is a disordered quasi-liquid layer. Note that the absence of oscillations does not mean that premelting is absent. A quasi-liquid layer with an electron density equal to bulk ice would not lead to the appearance of oscillations in the reflectivity curve and therefore is undetectable by this technique.

Reflectivity curves taken at low temperatures show no, or only broad oscillations, indicating the presence of only a very small to negligible quasi-liquid layer. As the temperature increases this oscillation increase in frequency, indicating the growth of the thickness of the disordered region. While this trend follows the temperature increase, some curves indicate the influence of another parameter. For example, the curve taken at –0.2 °C clearly shows a thicker quasi-liquid layer than the reflectivity measured at –0.1 °C, despite the lower temperature.

Figure 5.5 shows the same data as Fig. 5.4, but the color indicates the irradia-

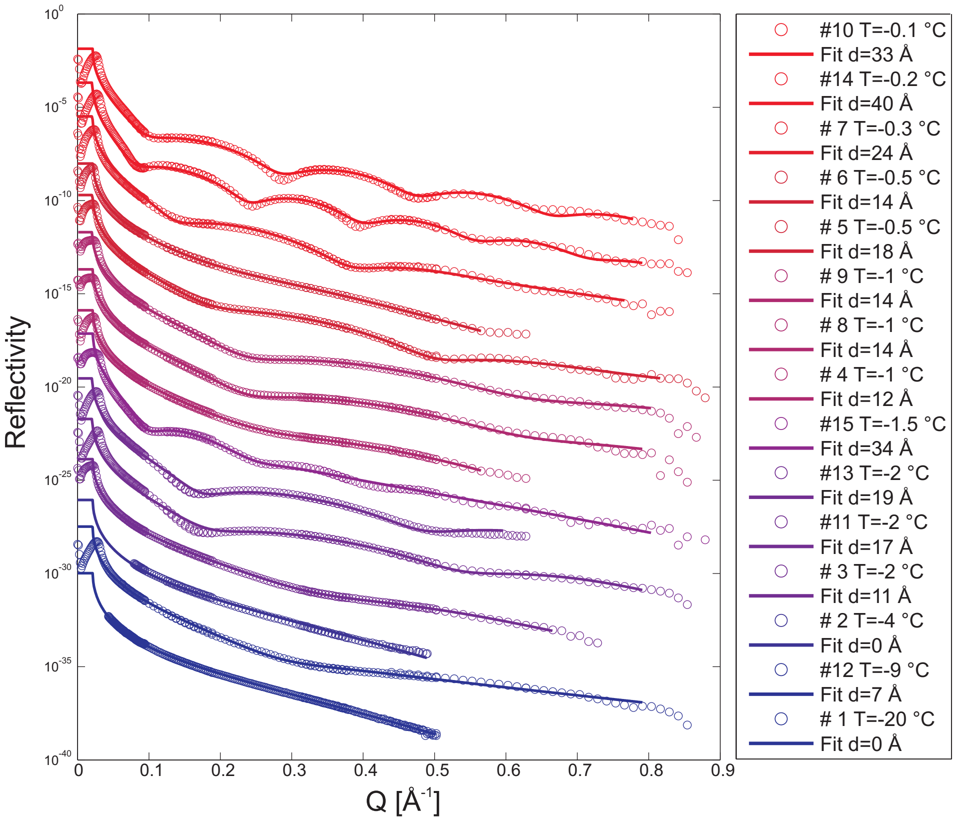

Figure 5.4: Reflectivities obtained at the ice-silica interface. The curves are displaced by a factor of 100. Circles indicate experimental data, together with the best fits (lines). The color of the symbols indicates the temperature of the measurement. The numbers of the fits refer to table 5.1.

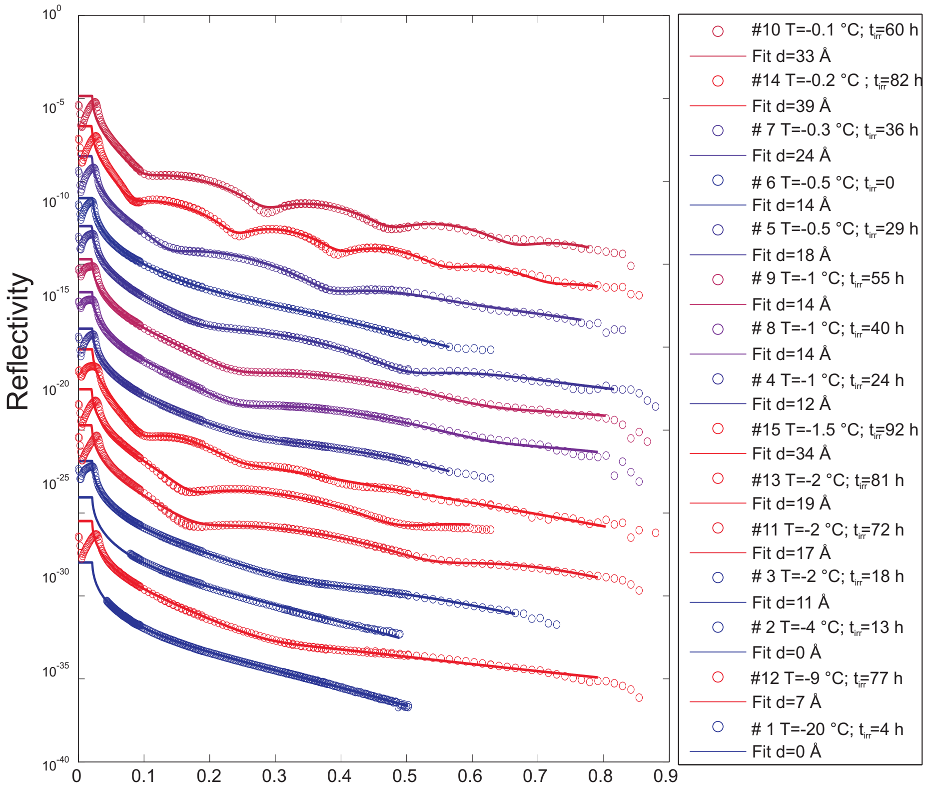

Figure 5.5: Reflectivity data from the ice-silica interface. The graph is similar to Fig. 5.4, but the color indicates the irradiation time of the sample, ranging from 0 (blue) to 92 hours (red).

Number	χ^2	**d**$_{QLL}$ **[Å]**	δ_{QLL}	$\rho_{e,QLL}$ **[Å^{-3}]**
1	0.0695	0	—	—
2	0.1989	0	—	—
3	0.0532	10.9	$5.0 \cdot 10^{-8}$	0.38
4	0.0351	12.4	$5.4 \cdot 10^{-8}$	0.41
5	0.1401	17.9	$5.2 \cdot 10^{-8}$	0.40
6	0.0383	14.3	$5.0 \cdot 10^{-8}$	0.38
7	0.1842	23.7	$5.5 \cdot 10^{-8}$	0.42
8	0.1739	13.7	$5.5 \cdot 10^{-8}$	0.42
9	0.0917	13.8	$5.4 \cdot 10^{-8}$	0.41
10	0.2681	33.1	$5.6 \cdot 10^{-8}$	0.43
11	0.3095	17.3	$5.6 \cdot 10^{-8}$	0.43
12	0.1723	7.3	$5.4 \cdot 10^{-8}$	0.41
13	0.2430	18.7	$5.6 \cdot 10^{-8}$	0.43
14	0.2194	39.3	$5.6 \cdot 10^{-8}$	0.43
15	0.2067	34.0	$5.6 \cdot 10^{-8}$	0.43

Table 5.2: Fitting results for the ice-silica interface.

tion time of the sample. Virgin sample surfaces are shown in blue. The curves turn more reddish with increasing irradiation. Since in most measurements irradiation time and temperature have increased simultaneously, it is difficult to attribute the growth of the quasi-liquid layer to each one of the parameters separately. However, for reflectivities taken at the same temperature one can clearly deduce an increase in the thickness of the premolten region with increasing radiation dose.

Figure 5.4 shows that the fits reproduce the measured data well. The numerical quality of the fit, measured as its χ^2-value (as defined by Eq. 4.14), is listed in table 5.2, together with the most important parameters of the fit. Figure 5.6 summarizes the parameters resulting from the fits. The index of refraction of the bulk ice was kept constant at its theoretical value ($\delta_{ice} = 4.31 \cdot 10^{-8}$) and is not included in the graphs.

The thickness of the quasi-liquid layer is a very robust fitting parameter, since it is directly related to the period of the oscillations on the reflectivity curve. This allows the determination of the thickness with an error of less than 10 pm. The index of refraction and the roughness of the layer and the substrate have higher uncertainties, owing to the high level of correlation between these parameters. Fixing the index of refraction of the bulk ice to the theoretical value and allowing only for small changes in the substrate refraction (± 5%), allows the determination of the index of refraction and electron density of the premolten region within 10% accuracy. For the measurements without premelting, the roughness can be determined very accurately, with a resolution of better than 10 pm. In the presence of the quasi-liquid layer, the strong correlation between the roughness at the ice/quasi-liquid and quasi-liquid/silica interface in the fitting render the accurate determination difficult. The value for the substrate roughness was left constant as long as possible, but for later measurements it seems to change. The accuracy of the determination of the roughness then drops to $\Delta\sigma =$ ±5 Å.

The thickness of the quasi-liquid layer will be discussed in more detail later. The index of refraction for the substrate and the quasi-liquid layer (if present) are remarkably constant. For the silica substrate the standard deviation is $1.58 \cdot 10^{-9}$ and the mean value $\bar{\delta}_{Silica} = 8.60 \cdot 10^{-8}$, differing less than 1% from the theoretical value of $8.68 \cdot 10^{-8}$. Ignoring the first two measurements without premelting, the standard deviation for the index of refraction of the quasi-liquid layer is $2.23 \cdot 10^{-9}$ and the mean value $\bar{\delta}_{qll} = 5.41 \cdot 10^{-8}$. This corresponds to an electron density of $\rho_{e,qll} = 0.413$ Å^{-3}, 23% higher than the electron density of water ($\rho_{e,water} = 0.335$ Å^{-3}) and 34% higher than the electron density of bulk ice ($\rho_{e,ice} = 0.308$ Å^{-3}). This result will be discussed later.

The results for both interface roughnesses are more scattered. The silica substrate has a mean roughness of $\bar{\sigma}_{silica} = 6.1$ Å, with a standard deviation of 2.6 Å. The scattering of the fit results seems to increase for later measurements. It is unclear if this is an artifact from fitting or a result of radiation damage. The roughness of the quasi-liquid layer, indicating the width of the transition between the disordered region and the bulk ice, is small. The mean value is $\bar{\sigma}_{qll} = 3.5$ Å and the standard deviation 1.7 Å. The boundary of the premolten region seems to be very well defined.

In order to reproduce the results the same sample was investigated in November 2005. The radiation damage done to the sample allows to locate the position of the measurement performed in June 2005. In order to find the previous position of the beam on the interface the instrument is set to a fixed point on the reflectivity curve. The sample is then horizontally scanned through the incident beam. The previous beam position can be identified by a change in the observed intensity. The contrast in this measurement depends on the particular shape of the reflectivity curve. Therefore, the scan was repeated at different momentum transfers Q. The best contrast was achieved for Q=0.26 Å^{-1} (see Fig. 5.7). The width of the beam mark is approximately 0.1 mm, four times larger than the horizontal beamsize (see chapter 4.2.2). This broadening is probably due to diffusion of the damage done to the ice.

In this experiment the temperature of the sample was immediately set to –0.25 °C, a temperature region where strong interface melting was expected from the previous experiment. The sample was continuously irradiated for six hours at constant temperature. Surprisingly, no interface melting could be observed this time. In order to reproduce the previous experiment as accurately as possible a

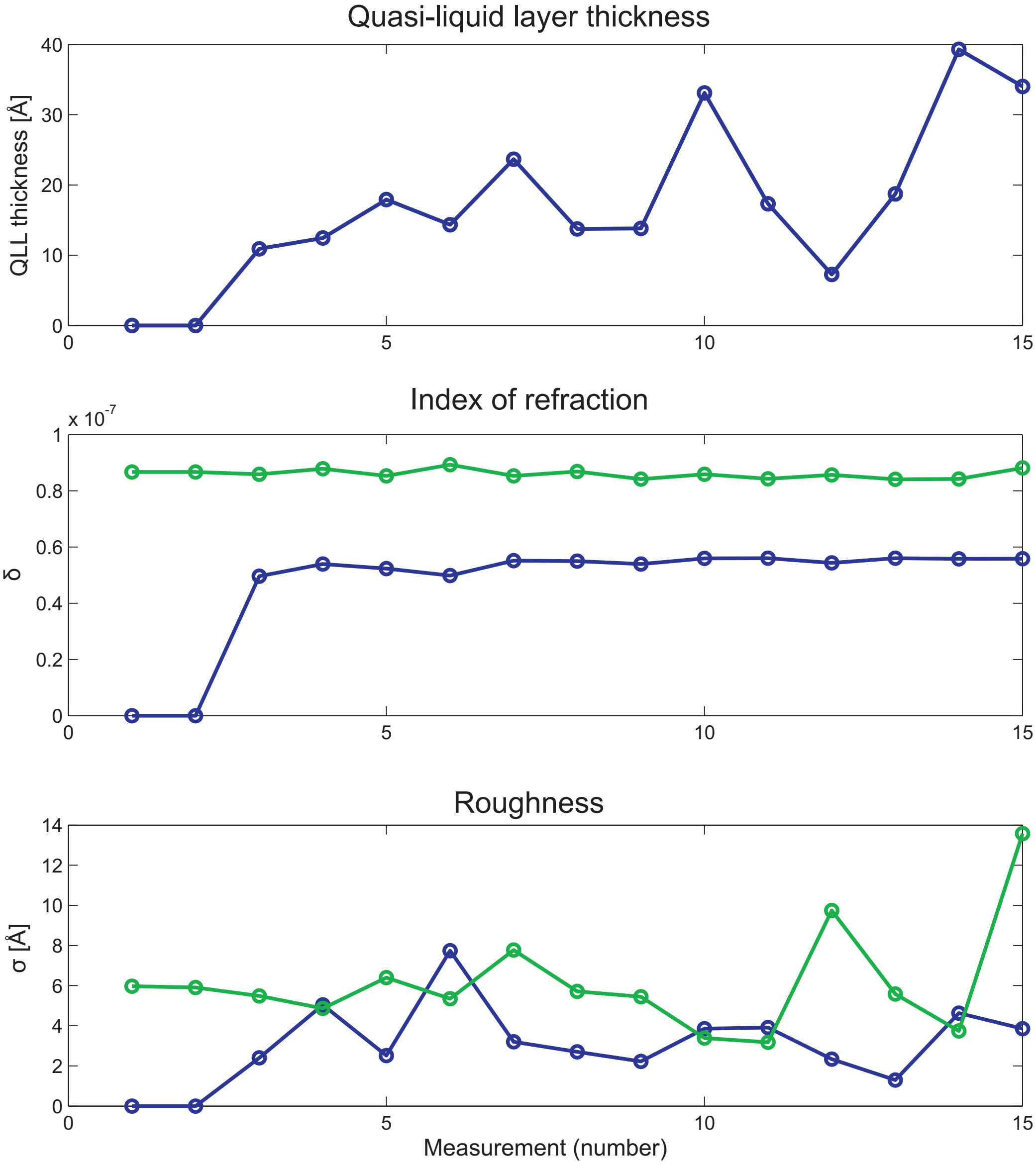

Figure 5.6: Summary of the fitting parameters for all measurements at the ice-silica interface. The parameters for the quasi-liquid layer are shown in blue. The parameters for the substrate are indicated in green.

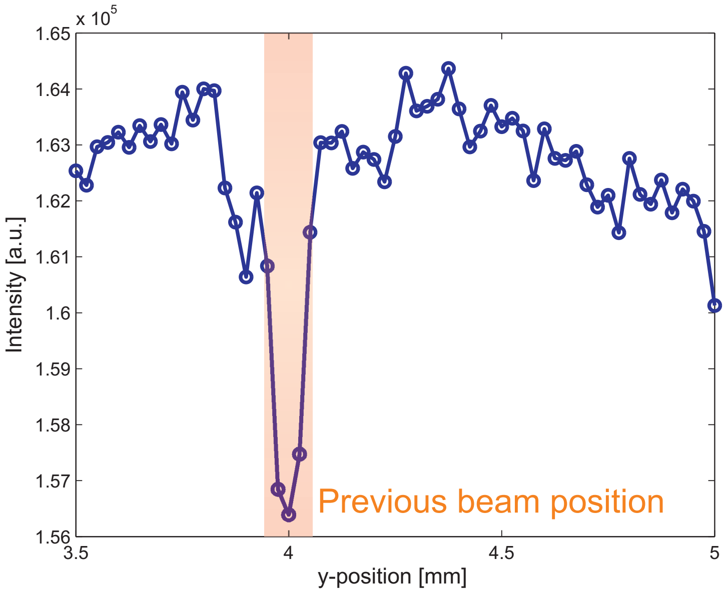

Figure 5.7: Radiation damage at the ice-silica interface caused by the experiment performed in June 2005. The instrument is set to fixed momentum transfer $Q = 0.26$ Å^{-1} while scanning the horizontal position of the sample.

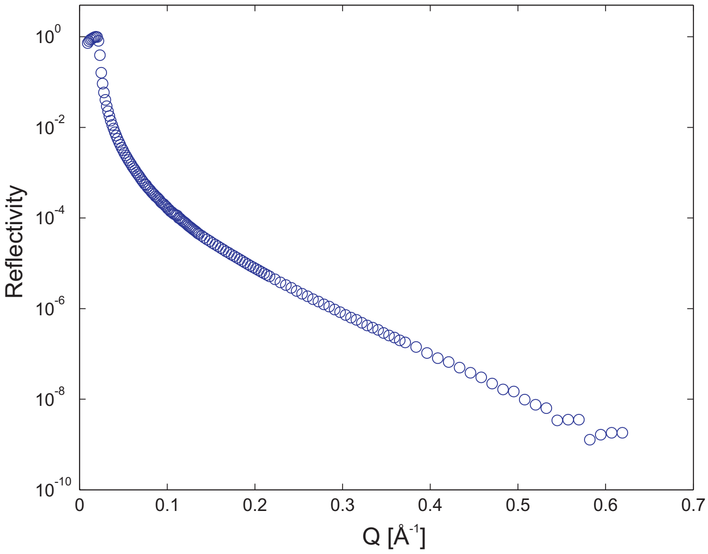

Figure 5.8: Reflectivity curve taken at –0.5 °C in November 2005 after irradiating the sample for more than 30 hours.

temperature cycle was then applied, cooling the sample to –20 °C, and heating it up to –0.5 °C again. Figure 5.8 shows a reflectivity curve taken after 31 hours of irradiation. Clearly, there is no indication of a premolten layer visible.

A second silica sample (sample 7 in table 4.1) was measured in the same beamtime. The substrate was bought from the same supplier and the surface is of similar quality. The preparation of both samples was identical. The sample was irradiated for 48 hours in a temperature range where a thick quasi-liquid layer is expected, but no interface melting could be observed.

The result of this second beamtime questions the reproducibility of the interface melting experiments. It shows that the premelting is governed by additional parameters that are not understood and seem to be sample and time-dependent, since all the experimental parameters were the same in the two experiments. The consequences of this result will be discussed in detail in the next chapter. The following section will show the results for the ice-quartz interface demonstrating a similar behavior.

5.2 Quartz substrates

Three ice-quartz interfaces were investigated in this work (numbers 4, 5 and 8 in table 4.1, respectively). All interfaces were prepared with the basal plane quartz surfaces in contact with the ice basal plane.

Sample 4 was measured in November 2004. It turned out that the 1 mm thick quartz substrate was not stiff enough for the experiment. The ice single crystal bent the quartz substrate during freezing. Since it was not possible to define the incident and exit angles with sufficient accuracy, the reflectivity could not be measured in a reproducible manner.

For this reason the experiment was reproduced with a quartz plate of double thickness in February 2005 (sample 5). However, even the thickness of 2 mm was not enough to prevent bending of the substrate completely. Data collection at high angles was difficult and impossible at small angles. The resulting reflectivity curves are shown in Fig. 5.9. The curves are offset by a factor of 100. None of the curves indicates the presence of an additional (quasi-liquid) layer. The bending of the substrate decreased with increasing temperature. For this reason the reflectivity curves change slightly in slope. The data quality in the small angle region increases with temperature, indicated by a smoothing of the region close to the critical angle (Q$\approx$0.05 Å^{-1}).

Since the bending of the substrate induces a defocusing of the beam, its effect can directly be seen in the width of the specular reflection. Figure 5.10 shows the width of the specular reflection for different momentum transfers for a measurement at $T = -20$ °C. For a high quality surface with negligible bending the

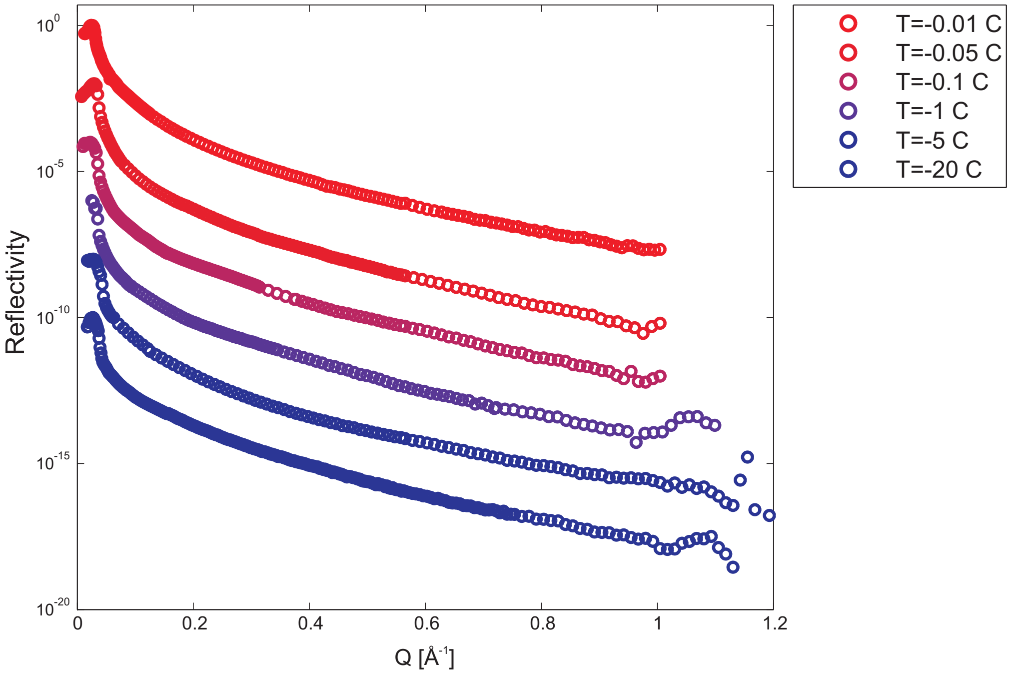

Figure 5.9: Results of the beamtime in February 2005.

width of the specular reflection is less than $5 \cdot 10^{-3}$ °. At small angles, where the effects of surface imperfections are most pronounced, the average width exceeds values of $15 \cdot 10^{-3}$ °, three times higher than for the perfect surface. In addition, small changes in momentum transfer lead to strong and unpredictable changes in the width. For a momentum transfers larger than 0.06 Å^{-1}, the width starts to decrease monotonously. The measured width of rocking scans performed at high temperature (–0.01 °C) and large momentum transfer is shown for comparison. The width is significantly smaller, but still larger than for a perfect surface. There is only a small and monotonous increase of the width with increasing momentum transfer, indicating that the surface has relaxed at this temperature.

The third ice-quartz interface (sample 8) has been investigated during the beamtime in June 2005. In order to prevent substrate bending a large single crystal with a thickness of 12.7 mm was used. Figure 5.11 shows the widths of the specular reflection for different momentum transfers. The width is constant over the full momentum transfer range and close to $3 \cdot 10^{-3}$ °. The data set was taken at –5 °C, but similar results were obtained for all temperatures. Therefore, it can be concluded that the surface is not bent. Furthermore, the absence of diffuse scattering shows that the remaining surface roughness is fully uncorrelated.

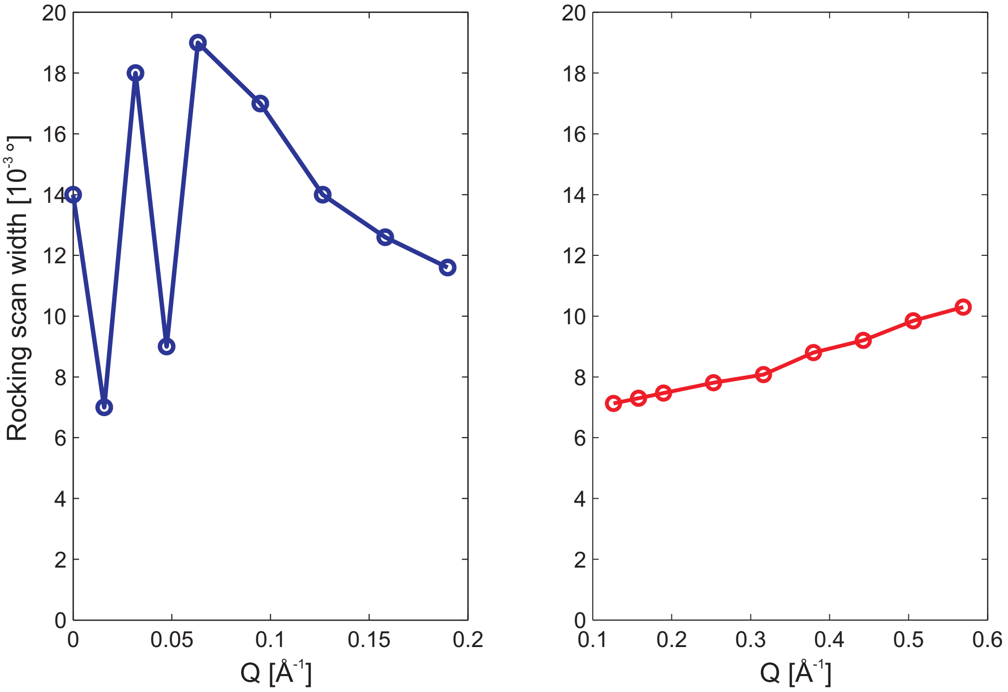

Figure 5.10: Width of the specular reflection at the ice-quartz interface for different momentum transfers (Left: Small angle part. Right: High angle part). The scans have been perfomed at $T = -20$ °C.

During the beamtime severe problems occurred with the temperature control system. The problems could be solved, but the first measurement under stable conditions could only be performed after 59 hours of irradiation. For this reason the irradiation times of the quartz sample are much higher than for the silica sample (see table 5.3). The dataset 4, which has an irradiation time of 0, has been measured at a different sample spot. Figure 5.12 shows the temperature profile used during this beamtime.

The reflectivities obtained are shown in Fig. 5.13. The color of the curve indicates the temperature at which the measurement has been performed. The curves are offset by a factor of 100 to avoid overlapping. The effect of irradiation time is displayed in Fig. 5.14. The results are similar to those obtained for the silica sample. There is a clear signal of a layer at the interface. The thickness of this layer depends on temperature and irradiation time.

The values of the fits to the data are shown in table 5.4. The quality of the fits and the accuracy of their parameters are similar to the values obtained for the silica data. The values of all the fitting parameters can be seen in Fig. 5.15.

Quartz has a higher density than silica, resulting in a higher index of refrac-

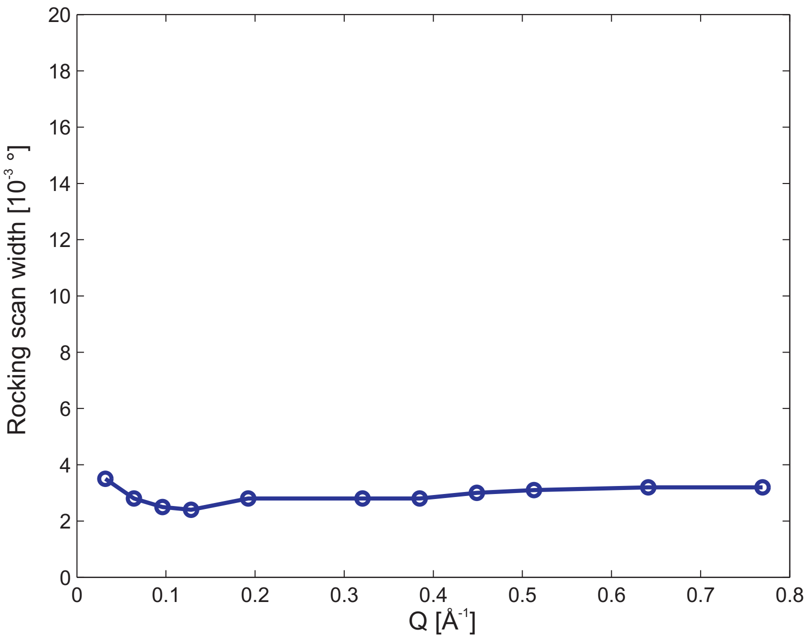

Figure 5.11: Specular reflection width of the quartz substrate measured in June 2005.

Number	Temperature	Irradiation time
1	-5 °C	59 hours
2	-1 °C	66 hours
3	-2 °C	78 hours
4	-2 °C	0 (new spot)
5	-0.2 °C	90 hours
6	-0.1 °C	97 hours
7	-8 °C	102 hours
8	-5 °C	107 hours
9	-12 °C	117 hours
10	-20 °C	120 hours
11	-1 °C	137 hours
12	-0.5 °C	142 hours
13	-0.2 °C	150 hours

Table 5.3: Reflectivity measurements at the third ice-quartz interface.

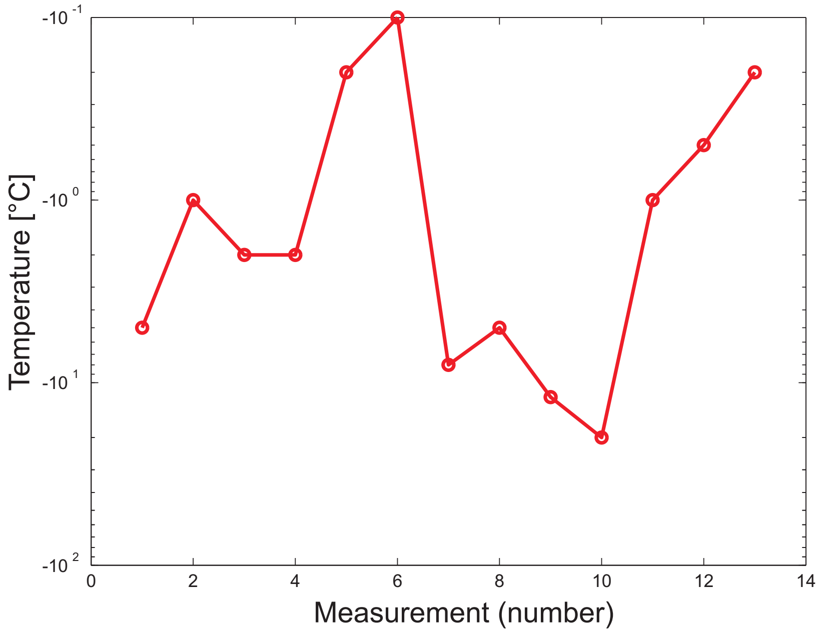

Figure 5.12: Temperature profile of the measurements performed at the ice-quartz in June 2005.

Number	χ^2	$\mathbf{d}_{QLL}$ **[Å]**	δ_{QLL}	$\rho_{e,QLL}$ **[Å^{-3}]**
1	0.1302	0	—	—
2	0.1313	18.4	$5.6 \cdot 10^{-8}$	0.43
3	0.0670	15.0	$5.6 \cdot 10^{-8}$	0.43
4	0.1042	0	—	—
5	0.0527	34.1	$5.6 \cdot 10^{-8}$	0.43
6	0.3254	46.2	$5.6 \cdot 10^{-8}$	0.43
7	0.2815	10.1	$5.3 \cdot 10^{-8}$	0.41
8	0.3352	21.4	$5.6 \cdot 10^{-8}$	0.43
9	0.2400	14.8	$5.6 \cdot 10^{-8}$	0.43
10	0.0398	10.4	$5.2 \cdot 10^{-8}$	0.40
11	0.2317	29.9	$5.6 \cdot 10^{-8}$	0.43
12	0.2660	37.6	$5.6 \cdot 10^{-8}$	0.43
13	0.3025	50.1	$5.6 \cdot 10^{-8}$	0.43

Table 5.4: Fitting results for the ice-quartz interface.

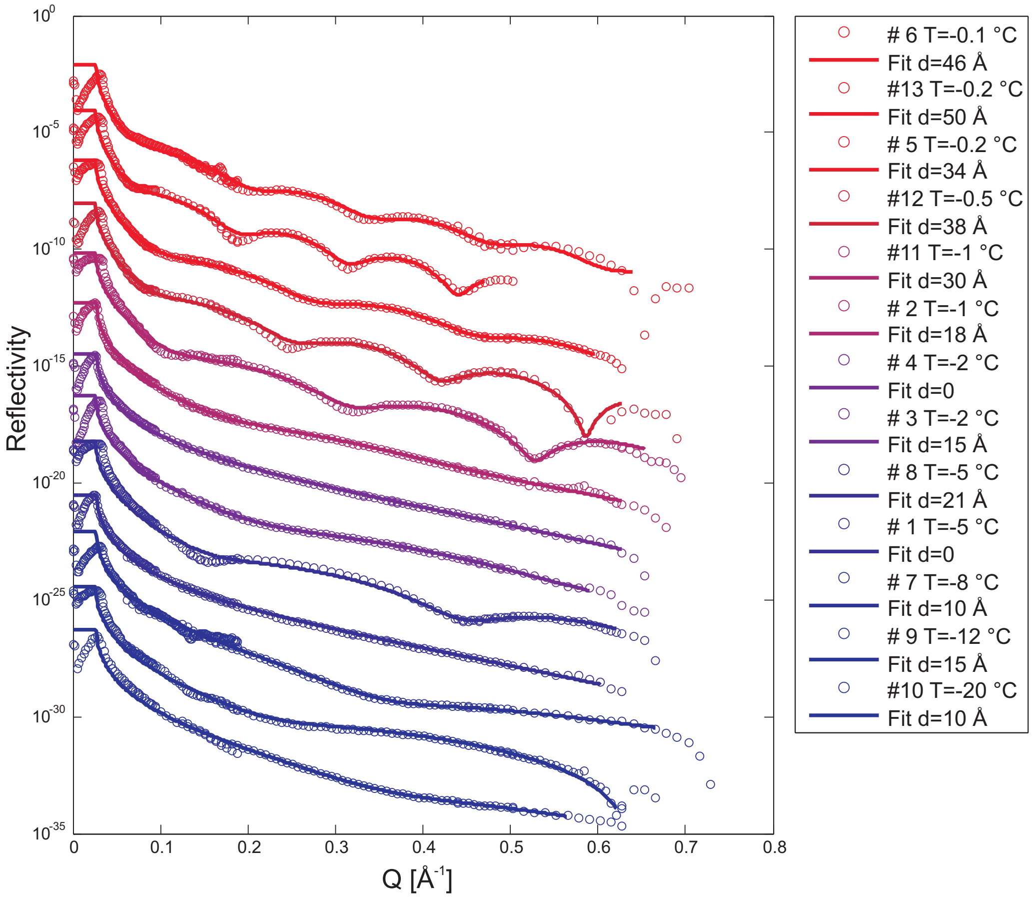

Figure 5.13: Temperature-dependent reflectivity curves measured at the third ice-quartz interface. The curves are displaced by a factor of 100. The circles indicate experimental data together with the best fits (lines). The color of the symbols indicates the temperature of the measurement.

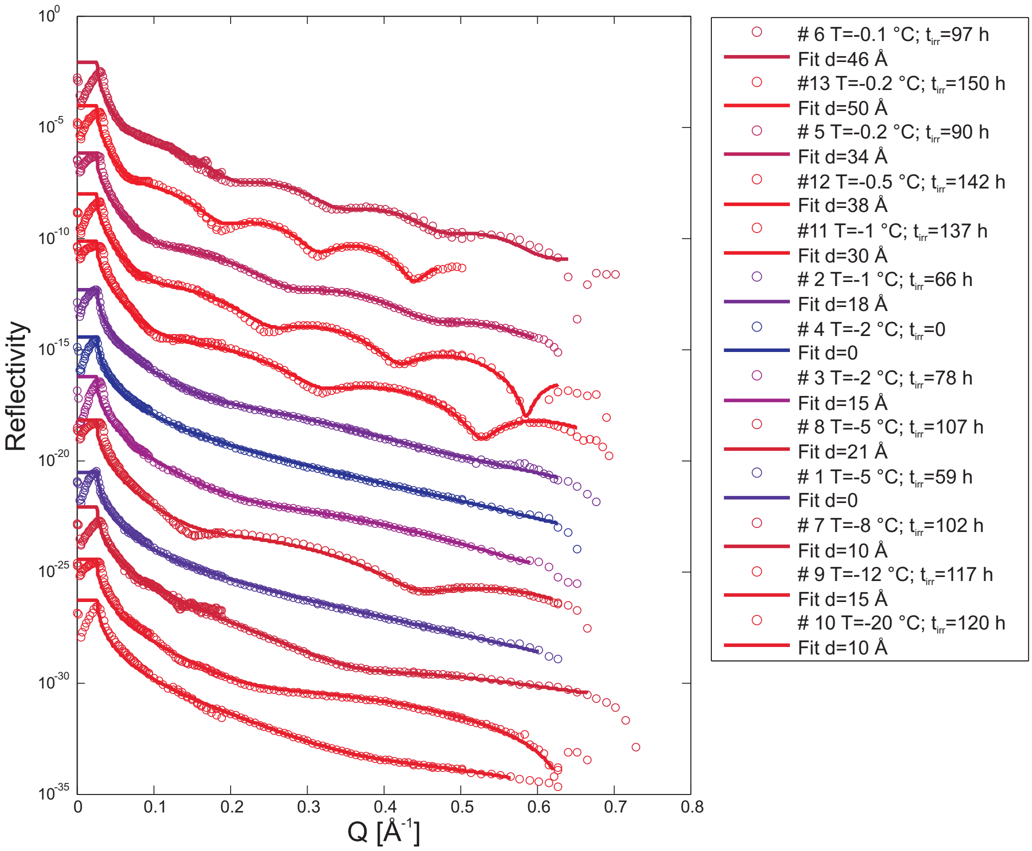

Figure 5.14: Temperature-dependent reflectivity curves measured at the third ice-quartz interface. The color indicates the irradiation time of the sample, ranging from 0 (blue) to 150 hours (red).

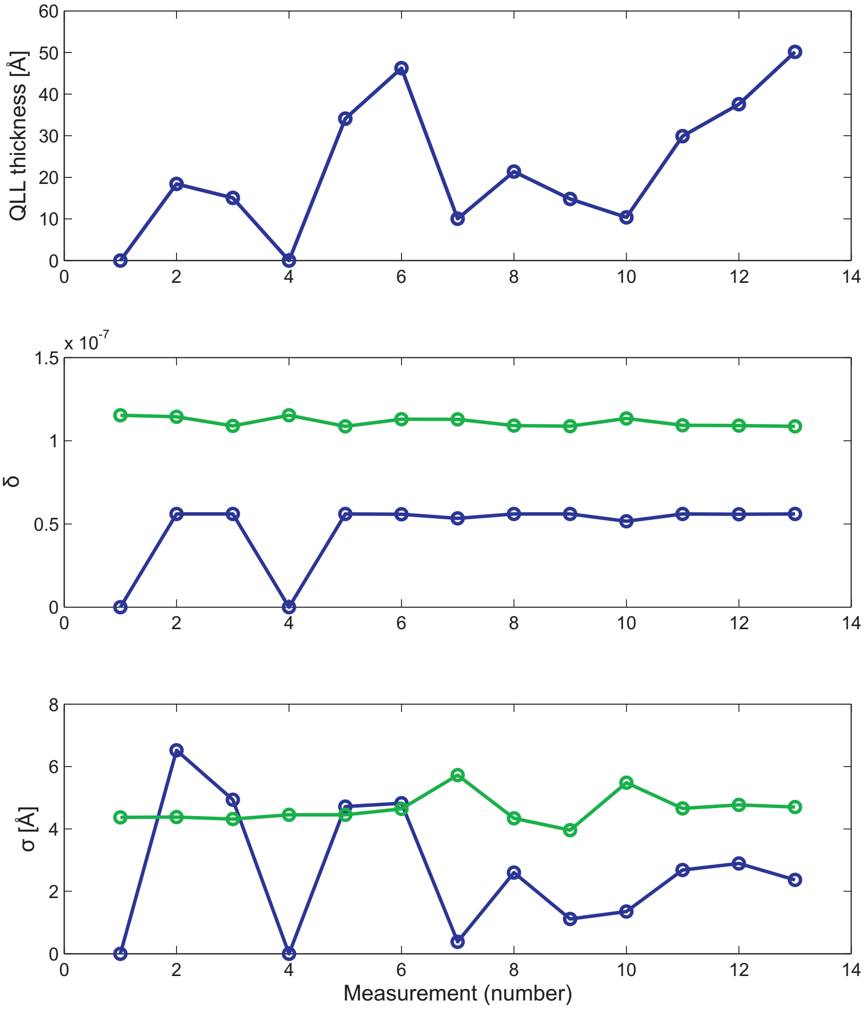

Figure 5.15: Fitting parameters for all the measurements taken. The parameters for the quasi-liquid layer are shown in blue. The parameters for the substrate are indicated in green. Note that no premelting was observed for the measurements 1 and 4, therefore d_{QLL}, δ_{QLL} and σ_{QLL} are zero.

tion of $\delta_{quartz} = 1.05 \cdot 10^{-7}$ (electron density $\rho_{e,quartz} = 0.80$ Å^{-3}). The index of refraction resulting from the fits is slightly (6%) higher than this value. The average index of refraction is $\bar{\delta}_{quartz} = 1.11 \cdot 10^{-7}$, with a standard deviation of $2.8 \cdot 10^{-9}$. Reflectivity measurements only allow a determination of the electron density difference between the two bulk materials. Since the absolute value can not be probed it is not possible to tell if this enhanced density is due to a denser substrate or to a reduction of the density of the bulk ice. The second option seems physically more reasonable and could be an artifact of radiation damage or sample preparation. The index of refraction of the premolten region is very robust and with an average value of $\bar{\delta}_{qll} = 5.53 \cdot 10^{-8}$ and a standard deviation of $1.47 \cdot 10^{-9}$. This corresponds to an electron density of $\rho_{e,qll}$ =0.422 Å^{-3}, 26% larger than the electron density of water and 37% larger than the electron density of ice. It agrees very well (within 2%) with the result obtained for the electron density of the quasi-liquid layer at the ice-silica interface. Chapter 6.2 will discuss these results in more detail.

The average value of the substrate roughness is $\bar{\sigma}_{quartz} = 4.6$ Åwith a standard deviation of 0.5 Å. For the quasi-liquid layer an average roughness of $\bar{\sigma}_{qll} = 3.1$ Å is obtained, again with pronounced scattering in the data. The standard deviation is 1.9 Å. For the silica sample an average roughness of 3.5 Å was obtained for the quasi-liquid layer. The consistency of these values is important because the roughness of the substrates is different in both experiments. This strongly suggests that the roughness obtained for the premolten region is indeed a measure of the quasi-liquid-ice boundary region.

5.3 Other samples

This section covers the remaining samples, with the exception of the ice interfaces with self-assembled monolayers. Their properties can be seen in table 4.1. The substrate for sample 1 was float glass which is frequently used for laboratory equipment. Unlike fused silica it contains many impurities. The substrate for sample 2 was a sapphire single crystal. Sample 3 was prepared with a similar sapphire substrate, but covered by a 100 nm layer of silver grown by MBE. Sample 9 was prepared with a single crystalline magnesium oxide substrate.

5.3.1 Ice-float glass interface

The ice-float glass interface was the first interface investigated in the course of this work. The measurements were performed in August 2003. The width of the specular reflection was $5 \cdot 10^{-3\circ}$. It showed no sign of broadening with increasing momentum transfers. The measured reflectivities are shown in Fig. 5.16.

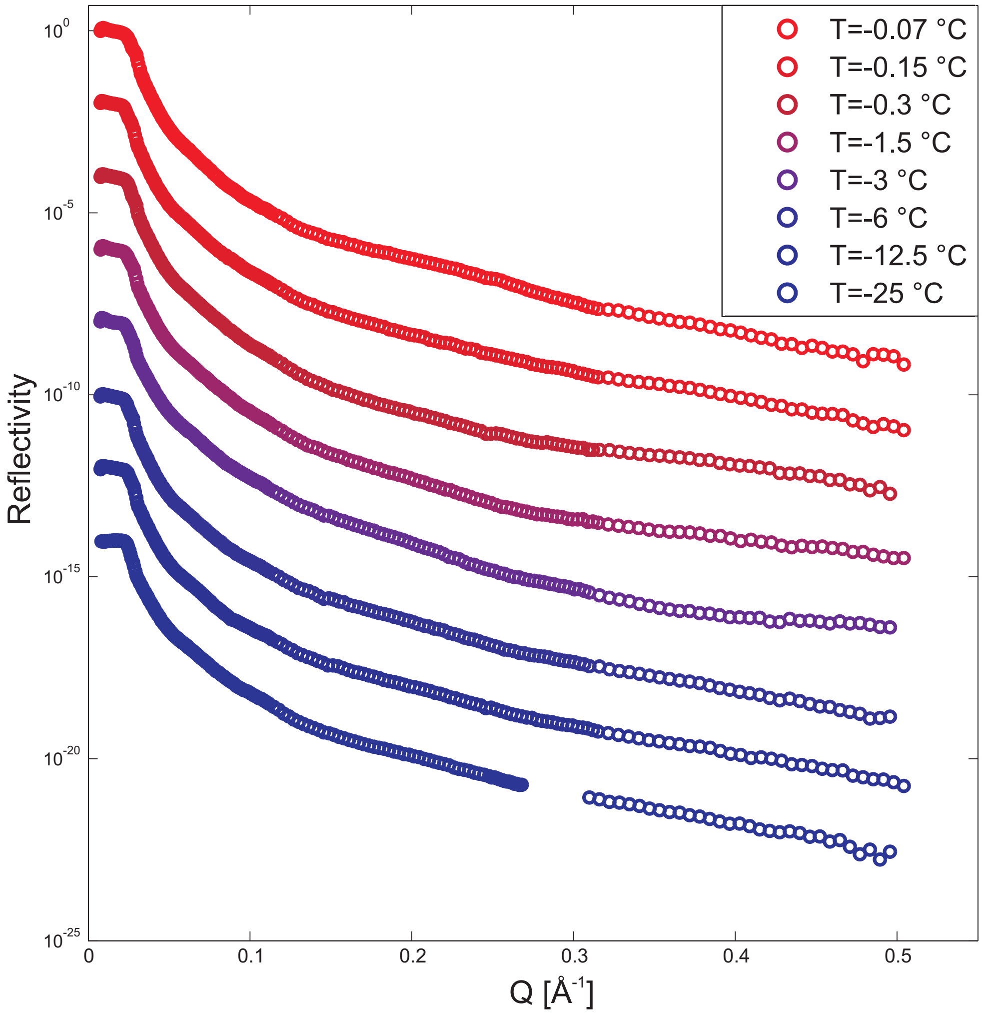

Figure 5.16: Temperature-dependent reflectivity of the ice-float glass interface . Low temperatures are shown on the bottom. Higher temperatures are displaced by a factor of 100.

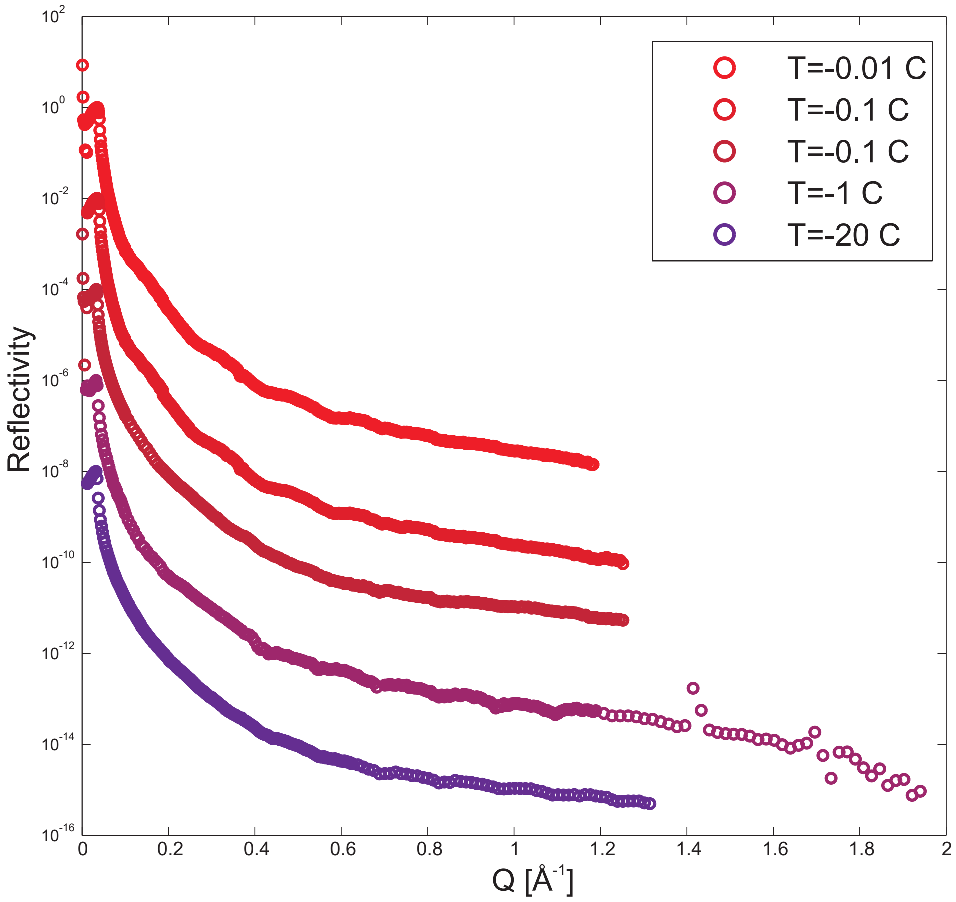

Figure 5.17: Temperature-dependent reflectivity of the ice-sapphire interface.

Small changes are visible on the reflectivity curve when changing the temperature. Unfortunately, these changes are neither reproducible, nor are they significant enough to produce stable fits. Models employing a glass substrate with a premolten layer were not able to reproduce the data with satisfying quality. In addition, it remains unclear if, and to which extent, the substrate releases impurities into the ice. For this reason these results can not be used to draw conclusions about the presence of a quasi-liquid layer at this interface.

5.3.2 Ice-sapphire interface

The measurements were performed during the beamtime in February 2004. Although the substrate was only 1 mm thick, the sample showed no bending. The roughness of the substrate was very low, allowing the measurement of the reflectivity curve up to $Q = 1.8$ Å^{-1}. The width of the specular reflection was constant over the whole range with a value of $3 \cdot 10^{-3\circ}$. The reflectivity curves are shown in Fig. 5.17.

At all temperatures a faint, high frequency oscillation is visible. Since this feature is not temperature-dependent, it can not be attributed to premelting. It is more likely that the oscillations are produced by a thick layer of contamination at the interface ($d = 40$ Å) produced during baking. Since no etching was applied to clean the substrate after baking, the contaminations might still have been present during sample bonding.

No consistent changes of the interface reflectivity could be observed by changing the temperature. The roughness and contrast of the layer of contaminations seems to change slightly, resulting in a faster overall decay of the reflectivity with increasing temperature. This is probably due to diffusion of the contaminations into the ice at higher temperatures. There is no indication of the appearance of a quasi-liquid layer with a change in the electron density. This could be either because the contaminations at the interface block premelting or because the signal of the contamination obscures oscillation coming from the quasi-liquid layer.

5.3.3 Ice-silver interface

The ice-silver interface was investigated in February 2004. The temperature-dependent reflectivity is shown in Fig. 5.18. The interference fringes from the silver layer are clearly visible. Since the electron density difference between ice ($\rho_{e,ice} = 0.3$ Å^{-3}) and silver ($\rho_{e,Ag} = 2.8$ Å^{-3}) is very high, these oscillations obscure any signals from a quasi-liquid layer of small thickness. Therefore, only high temperature measurements are shown in Fig. 5.18.

The highest measured temperature was –0.01 °Cwith a total irradiation time of 44 hours. However, no significant change can be seen in the reflectivity. No signal of premelting can be observed, but the presence of a quasi-liquid layer with a thickness of less then 20 Å can not be excluded. If the density change between the ice and the quasi-liquid layer is lower than 20%, an even thicker disordered region would be invisible. Similarly, contaminations at the interface could be obscured by the large density contrast between the silver and the ice.

For these reasons no conclusions can be drawn about the premelting at the ice-silver interface. The quality of the silver layer is very high, with a roughness of only 3.2±0.5 Å. The width of the specular reflection is less than $3 \cdot 10^{-3\circ}$ and constant up to 1 Å^{-1}. This shows that the high quality surface created in the MBE process is conserved through the bonding process.

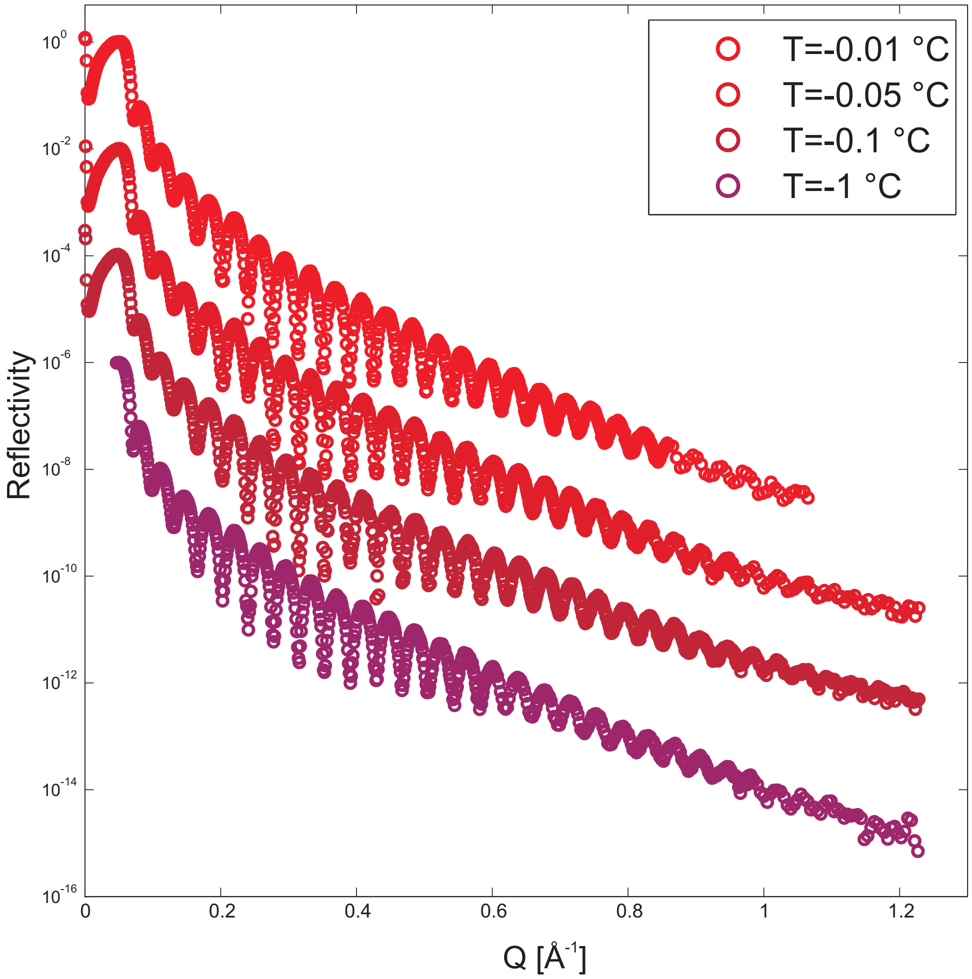

Figure 5.18: Temperature-dependent reflectivity of the silver-ice interface.

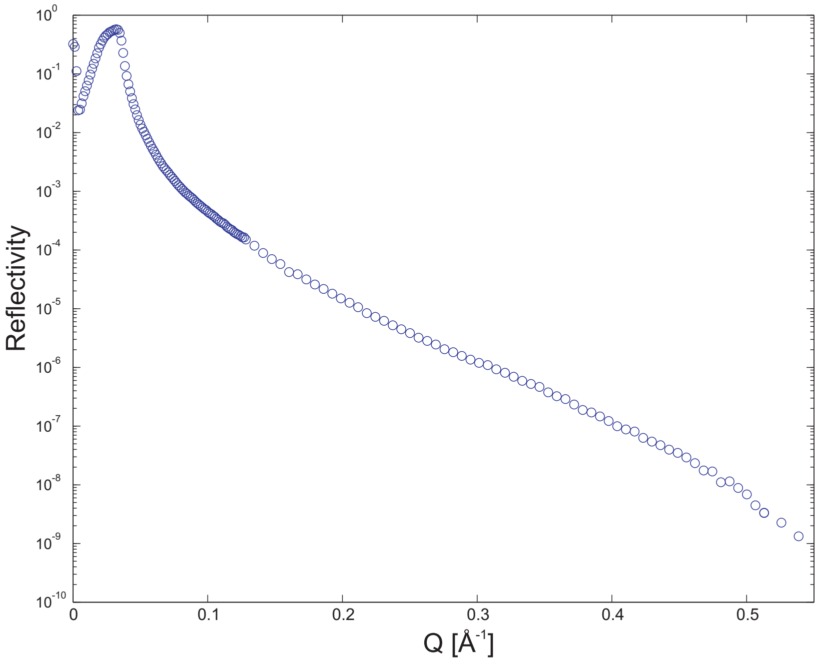

Figure 5.19: Reflectivity of the ice-MgO interface after 2 hours of irradiation at $T = -0.2$ °C.

5.3.4 Ice-MgO interface

The ice-MgO interface was investigated in June 2005. The 3 mm thick substrate did not show any signs of bending. The widths of the specular reflection were between $3 \cdot 10^{-3\circ}$ and $5 \cdot 10^{-3\circ}$. The substrate was heated to –0.2 °C and irradiated for 21 hours. No signs of premelting could be observed. Figure 5.19 shows the reflectivity after 21 hours of irradiation. No oscillations are visible, indicating the absence of a layer with a change in electron density at the interface.

Unlike the samples described before, this sample shows a flat reflectivity curve without any features that could hide a quasi-liquid layer. Therefore, it can be concluded that no premelting was happening at the interface during the measurement or that the quasi-liquid layer has a density identical to the density of bulk ice.

5.4 Self-assembled monolayers

The ice in contact with hydrophobic self-assembled monolayers has been investigated in July 2006. The sample preparation is described in chapter 4.1.1. Two interfaces with different SAMs grown on a silicon substrate covered by its native oxide layer have been measured. On one substrate octadecyl-trichlorsilane (OTS), a molecule with a pure hydrocarbon tail, was deposited. The second substrate was covered with fluoroalkylsilane (FAS), a flourinated hyrdocarbon. The substrate consists of silicon, covered by a silicon oxide layer to which the head group of the SAM is anchored. The molecules are depicted in Fig. 4.2.

Organic molecules are radiation sensitive. For this reason great care was taken to characterize radiation damage and keep the radiation dose on the sample as small as possible. The reflectivity curves were measured while translating the sample horizontally through the beam such that every point of the reflectivity curve was measured on a fresh, non-irradiated spot. The radiation effects are discussed in more detail below.

5.4.1 Octadecyl-trichlorsilane (OTS)

Due to the high quality silicon substrate, the width of the specular reflection is very small. In the experiment the value was constant at $1.2 \cdot 10^{-3\circ}$ up to $Q = 0.5$ Å^{-1}. This demonstrates the high quality of the substrate surface. The OTS layer did not introduce additional surface roughness.

Figure 5.20 shows the reflectivities from the OTS-ice interface for different temperatures. No big changes are observed when changing the temperature. The position of the minimum shifts slightly. The depth of the first minimum decreases with increasing temperature. These changes probably result from relaxation phenomena at the interface as the temperature of the sample is increased.

Since it was not possible to measure the reflectivity of the OTS layer without ice, its properties could not be determined independently. This leads to a large number of unknown parameters in the model of the ice-OTS interface when fitting the data. From the chemical structure a layer thickness of 5.5 Å is expected for the head group, and a thickness of 22 Å for the hydrocarbon tail. The position of the first minimum at $Q \approx$ 0.2 Å^{-1}, suggests a total thickness of the OTS layer of 31 Å. This value is confirmed by the fitting. The model used for the fits consists of two layers for the self-assembled monolayer, one for the head group and one for the hydrocarbon tail. The substrate is covered with an additional layer of silicon dioxide.

Since the electron density contrast between the silicon and its oxide layer is small, the oxide layer does not contribute to the distance obtained from the first minimum. This thickness is 13% higher than the expected total thickness of 27.5 Å. The index of refraction measured for the hydrocarbon tail is only $3.3 \cdot 10^{-8}$, 14% smaller than the expected value of $3.8 \cdot 10^{-8}$. This indicates a stretching of the layer, since the density drops by the same amount the thickness increases. The origin of the stretching is unclear.

Although the data are of high quality, the large number of unknown parameters does not allow to deduce details on the structure of the ice interface. The problem

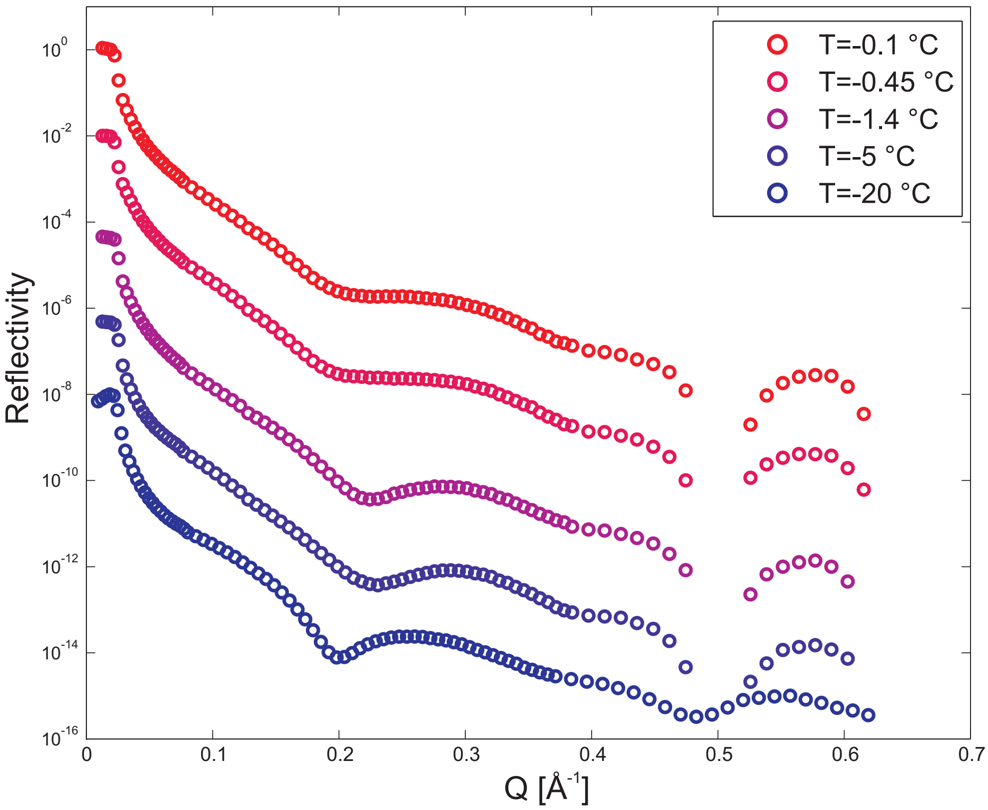

Figure 5.20: Temperature-dependent reflectivity of the ice-OTS interface. The sample has been translated horizontally during the measurement in order to avoid radiation damage. The reflectivity curve exhibits a deep minimum at $Q = 0.5$ Å^{-1}, where the measured reflectivity disappears in the background.

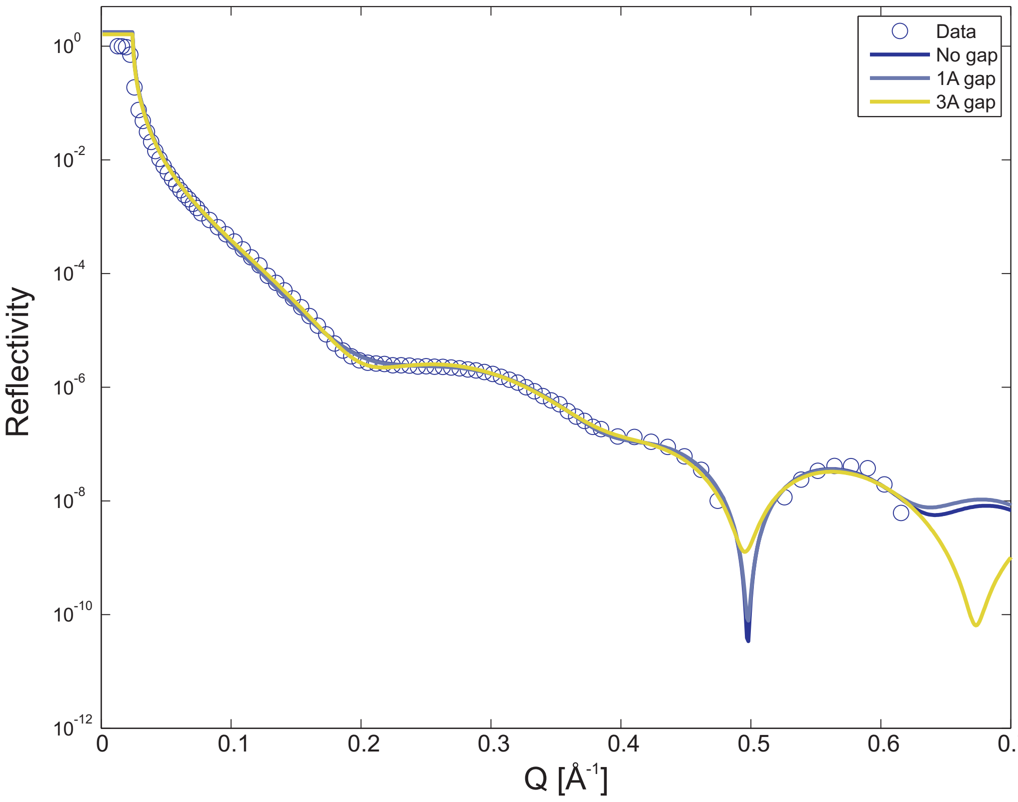

Figure 5.21: Fits to the reflectivity measured at –0.45 °C. The different fits with a fixed thickness for the quasi-liquid layer are shown. There is no significant difference in the quality of the fits.

is illustrated in Fig. 5.21. The data taken at –0.45 °C are shown as green circles. The solid lines show fits assuming quasi-liquid layers of varying thickness. In these fits, the thickness of quasi-liquid layer at the interface has been fixed, while the fitting program can adjust the other parameters of the sample within physically reasonable boundaries. There is no significant difference in the quality of the fits. Therefore it is not possible to confirm the presence of a quasi-liquid layer at the ice-OTS interface.

5.4.2 Fluoroalkylsilane (FAS)

The rocking scan widths confirm a similar high quality of the FAS-SAM as for the OTS sample. No surface correlations were found for this SAM.

The sample was heated to –0.4 °C. After measuring the reflectivity, it was cooled to almost –20 °C and measured again. A final measurement was performed

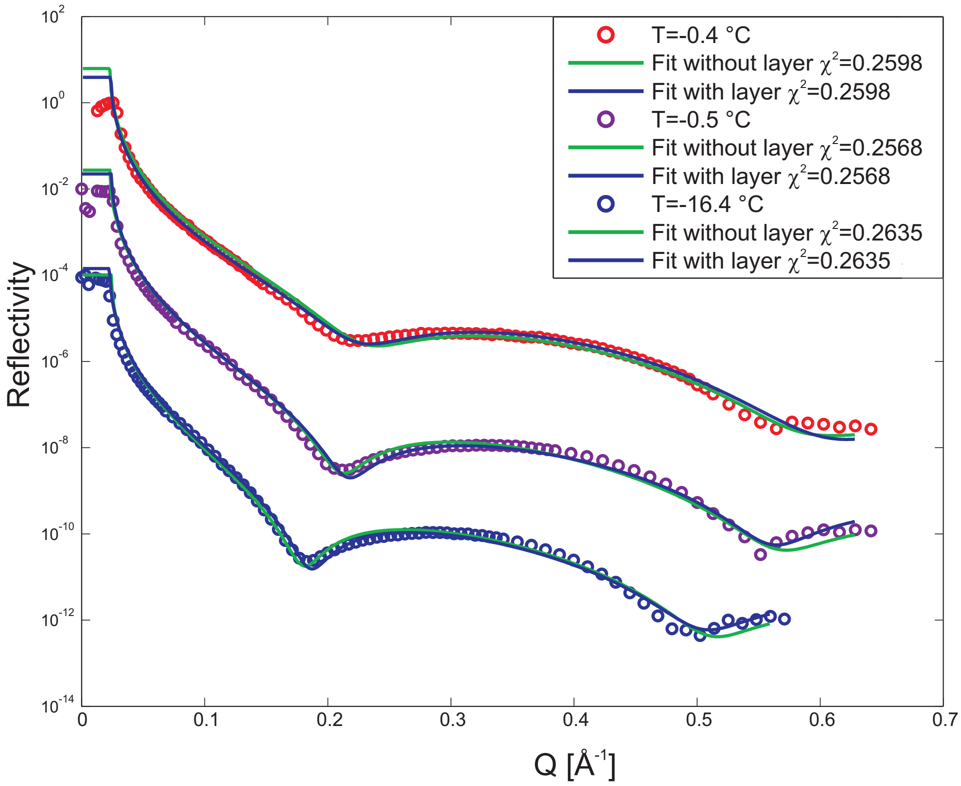

Figure 5.22: Temperature-dependent reflectivity of the ice-FAS interface.

at a high temperature of –0.5 °C. The observed reflectivities are shown in Fig. 5.22. The reflectivity shows a broad and strong oscillation from the fluorinated self-assembled monolayer. The solid lines show fits to the data.

For the electron density model of the fluoroalkylsilane three layers were used. The first layer represents the silane head group that is anchored to the substrate. Its thickness is left free within 4 to 6 Å. A thin second layer simulates the two CH_2 groups. The long fluorinated tail is modeled as a third layer with a thickness of approximately 11 Å.

In Fig. 5.22 two fits are shown for every reflectivity taken. One with a three-layer model containing only the self-assembled monolayer and no additional structure at the interface (green lines). The second fit assumes an additional layer at the interface. The improvement of the fits is not significant. The introduction of additional fitting parameters results only in a small improvement of the fit. The changes in the reflectivity can be reproduced by slightly altering the properties of the monolayer. This indicates that the temperature-dependent changes are due to

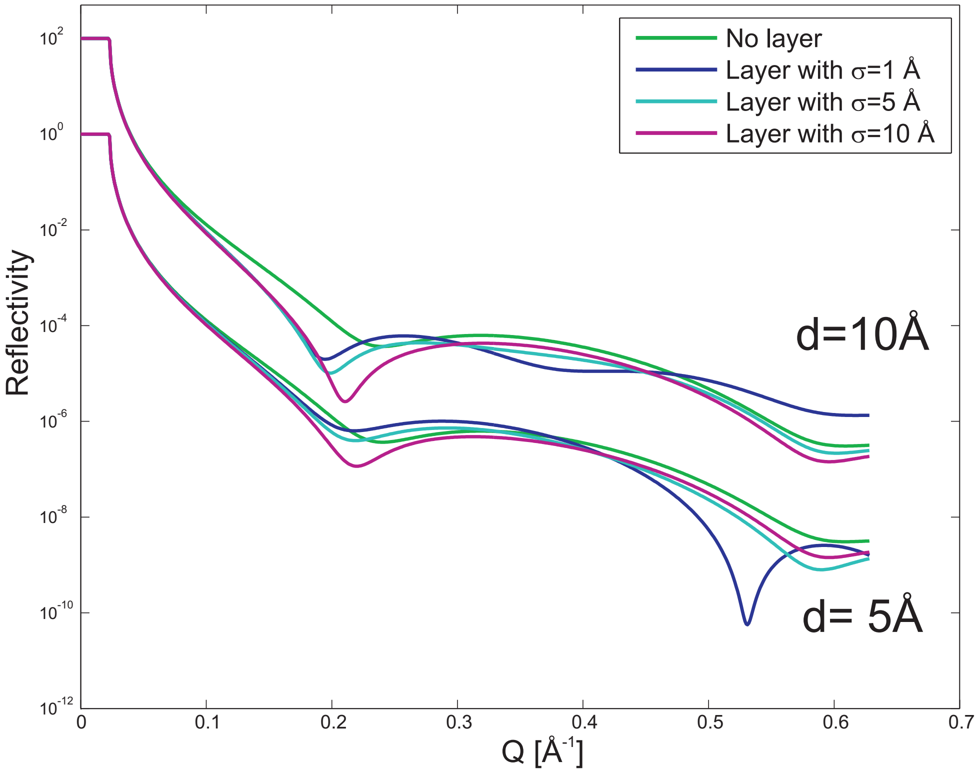

Figure 5.23: Combined effect of roughness and quasi-liquid layer thickness on the reflectivity obtained from the ice-FAS interface. The density of the quasi-liquid layer was set to $\rho_e = 1.2\rho_{e,H2O}$.

relaxation effects rather then to the appearance of additional structures.

Calculated reflectivity curves are used to visualize the effect of a quasi-liquid layer on the reflectivity of the complicated ice-FAS structure (see Fig. 5.23). To model the FAS film, the best fit to the data measured at –0.4 °C was used. On the top interface to the ice an additional quasi-liquid layer was added. The premolten layer was assumed to have the same density as measured in previous experiments ($\rho_e = 1.2\rho_{e,H2O}$). Figure 5.23 shows the calculated reflectivity for a 5 Å thick (bottom curves) and for a 10 Å thick (top curves, displaced by a factor of 100) premolten region. Each layer thickness has been combined with a roughness of 1, 5 and 10 Å, respectively.

The calculated reflectivity shows that a layer of 10 Å or greater thickness leads to an additional minimum in the broad oscillation if the roughness is smaller than 5 Å. Even for larger roughnesses, the position of the first minimum and the intensity in the region between 0.1 Å^{-1} and 0.2 Å^{-1} are different compared to the reflectivity without a quasi-liquid layer (green line). The presence of a quasi-liquid layer with a thickness of $d \geq 10$ Åcan be excluded, assuming it has a similar density as observed at other interfaces. A layer of 5 Å or less can not be excluded, except if the roughness is much smaller than 5 Å. In this case a strong minimum appears at $Q = 0.53$ Å^{-1}, which is not observed in the data.

In summary, the presence of a small quasi-liquid layer at the interface between self-assembled monolayers of OTS and FAS can not be excluded, but there is no indication for it. It is important to note that these measurements have been performed with a very small radiation dose to conserve the organic molecules. On no other sample premelting has been observed with radiation doses this small. Stronger irradiation of the sample results in irreversible decomposition of the organic molecules.

5.5 Summary

In total, eleven samples have been investigated in this work. Only in two cases (sample 6 and 8) interface melting could be detected. In three cases (samples 5, 7 and 9) there is clear evidence that either premelting is absent or that the premolten layer exhibits a density close to the surrounding ice. X-ray reflectivity relies on a proper matching of the density contrast between the ice, the substrate and any possible layer in between. This contrast matching can not be fulfilled in case of the ice-silver interface (sample 3) because the electron density of the silver is too high. A perfect OTS layer would provide good contrast matching, but the OTS layer used in this work (sample 11) grew with too small density. The density contrast for the ice-FAS interface (sample 10) does only allow the confirmation of premelting in ideal conditions, i.e. thick quasi-liquid layer and low roughness. The remaining samples (1,2 and 4) did not provide reflectivity curves of sufficient quality. The results from samples 5 to 9, for which the presence or absence of premelting could be determined, will be discussed in the following chapter.

Chapter 6

Discussion

Most of this chapter will be dedicated to the discussion of the results obtained from the ice-quartz and ice-silica interfaces. First, the two measurements that showed interface melting will be discussed. The growth law for the quasi-liquid layer will be deduced and the results will be compared to other works. Finally we will discuss the widely varying melting behavior of ice at the interfaces studied in this work.

6.1 Growth law

The growth law for the quasi-liquid layer thickness is deduced from the temperature dependence $L(T - T_M)$. Since interface melting was only observed at the ice-silica and ice-quartz interface, the data for the discussion of the growth law are solely originating from these two interfaces.

6.1.1 Correction for radiation effects

The temperature dependence of the quasi-liquid layer thickness obtained for both the quartz (stars) and the silica sample (circles) is shown in Fig. 6.1. There is a lot of scattering in the data. The expected logarithmic growth law for systems governed by short-range forces is not obvious from the data. However, it was observed in the experiments that continuous beam irradiation increases the thickness of the quasi-liquid layer.

The average photon flux was determined to $\phi \approx 10^{10}$ photons per second in uniform filling mode. The number of photons absorbed by the sample is given by

$$\alpha = \phi \mu_{en} l t. \tag{6.1}$$

where μ_{en} is the mass energy absorption coefficient, denoting the attenuation of the beam per length unit, taking into account all the absorption channels. l is the

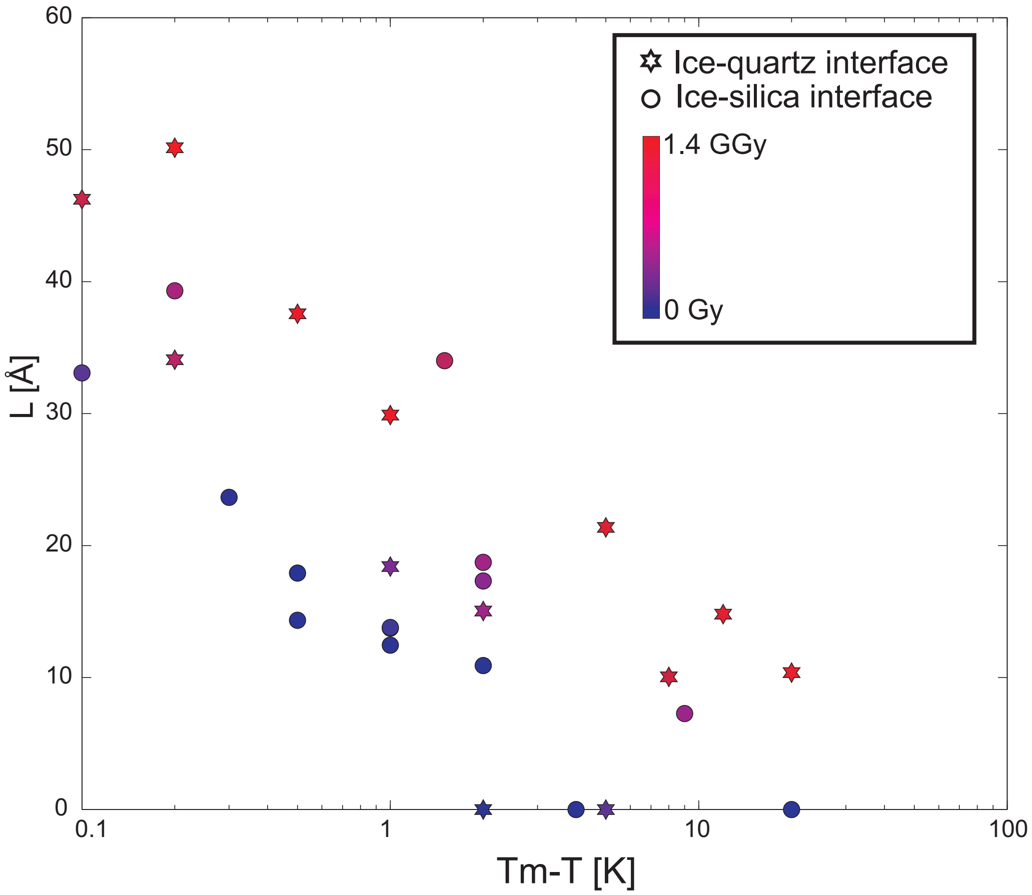

Figure 6.1: Quasi-liquid layer thickness without correction for radiation effects (Stars: ice-quartz interface, circles: ice-silica interface). The color of the symbols indicates the radiation dose to the sample, ranging from 0 to 1.4 GGy.

path length and t the irradiation time. The value of $\frac{\mu_{en}}{\rho} = 0.0265\frac{cm^2}{g}$ has been taken from the NIST website [85]. The radiation dose rate is defined as the energy deposited within 1 kg of material per second. Each photon carries an energy of $\epsilon = 72.5$ keV. Expressing the volume $V = l \cdot \sigma$, with the length l along the beam and the beam cross-section σ, the radiation dose rate is given by

$$\dot{D} = \frac{E}{\rho V t} = \frac{\alpha \cdot \epsilon}{\rho \sigma l} = \frac{\phi \cdot \epsilon}{\sigma} \frac{\mu_{en}}{\rho}. \tag{6.2}$$

With the beam cross section $\sigma = 25\mu m \cdot 5\mu m$ the total dose rate is given as

$$\dot{D} = 1.6 \cdot 10^{16} \frac{\mathrm{keV}}{\mathrm{gs}} = 2.56 \frac{\mathrm{kGy}}{\mathrm{s}}. \tag{6.3}$$

In Fig. 6.1, the radiation dose for each measurement is coded by the color of the symbol, ranging from blue, for a virgin surface, to red for high radiation doses. The highest radiation dose measured was 1.4 GGy. The importance of correcting for radiation damage is obvious from the diagram. All the symbols corresponding to high radiation doses gather at the top of the diagram, while the blue symbols are found at the bottom.

The measurements that have been performed at the same temperature with different radiation doses allow an estimation of the radiation-induced layer growth. The evolution of the layer thickness with radiation dose is shown in Fig. 6.2. The symbols show the measured layer thicknesses, the lines are linear fits to the data. The inset shows the slope of the fitted linear function as a function of temperature. The radiation induced growth is larger at the ice-quartz interface. Unfortunately, the measured data points are not sufficient to isolate a clear temperature trend. The average radiation growth is $\mathrm{d}L/\mathrm{d}D = 22 \pm 5$ Å/GGy for the ice-quartz interface and $\mathrm{d}L/\mathrm{d}D = 11 \pm 5$ Å/GGy for the ice-silica interface.

Using these values it is possible to correct the thickness of the quasi-liquid layer for radiation effects

$$L_0 = L_m - \frac{\mathrm{d}L}{\mathrm{d}D} \cdot D. \tag{6.4}$$

The resulting growth law is shown in Fig. 6.3. The correction was not applied to layers of zero thickness, since it is unknown which radiation dose is necessary to initiate premelting. The scattering of the data points has been significantly reduced. The presence of a negative layer thickness is an artifact. A negative layer thickness implies only that no interface melting is observable on the non-irradiated interfaces. The negative value allows to estimate the radiation dose necessary to initiate interface melting.

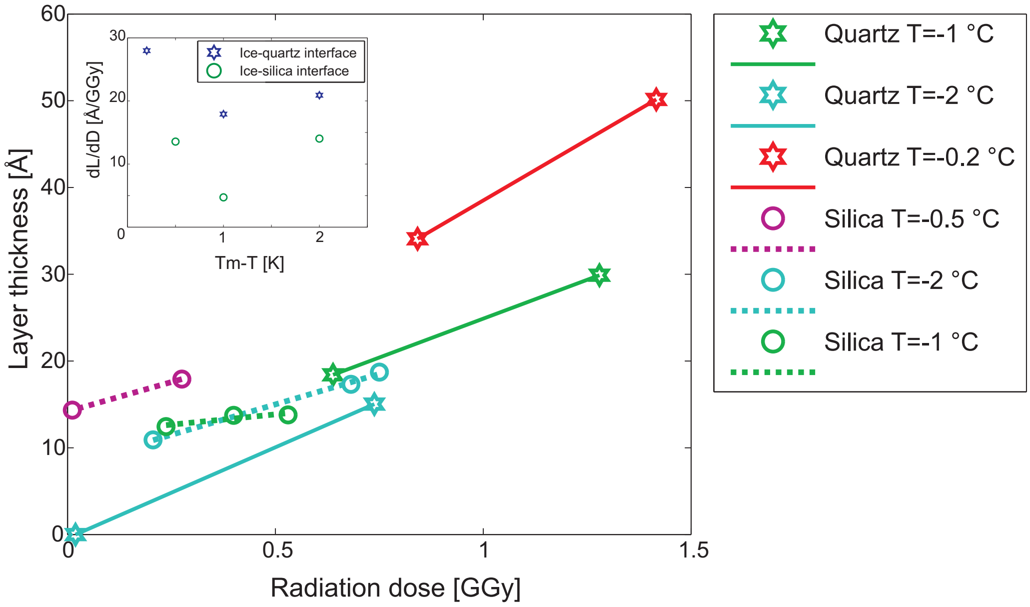

Figure 6.2: Growth of the quasi-liquid layer with irradiation dose. Only the data points for which the same temperature has been measured with different radiation times are shown. The stars show results for the ice-quartz interface, the circles denote the layer thickness at the ice-silica interface. The inset shows the derivative of the growth as a function of temperature.

6.1.2 Experimental errors

Temperature

The data sets from the ice-silica and ice-quartz interfaces have been measured with the peltier cooling chamber (see chapter 4.1.3). Although this chamber has very high relative temperature stability, the absolute temperature is not defined with the same accuracy, since the cooling is only done from two sides of the sample. The low heat conductivity of the ice can lead to temperature gradients on the sample.

In such a geometry it is difficult to determine the precise temperature. In all experiments a temperature sensor has been molten into the bulk ice. The heat conduction through the wire to the sensor was too strong to give an accurate reading. The air surrounding the sample was never cooler than +16 °C over the course of an experiment, which in turn leads to a measured temperature that is too high. The geometry of each sample is different, as well as the exact positioning of the sensor and its cabling.

Since the absolute temperature of the ice at the interface could not be measured with high accuracy, the temperature of the cooling plates was measured

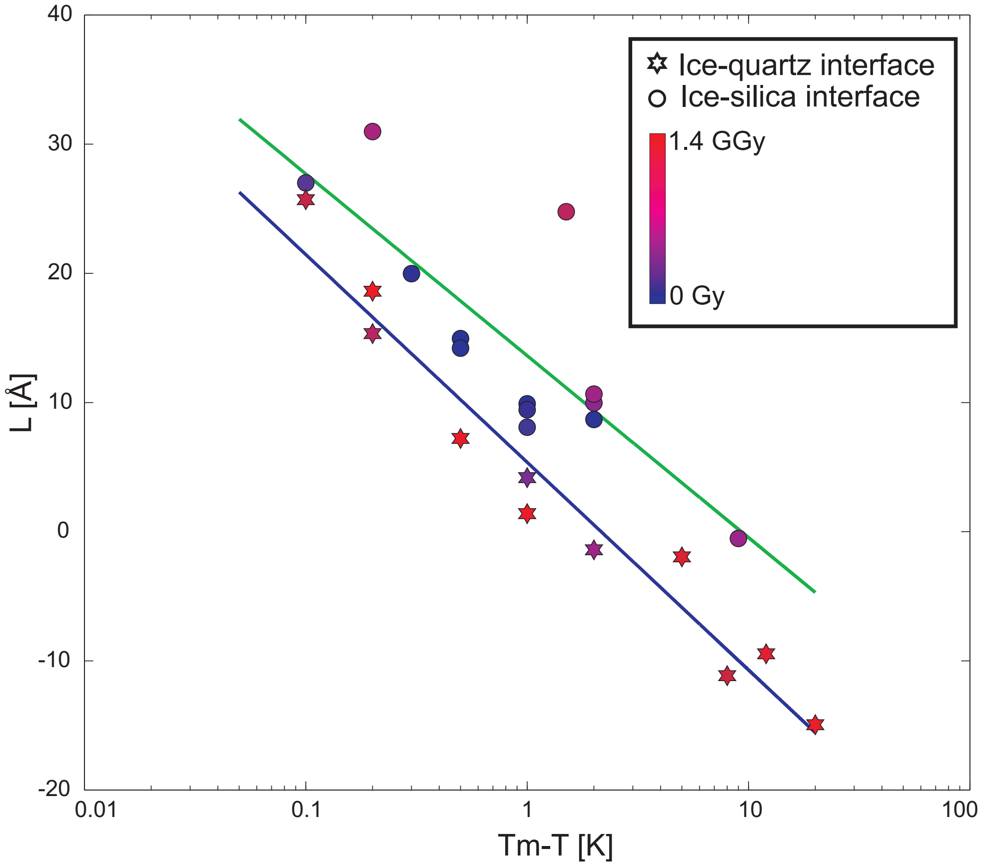

Figure 6.3: Radiation-corrected growth of the ice-silica (circles) and ice-quartz (stars) interface. The solid lines are guides for the eye. A negative layer thickness indicates that no premelting will be observed on a non-irradiated interface.

instead. The temperature of the cooling plates can be measured with an accuracy of 10 mK using calibrated temperature sensors. However, due to temperature gradients across the sample, the temperature of the cooling plate will differ from the temperature of the measured interface.

Simon Engemann performed some measurements of the temperature gradients in the ice [3]. The temperature gradient inside the samples between the cooling plates (y direction) was smaller than ±2.5 mK/mm, for temperatures close to the melting point. This result can be directly applied to our samples, since their geometry is similar (24 mm length compared to 25.4 mm for the samples presented in this work). The temperature of the ice at the measured spot might be up to 50 mK higher than the temperature of the cooling plates.

Temperature gradients parallel to the heating plates (x direction) will lead to the observation of a reflectivity that is averaged over different temperatures. Since the sample has constant cooling in the x direction this gradient is expected to be small. In addition, the footprint of the beam decreases with increasing angle. The important part of the reflectivity is measured at large angles, where the footprint is small. For this reason the experimental error of temperature gradients in the x direction is negligible.

Taking all into account, the total uncertainty of temperature is estimated to $\Delta T =^{+60}_{-10}$ mK.

Layer thickness

The thickness of the premolten layer can be determined with very high accuracy from the reflectivity curve. Its experimental error can be considered negligible compared to other experimental errors. Much larger is the error associated with radiation damage. Since the nature of the radiation damage is not understood, it is impossible to predict the functional dependence on dose and temperature. For most temperatures only one or two measurements were performed with different radiation dose, allowing only to employ a linear growth law. As no temperature trend was visible, the radiation induced growth of the quasi-liquid layer was considered to be temperature-independent and the values for different temperatures averaged.

The experimental error in the determination of L_0 is

$$\Delta L_0 = \left| \frac{\partial L_0}{\partial \frac{\mathrm{d}L}{\mathrm{d}D}} \right| \cdot \Delta \frac{\mathrm{d}L}{\mathrm{d}D} + \left| \frac{\partial L_0}{\partial D} \right| \cdot \Delta D. \tag{6.5}$$

The standard deviation obtained in section 6.1.1 is used for $\Delta \frac{\mathrm{d}L}{\mathrm{d}D}$. The error of the dose calculation is determined by the uncertainty in the irradiation time Δt_{irr} and the uncertainty of the dose rate calculation $\Delta\dot{D}$

$$\Delta D = t_{irr} \cdot \Delta\dot{D} + \dot{D} \cdot \Delta t_{irr}. \tag{6.6}$$

The irradiation time is well known, however, measuring a full reflectivity curve takes up to 30 minutes. Most of the measurements are performed from low to high angles. The large momentum transfer part of the reflectivity is therefore more exposed to radiation than the part close to the edge of total reflection. Fortunately, radiation induced growth is slow, in 30 minutes the thickness of the quasi-liquid layer increases by only 0.05 Å for the ice-silica and 0.1 Å for the ice-quartz interface. Since the time for a single measurement is much smaller than the total irradiation time, no correction has to be applied and Δt_{irr} is set to ±15 minutes.

The radiation dose rate is calculated with Eq. 6.2. The beam cross-section σ is known from knife edge scans with negligible error. The energy bandwidth of the monochromator is $\Delta\epsilon = \pm 0.1 keV$ (see chapter 4.2.1). A rather large error of 10% is attributed to the flux Φ. This error accounts for differences in the storage ring current during the measurements. The mass energy-absorption coefficient is taken from the NIST database, an error of 5% has been estimated for the accuracy of the calculations. The total error of the dose rate is then given by

$$\Delta\dot{D} = \left|\frac{\epsilon\mu_{en}}{\sigma\rho}\right| \Delta\Phi + \left|\frac{\Phi\mu_{en}}{\sigma\rho}\right| \Delta\epsilon + \left|\frac{\Phi\epsilon}{\sigma}\right| \Delta\frac{\mu_{en}}{\rho} = \pm 0.4\frac{kGy}{s}. \tag{6.7}$$

6.1.3 Discussion of the silica and the quartz substrate

The results from the measurements at the ice-silica interface are shown as circles in Fig. 6.4. From the theory a logarithmic growth law is expected (see chapter 2.5.1). The blue line shows the fit of Eq. 2.10 to the data, taking into account the experimental errors calculated in section 6.1.2. The obtained growth law is

$$L(T) = 5.0 \pm 0.7\,\text{Å} \ln\left(\frac{-9 \pm 3.5°\text{C}}{(T_M - T)}\right). \tag{6.8}$$

The correlation length of the quasi-liquid layer is $\xi_{Silica} = 5.0 \pm 0.7$ Å, the onset temperature for premelting is $T_{O,Silica} = -9.3 \pm 3.5$ °C. The layer thicknesses, which have been measured several times at the same temperature, coincide very well. This indicates that averaging the radiation induced growth rate over all temperatures is a good approximation. The two data points measured with highest radiation dose display a larger deviation from the growth law than the other data points. This indicates nonlinear effects at very high radiation doses or thick layers. However, no such effects were observed at the ice-quartz interface.

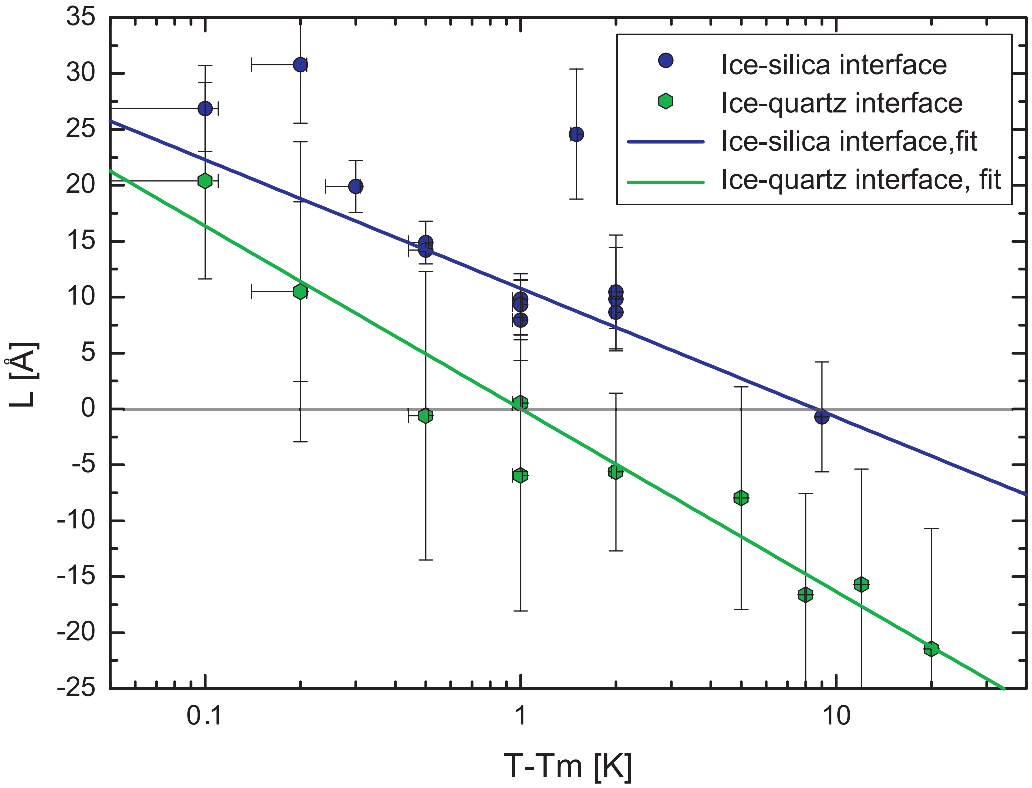

Figure 6.4: Growth law for the ice-silica and the ice-quartz interface with the error bars calculated in section 6.1.2. Fits using a logarithmic growth law are shown as lines.

The fit to the measured quasi-liquid layer thicknesses is indicated by the green line in Fig. 6.4 resulting in

$$L(T) = 7 \pm 1.7\ \text{Å} \ln\left(\frac{-1.0 \pm 0.4°\text{C}}{(T_M - T)}\right). \tag{6.9}$$

The scattering of the data is much smaller than in the case of the ice-silica interface. The correlation length is $\xi_{Quartz} = 7 \pm 1.7$ Å, significantly higher than for the quasi-liquid layer at the ice-silica interface. The onset temperature is $T_{O,Quartz} = -1.0 \pm 0.4$ °C. The error of the quasi-liquid layer thickness is larger for the ice-quartz interface. This is because the irradiation time is longer, thus the uncertainty in the layer radiation growth has a larger impact.

The onset temperature of premelting is significantly higher for the quartz sample. This indicates that the crystalline substrate has a stabilizing effect on the ice structure, preventing the formation of the disordered phase. Quartz crystallizes in a hexagonal lattice. The basal plane of the substrate was oriented parallel to the basal plane of the ice. However, the structure of both materials is different and the in-plane orientation of the ice remained undetermined. The structure of the first ice layers may be further distorted or misaligned due to the bonding process.

The correlation length of pure supercooled water has been determined in small angle scattering experiments [96]. In the temperature range of interest, a temperature-independent correlation length of $\xi_{H_2O} \approx$ 3.6 — 3.8 Åwas found. The correlation length of the quasi-liquid layer is larger, closer to the values obtained for supercooled water [97] where a correlation length of 8 Åwas found at $T = -20$ °C. Since the quasi-liquid layer is a strongly confined layer and is influenced by the ice crystal lattice, a higher correlation length is expected. Since the experimental data for the bulk water exhibit a large uncertainty it is only possible to note that the measured correlation length is similar to the correlation length of supercooled water or slightly higher than the correlation length of water at room temperature. The correlation length for the ice-quartz interface is higher than for the ice-silica interface. As mentioned before this might be attributed to the presence of the crystalline substrate.

6.2 Density of the quasi-liquid layer

While the correlation length of the quasi-liquid layer is similar to the value of bulk water, the electron density is much higher (see tables 5.2 and 5.4). The average electron density is similar for both substrates. This indicates that the phenomena leading to this increased density does not depend on the crystallinity of the substrate.

The electron density difference between the quasi-liquid layer and its surroundings determines the amplitude of the oscillations in the reflectivity curve. Since only one layer is present at the interface, the density difference is a robust fit parameter. The density of the quasi-liquid layer is found to be approximately 25% higher than the density of bulk water. Since the compressibility of water is $\kappa = 0.53$ 1/GPa at 0 °C [88], the pressure needed to induce a compression of the ice $\frac{\Delta V}{V} = -\sqrt[3]{1.25} = -1.077$ is

$$\Delta p = -\kappa^{-1} \frac{\Delta V}{V} = 2.0 \mathrm{GPa}. \tag{6.10}$$

Obviously, there is no physical explanation for this pressure and thus a mechanical compression can be excluded. In the following other explanations such as charging, radiation damage, impurities and the stabilization of a high density water phase are discussed.

6.2.1 Radiation effects

High energy photons interact with matter mainly via the photoeffect and to a lesser extent via the Compton effect. Both of these processes create free electrons. This can affect the sample in two ways: By charging the interface and by damaging the chemical bonds of the substrate material.

The substrates used in this work are insulators. Therefore, the sample is electrically isolated from the chamber and charging can take place. In order to increase the electron density by the measured amount an additional electron density of 0.084 Å^{-3} is required. This corresponds to a charge density of $\rho_e = 1.34 \cdot 10^{10} \frac{\mathrm{C}}{\mathrm{m}^3}$. There are two reasons that speak against this model. First, it raises the question why the free electrons do not recombine with the positive ions created during ionization. Second, although the total charge is not very high, it is assumed to be confined to a very small volume, thus leading to a high charge density, which is energetically unfavorable.

The strong influence of radiation damage on the thickness of the quasi-liquid layer has already been discussed. It is possible that the measured density is also influenced by this effect. After several days of irradiation, the beam path inside the bulk ice becomes visible as a faint line. This indicates a structural change in the material, probably due to the creation of gas bubbles from the radiolysis of the water molecules. As a result, bubbles of hydrogen and oxygen gas are produced. If these bubbles reach a sub-micrometer diameter, they scatter visible light. However, since this process changes the structure, but not the number of molecules or electrons in the ice, it is not changing the electron density of the substrate.

The gas molecules might be able to escape the bubble by diffusing into the ice. This seems to be unlikely, however, since the solubility of gases in ice is very low. A more probable way of mass transport would be through a percolated network of bubbles. When the bubbles get large enough to overlap each other, gas molecules might escape the sample. Unfortunately, there are no data available on the structure of this radiation zone. The high vapor pressure and the high mobility of the ice surface prevent the preparation of ex-situ samples for imaging techniques such as atomic force microscopy and electron microscopy.

An increase in electron density could be observed if the substrate dissolves in the ice. The solubility of silica in water is very low and can be expected to be almost zero in ice. The radiolysis of ice creates OH-radicals, H_2O_2 and other aggressive molecules that may attack the surface of the substrate and thereby enhance the solubility. However, as indicated in Fig. 6.5, the premolten region has to incorporate 30% silica to reach the observed electron density. If it is assumed that the native density of the quasi-liquid layer is equal to the density of water, this value drops to 25%, which is still unphysical. Even in basic solutions the

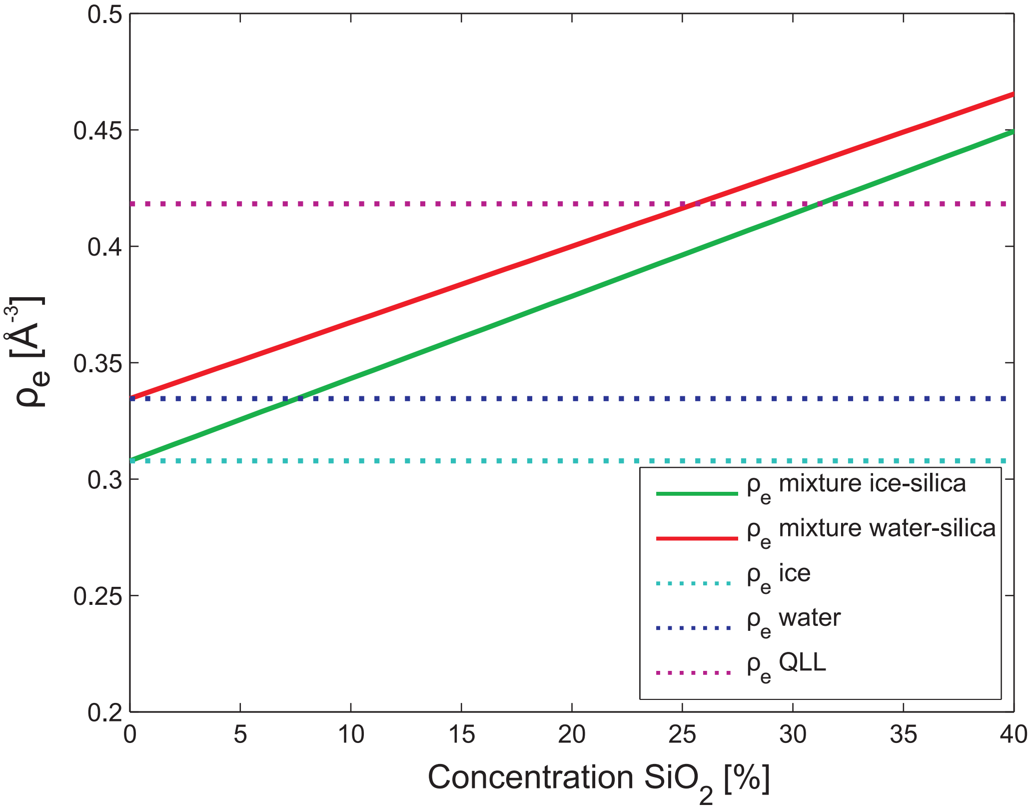

Figure 6.5: Observed electron density of the quasi-liquid layer as function of dissolved silica (in atomic %). Green line: electron density for a mixture of bulk ice and silica. Red line: electron density for a mixture of water and silica. Dashed lines denote the values for the electron density of pure water, ice and the quasi-liquid layer.

solubility of silica is less than 0.1%.

Radiation damage has a large influence on the premelting and it is likely that it will also influence the density of the quasi-liquid layer. However, a radiation damage mechanism inducing an increase in electron density could not be identified.

6.2.2 Impurities

The solution of impurities into the premolten region could account for the increased electron density. The ice single crystals can be considered to be free of impurities, since they are made from ultra-pure water and have been zone melted. This method removes almost all impurities still inside the ice. Great care was

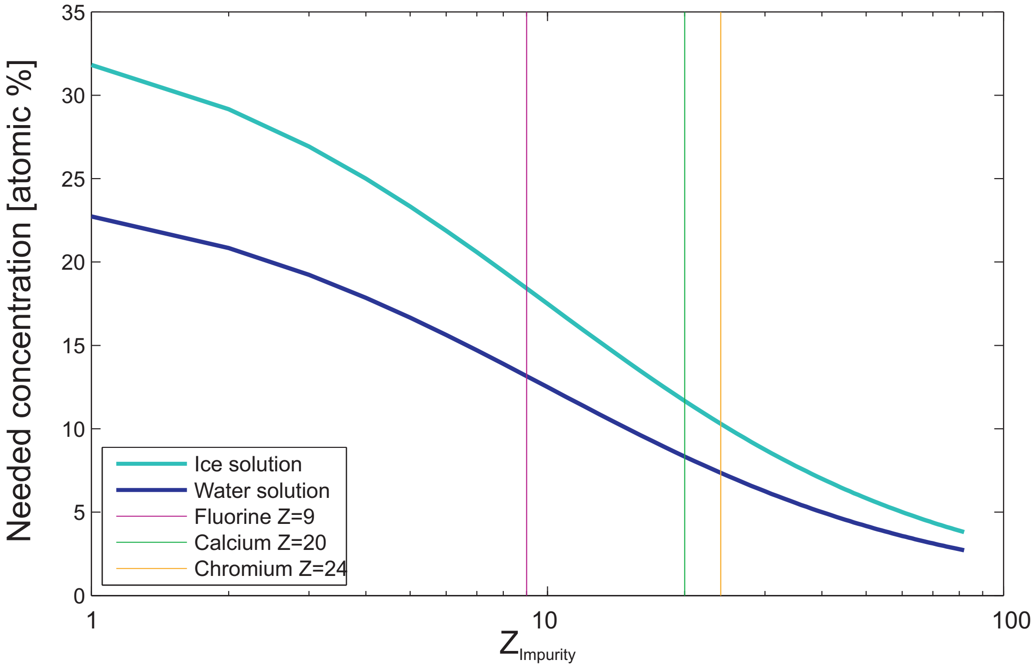

Figure 6.6: Concentration of impurities needed to observe the electron density measured for the quasi-liquid layer, calculated with Eq. 6.11. Cyan line: Assuming the pure premolten layer has a density equal to ice. Blue line: Assuming the native electron density of the quasi-liquid layer is equal to water. Vertical lines: Possible impurities.

taken to keep the samples clean during sample preparation. The substrates have been etched with chromium sulfuric acid and rinsed with milli-Q water. Once the substrate is bonded to the ice crystal, the interface is protected from impurities.

Sources of impurities are hydrocarbons floating in air and settling on the surface of the substrate between cleaning and bonding. Since the electron density of these molecules is small they should not increase the electron density significantly. Likewise, the air was contaminated with Calcium, since construction work has been performed inside the buildings during the time of sample preparation. The milli-Q water used in the sample preparation had a specific resistance of 12 MΩ·cm, which excludes it as a source of ionic contaminations. Ions may, however, have been dissolved from the walls of the glass bottle that contained the water. Finally, although careful rinsing was applied, some chromium ions could be left on the substrate surface after etching. However, all the possible sources of impurities account in the worst case for contaminations in the ppm regime.

Assuming that the small amount of impurities does not change the mass density of the quasi-liquid layer, the increase in electron density can be calculated as

$$\frac{\Delta \rho_e}{\rho_e} \approx \frac{\Delta f_{QLL}}{f_{QLL}} = \frac{f_{water} \cdot c + f_{impurity} \cdot (1-c)}{f_{water}}. \tag{6.11}$$

$f_{water} = 2f_{1,H} + f_{1,O}$ is the total structure factor of water, c is the concentration of the impurity with the structure factor $f_{1,impurity}$. Equation 6.11 is only a crude estimate, but it is sufficient to demonstrate the order of magnitude of the effect. In Fig. 6.6, the concentration necessary to obtain the observed electron density of the quasi-liquid layer is plotted as a function of the atomic number of the impurity. The cyan and blue lines show the result of the calculation for a premolten region with the native density of ice and water, respectively. The atomic numbers of calcium and chromium are marked with a green and orange line, respectively. Fluorine has been marked with a magenta line, since it exhibits the highest diffusion coefficient in ice. It could diffuse fast enough through the ice crystal to contaminate the interface between the bonding process and the actual reflectivity experiments at the synchrotron radiation source [98]. However, no source of fluorine contamination could be identified.

Figure 6.6 shows that very high concentrations of impurities are necessary to affect the density of the quasi-liquid layer strong enough. Even for high-Z elements, concentrations of several percent are required. Since this can be ruled out, impurities can be excluded as the source of the increased electron density in the quasi-liquid layer.

6.2.3 Stabilization of a high density water phase

After excluding experimental artifacts or the increase in the electron density via impurities, the possibility of an increased mass density has to be examined. As described at the beginning of this section, the increase in density can not be explained by a simple compression of the ice. An alternative explanation may be found in the formation of a different phase of water.

Ice is known to form several amorphous phases [9]. Due to their difference in density, they are labeled low-density amorphous (LDA), high-density-amorphous (HDA) and very high-density amorphous (VHDA) ice. VHDA can be formed by compressing HDA at 1.1 GPa. The resulting ice can be recovered to ambient pressure at 77 K and has a density of 1.25 g/cm^3 [4]. The fact that the density is approximately the same as the density observed for the premolten layer shows that it is possible to arrange water molecules in a disordered phase with the measured density.

Some water models [6] assume that the amorphous ices have liquid counterparts and that the bulk structure of water characterized by large density fluctuations between the two water states. One of this water phases has a low (LDW), the other a high density (HDW). Although experimental evidence for the existence of these water phases was found, they have never been observed directly. Here we speculate that confinement or the presence of an interface could stabilize one of the two phases. Since the quasi-liquid layer exhibits the same density as VHDA, which is interpreted as the amorphous counterpart of the HDW, the structure of the quasi-liquid might be similar to the structure of the high-density water phase. The critical point above which the two water phases become indistinguishable in the bulk is located at 220 K. Whether confinement and the presence of the SiO_2 interface are sufficient to stabilize the HDW phase so far away from equilibrium remains unclear.

As the term *quasi*-liquid layer infers, it is not surprising that the premolten region has physical properties that differ from bulk water. First, some crystalline order may remain inside the layer and second, the layer is confined in a space of several molecular diameters. High density water phases in nanoconfinement have already been found by Floquet et al. [5]. They investigated water confined inside zeolites with neutron diffraction. The zeolite structure features ring channels of 7.3 Å diameter. At 300 K, these channels fill with two water helices. The density of this confined water phase is 1.2 g/cm^3, remarkably close to the value found in this work. The helical structure found in the zeolites may be caused by structural commensurability during the growth of the water helices and is probably different from the water structure of the quasi-liquid layer found in this work. It shows, however, that it is possible to stabilize high density water phases in nanoconfinement.

In total, four interfaces showed interface melting in the reflectivity studies performed by Simon Engemann [65] (see chapter 2.6.5) and the work presented here. In all cases the density of the quasi-liquid layer is between 1.2 to 1.27 g/cm^3. The system investigated by Simon Engemann is the interface between ice and the native SiO_2 layer on silicon substrates. Since all four substrates consist of different forms of SiO_2, it is not possible to conclude whether the increased density in the quasi-liquid layer is induced by the substrate material or a generic property of premelting.

In summary, it seems very likely that the observed high electron density of the quasi-liquid layer is not an artifact of the sample preparation or the experiment technique. Instead, it seems to be related to the formation of a water phase with increased mass density in the confined premolten region. It is not possible to decide whether this phenomenon is a generic property of confined water layers or specific to water in contact with SiO_2 surfaces.

6.3 Suppressed premelting

The results discussed so far were all obtained on two samples during the beamtime of June 2005. These were the only two samples for which interface melting could be observed. There are some samples for which the quality of the data is not high enough to confirm the presence of interface melting. In three cases the presence of a quasi-liquid layer with a density different to the surrounding ice can be excluded. These are the ice-MgO interface (sample 9) and two particular ice-quartz and ice-silica interfaces (sample 5 and sample 7, respectively).

6.3.1 Suppression due to substrate properties

As discussed in chapter 2.5.1, the presence and properties of premelting depend on the interface energies involved. Interface melting has been observed at the ice-SiO_2 interface. But since the interface energy of the ice-MgO interface is different, it is not possible to predict the presence or absence of interface melting. In addition, the high density water phase observed for the silica and quartz sample might be unique to the SiO_2 system. If the density of a possibly existing quasi-liquid layer at the MgO interface is not sufficiently different from the density of bulk ice, it will not be observable with x-ray reflectivity.

Likewise, it is possible to explain the surprising absence of premelting on the quartz sample 5 by changes of the interface energy with respect to sample 6 (that showed premelting) due to the different in-plane orientation. Since the cold room was only equipped with a two-circle diffractometer, it is not possible to align the ice and the quartz crystal laterally. For this reason the angle between the lattice parameters $\vec{a}_{quartz}$ of the quartz lattice and $\vec{a}_{ice}$ of the ice lattice are not known before the experiment. The interface energy is expected to be different for different angles. At certain angles interface melting could be favored, while at others it might be suppressed.

It is, however, possible to determine the rotation between the ice and the quartz lattice during the x-ray scattering experiments. For the ice-quartz interface (sample 5), where no interface melting was observed, the angle is 15°; for the second ice-quartz interface (sample 6) exhibiting strong premelting, the angle is 24°. A change of 9° might be enough to dramatically change the configuration between the two crystalline lattices and thus stop the formation of a high density phase or suppress premelting.

While it is possible to find reasons why premelting is suppressed in the two discussed samples, similar arguments can not be found for sample 8, which is an ice-silica interface identical to sample 7. Sample 7 shows that the formation of a quasi-liquid layer with a high density water phase is favorable on silica. Since the material is amorphous, there are no structural changes due to different in-plane orientations. Even more puzzling is the fact that it was not possible to observe interface melting on sample 7 when it was examined again after five months (see chapter 5.1) under identical conditions. The only possible conclusion is that additional parameters are controlling the formation of the high-density quasi-liquid layer.

6.3.2 Suppression by hidden parameters

The only way to identify unknown parameters controlling interface melting is by investigating many samples with systematically varying parameters. This allows to isolate the parameters involved. However, since it is only possible to perform the experiments at the high energy beamline ID15A, a highly overbooked beamline at the ESRF, there is not enough beamtime available to do this.

From the results obtained most can be learned by comparing the two experiments performed on sample 7. Interface melting could be observed in June, while five months later interface melting could not be detected. Between the experiments the sample was kept inside the cold room at -16 °C. The sample has not been modified during this time, in particular the orientation or the properties of the substrate remained unchanged. Since it was possible to measure both times on the same spot of the sample, lateral inhomogeneities can be excluded. Therefore it can be concluded that the parameter suppressing interface melting must be time-dependent.

The interface is protected from impurities by the surrounding ice single crystal. The only impurities that can diffuse fast enough through ice to significantly change in concentration between the experiments are HF and NH_3 [9] [98]. Since neither of these chemicals were used during sample preparation, their presence can be excluded. All other impurities did not change in concentration. Impurities present on the interface during the first experiment were still present during the second.

The only parameter of the sample that depends on time is the relaxation of the ice crystal lattice. The particular recipe to bond the substrate to the ice single crystal induced most likely stress and defects within the interfacial region of the ice lattice. The sample was stored between the experiments for five months at -16 °Conly slightly below the melting point. The long storage at elevated temperature has an annealing effect on the crystal and allows the lattice to relax.

If this is the reason for the different observations between the two experiments, the following conclusion may be drawn: Since defects can only relax with time, but not build up, interface melting is suppressed in the presence of a *relaxed* lattice. The high-density quasi-liquid layer forms only in samples that have a large amount of disorder left from the sample preparation. This surprising conclusion will be discussed in the next section.

It is important to note that the argument of insufficient disorder for starting the premelting can also be applied to the other interfaces that do not show premelting. Currently, we have no possibility to measure the level of disorder in the interfacial region. Therefore it is not possible to conclude that interface melting is unfavorable at MgO interfaces or that certain orientations between the quartz and ice crystal lattice suppress interface melting.

6.4 Disorder as the origin of premelting?

In both samples that showed premelting the quasi-liquid layer was only detectable when two conditions were fulfilled. The presence of disorder from the sample preparation and the absorption of a high radiation dose. The irradiation of the ice crystal lattice creates defects by ionizing and hydrolyzing the water molecules. The question arises if this imperfectness of the lattice is needed for the disordered layer to form.

The formation of a quasi-liquid layer is a disordering transformation. Defects and strain, constituting disorder in the lattice, are assumed to work in favor of this phenomenon. In addition the structural transformation could require a certain mobility of the water molecules, especially if a structurally very different high-density phase has to be formed. It might be possible that the required mobility of the water molecules is only achieved via the combination of radiation damage and defects from the sample preparation.

Does this suggest that the observed premelting is not a natural phenomenon, but only an artifact of the exposure to radiation? Fortunately, experiments with non-radiative methods, such as ellipsometry and quartz micro balance experiments, confirm the presence of interface melting (see chapter 2.6). Observations of natural phenomena controlled by premelting confirm its presence in nature (see chapter 2.7). However, there is a substantial difference in the quality of the ice interface.

In a natural environment, the ice will always be polycrystalline, with many defects and impurities, especially near the surface and interface region. Gases and salts, which are dissolved in the water, will segregate to form little bubbles of gas and solution, respectively. The interface will always be very rough and curved. In contrast, the measurements discussed in this work were performed on perfect single crystals of very high purity. The interfaces are smooth on a molecular scale. This ”unnatural” perfectness of the system, and the low mobility of the molecules in the perfect lattice, might be the reason why interface melting was only observed after producing enough defects through sample preparation and irradiation.

6.5 Comparison with other works

Obviously, the results presented in this work have to be compared with the results by Simon Engemann (see chapter 2.6.5). In his work two interfaces were investigated. Both interfaces were prepared from silicon substrates covered with native SiO_2 layers. The surface morphology of one substrate was similar to the substrates presented here, while the other substrate exhibited strong correlations in the surface roughness.

A radiation dose of similar value was required to initiate interface melting. The main difference between the two investigations is the effect of radiation on the sample. While for the ice-quartz and ice-silica interface discussed in this work, the thickness of the quasi-liquid layer kept growing with increasing radiation dose, the thickness of the quasi-liquid layer remained stable under irradiation for the silicon substrate. Once a sufficient radiation dose had been deposited to start premelting, the thickness was depending only on the temperature and the interface melting was reversible. In addition, samples measured a second time several months later still showed interface melting with exactly the same layer thickness.

The origin for this different behavior remains unclear. Although the materials at the interface are similar (amorphous SiO_2), there are important differences. The bulk silicon is conducting, leading to a better grounding of the sample. It is also a better heat conductor, leading to smaller temperature gradients in the interfacial region. On the other hand, both effects should be irrelevant for the observations presented in this work. The difference in sample preparation seems to be more important. To grow the native oxide layer, the samples have been etched with highly concentrated hydrofluoric acid [3]. Although careful rinsing with ultra-pure water was performed, some fluorides may remain on the interface and diffuse into the ice. Then the sample was left in air for several days to form the oxide layer. This leads to surface contamination with hydrocarbons. It was not possible to quantify how well the contaminants can be removed by the cleaning process before substrate bonding.

The substrate surfaces prepared by Simon Engemann in this way were hydrophobic. It is known that the irradiation of hydrophobic silicon surfaces in an aqueous environment leads to a hydrophilic surface termination. This change in the surface properties might promote premelting. However, the substrates used in this thesis were prepared with a hydrophilic surface and show the same phenomenon. For this reason, the radiation-induced change of the hydrophobicity of the interface can not be the only reason why irradiation is required to initiate premelting.

The reason why the thickness of the quasi-liquid layer was stable under irradiation in previous investigations [3] remains opaque, but the resulting properties of premelting can be compared to the results from this work. For the flat silicon-SiO_2

substrate a logarithmic growth law was found

$$L = 3.7\text{Å} \ln\left(\frac{-47°\text{C}}{T_M - T}\right). \tag{6.12}$$

Since the native SiO_2 layer is amorphous, a growth law similar to the ice-silica interface is expected. The correlation length is slightly smaller than the one measured for the silica substrate ($\xi_{Silica} = 5.0 \pm 0.7$ Å). The onset temperature is much lower, which may be related to the interface energy, which is a material property and can be different for both samples.

The interface with correlated surface roughness showed a larger correlation length of $\xi_{cor} = 8.2$ Å, which is closer to the value observed at the ice-quartz interface investigated in this work ($\xi_{Quartz} = 7 \pm 1.7$ Å). This is an additional indication that the presence of correlated surface roughness of the substrate gives rise to a larger correlation length in the quasi-liquid layer.

It is more difficult to compare the results with other works. Most of the experiments investigating premelting have been performed at the free ice surface. Experiments done with ellipsometry (see chapter 2.6.1) could not observe interface melting at the smooth silica-ice interface, which is in agreement with this work, since they did not use a radiative technique. Similar to this work, premelting was detected when the interface was perturbed by roughening the substrate or introducing impurities. This supports the idea that interface melting is suppressed at perfect interfaces.

Considering investigations of premelting by AFM tips (see chapter 2.6.3), the work of Pittenger et al. is closest to the observations in this work. The material of the cantilever was (boron-doped) silicon. The ice was polycrystalline. At -1 °C a thickness of 11 Å was obtained for the quasi-liquid layer, exactly the same value as has been observed in this work at the ice-silica interface. The agreement is less perfect at -2.6 °C where a quasi-liquid layer of 2.6 Å thickness (6 Å for the ice-silica interface) was found. Due to the differences in material and geometry and the different material properties probed by the two techniques, deviations are not surprising.

In summary, the results obtained in this work are similar to those obtained by other experiments. The largest uncertainty is the influence of radiation damage. The final chapter will summarize the results and discuss solutions to overcome the encountered problems in future experiments.

Chapter 7

Conclusions and Outlook

As mentioned in the introduction, the work presented here is based on the PhD thesis of Simon Engemann [3], where interface melting of ice was reproducibly observed at the ice-SiO_2 interface. The goal of this thesis was to broaden the understanding of the interface melting of ice by investigating the influence of different substrate parameters (morphology, impurities, ...) on premelting. Since the results of the original work by Simon Engemann could not be reproduced in the experiments performed for this work done, it is difficult to interpret the results.

Clearly, interface melting can be observed at the ice-SiO_2 interface under some conditions. However, it remains difficult to isolate these conditions. In all the experiments employing x-ray refraction, premelting could only be observed upon irradiating the sample. The effect of the radiation remains unclear. At present it is not clear whether interface melting does not set in without irradiation or whether it is only undetectable in x-ray refraction. The fact that interface melting has been observed by non-irradiative techniques indicates the second case, although most of these experiments were performed on polycrystals and interfaces of lower quality. The concept of suppressed melting due to a too high degree of structural perfectness can therefore not be excluded.

In this work, not all of the irradiated interfaces showed premelting. Furthermore, one sample showed premelting during one experimental campaign and not during a second beamtime. This indicates that additional parameters play an important role. Although there was not enough beamtime available to proof this hypothesis, there are indications that an additional source of disorder is required to initiate premelting. Possible sources are defects in the crystalline lattice from sample preparation or impurities.

If interface melting is observable, the quasi-liquid layer always shows a density that is approximately 20% higher than the density of bulk water. It can not be excluded that this is an artifact from radiation damage, but it is more likely to be the manifestation of a confined high density water phase. The structure of this phase is probably close to the structure of very-high-density amorphous ice (VHDA), which exhibits similar density.

Due to the large uncertainties caused by the radiation-induced growth of the quasi-liquid layer, it is not possible to decide if the layer thickness is following a logarithmic or an algebraic growth law. Employing the theoretically expected algebraic growth law for the ice-silica interface we find

$$L = 5.0 \pm 0.7\,\text{Å} \ln\left(\frac{-9 \pm 3.5°\text{C}}{(T_M - T)}\right). \tag{7.1}$$

For the ice-quartz interface

$$L = 7 \pm 1.7\,\text{Å} \ln\left(\frac{-1.0 \pm 0.4°\text{C}}{(T_M - T)}\right) \tag{7.2}$$

is obtained. The resulting values for the correlation length seem reasonable. Due to the large scattering of values for the thickness of the quasi-liquid layer published by other authors on surface melting, it is always possible to find data sets that show comparable results. However, there are fewer publications investigating solid-solid interfaces. Unfortunately, these works were preformed on polycrystalline ice and are not fully comparable with this work. The thickness values found in this study agree well with AFM measurements.

The morphology of the substrates seems to influence premelting. Measurements performed on the ice-quartz interface show a significantly higher correlation length and smaller layer thicknesses than the measurements at ice interfaces in contact with amorphous substrates.

Although x-ray reflectivity allows to measure the layer thicknesses with high accuracy, the values obtained in this work have large uncertainties. This is mainly attributed to radiation-induced growth of the layer thickness. The growth rate changes during the experiments, which prevents an accurate extrapolation to zero radiation dose. This results in large error bars, especially for the ice-quartz interface, where the experiments have been performed with long irradiation times.

Premelting could not be observed on any other substrates than SiO_2. Since it is unclear which conditions lead to the suppression of premelting, it is not possible to exclude interface melting for ice in contact with other substrates. It is reasonable to assume that similar hidden parameters play a role at these substrates as in the case of SiO_2.

The largest uncertainties of the sample quality stem from the preparation. Although great care was taken to obtain reproducible interfaces, the results show that this was not achieved. This might be partially due to the construction work at the Max Planck Institute during most of the time of this thesis, which led to severe constraints in the laboratory work and a large amount of dust and impurities in the air.

In addition, it appears that the process of melting the substrate into the ice is not reproducible enough. Special care was taken to ensure that the molten layer recrystallized from the side of the single crystal, thereby retaining its perfect lattice. The interfaces look optically perfect, which proofs that this process works well on the micrometer length scale. On the other hand, the quasi-liquid layers relevant for this study are only a few molecular layers thick. The recrystallization process can not be well controlled on this length scale. It is not even possible to measure the lattice properties of this buried interface region. Removing the substrate would irreparably destroy this region.

The problem of irreproducible results does not only plague this work. Thickness values for the quasi-liquid layer found in the literature scatter in orders of magnitude, depending on the sample and techniques used. In addition, one can assume that groups that searched for interface melting, but could not observe it, did not necessarily publish their results. Results from groups using polycrystalline samples (which covers the largest part of the work performed on ice) can not be compared with each other, since the morphology (grain size, roughness, . . .) of the ice is different in each sample. The investigations performed on single crystals are more reliable, but as demonstrated in this work, the produced interfaces are not reproducible on the molecular scale. It is fundamental for the scientific progress in this field to find new methods of sample preparation to overcome these problems and retrieve comparable results by different groups.

As discussed before, melting the substrate into the sample does not allow to control the properties of the interface layers of ice on the molecular length scale. It has the additional limitation of only being possible for substrates that are not dissolved in water. For this reason it has been impossible to investigate the interface melting of ice in contact with ionic crystals.

It is difficult to imagine a way to bond the substrate into the ice single crystal without melting the ice. Assuming that it is possible to prepare the surface of a single crystal with sufficient smoothness, it should be possible to press the substrate several microns into the ice. But this will obviously lead to a large amount of damage in the ice lattice. Furthermore, any irregularities left after the preparation of the ice surface will be conserved at the interface. Small height differences could lead to areas of the interface where the ice is not in contact with the substrate.

Better results might be obtained by using a method similar to wire regelation, where a weightened wire travels through a block of ice without melting it. Through a combination of plastic creep and premelting, the ice flows around the wire and refreezes behind hit. Samples could be prepared by putting a weightened substrate on a well-prepared ice surface at temperatures close to the melting point. With time, the substrate would sink into the ice. However, the time scale and pressures needed for a substrate to sink several micrometers into the ice are difficult to estimate. The structure of an interface, that is prepared this way, is unknown.

Defects in the ice crystal lattice have to be expected, although they could be much smaller than the damage created by other techniques.

A higher degree of reproducibility of the interface properties could be expected from methods that directly grow the ice on the surface of the substrate. This could either be done by freezing water droplets or condensation from the vapor phase. In the course of this work we tried to create samples by submerging the substrate in degassed, ultra-pure water and freezing it. Care was taken that the freezing starts from the substrate. This should repel remaining gases and impurities from the surface. But the quality of the obtained ice was very low. Even though degassed water was used, many air bubbles formed close to the interface. The ice formed polycrystals with very large domains. This leads to a very badly defined ice interface with large lateral inhomogeneities.

An alternative is to cool the substrate to liquid nitrogen temperature. If high speed droplets impact on a very cold surface, they freeze into an amorphous state [9]. Once the surface is covered with ice, it can be heated to temperatures close to the melting point. The ice will then transform into hexagonal ice (by transforming first into metastable cubic ice). The advantage of this technique is, that it can be used to bond the ice to water soluble substrates such as ionic crystals. Unfortunately, the ice lattice at the interface will contain many defects and suffer from the same limitations as an interface created by normal droplet deposition techniques.

The most promising technique is the deposition of water vapor. This technique has already been used for infrared spectroscopy experiments by Sadtchenko et al. [72]. In this technique water vapor is introduced into a vacuum chamber that contains the substrate. If the substrate is the coldest point in the chamber, the vapor will condense preferably on the surface of the substrate. The advantage compared to deposition from the liquid phase is that this technique allows a much better control of the physical parameters of the deposition. Since the ice layer can grow on the whole surface at the same time, spatial inhomogeneities can be avoided. Depending on the temperature of the substrate surface and the pressure of the water vapor, different growth modes might be possible. The goal would be to control the growth of molecular ice layers on the substrate. While this technique will most likely create polycrystalline ice, a properly chosen parameter set might lead to epitaxial growth. Even if this is not possible, growing polycrystalline ice with reproducible properties and spatially homogeneous properties would be a large step forward.

The only way to unravel the hidden parameters in the interface melting of ice is to investigate many samples that differ in systematic ways. However, it is not possible to perform this work using high energy x-rays at ID15 due to the lack of beamtime. For this reason the use of medium energy x-rays (5-20 keV) should be considered.

Using this energy range gives access to many more beamlines at different syn-

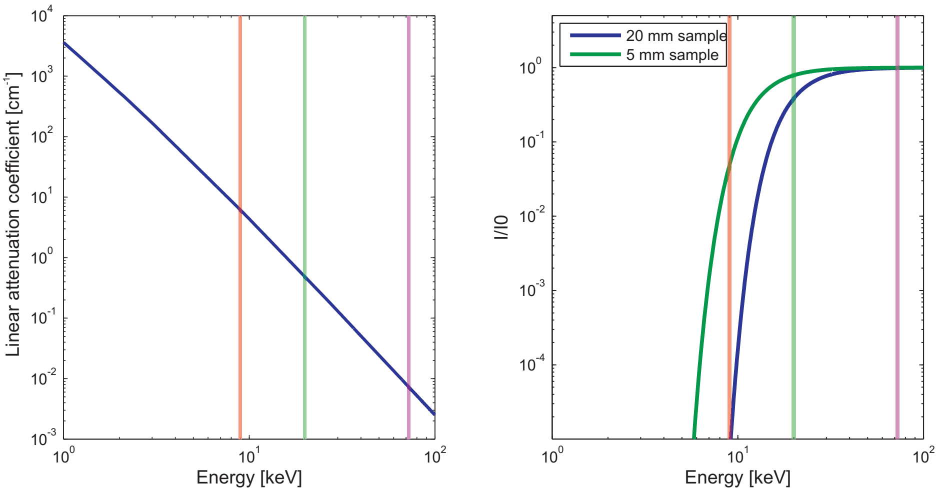

Figure 7.1: Effect of the photon energy on beam attenuation. Left: Linear attenuation coefficient for ice. The data are calculated from tabulated values [85]. Right: Transmitted intensity through an ice sample of 20 mm length and 5 mm length, respectively. Vertical lines: Photon energies for Cu K_α radiation (8.0 keV, orange), Mo K_α radiation (17.5 keV, green) and the radiation used in this work (72.5 keV, pink).

chrotrons. For the bulk of the work, however, it would be desirable not to depend on synchrotron radiation at all. Modern x-ray lab sources with rotating anodes can provide x-ray beams that allow the observation of the first part of the reflectivity curve. The access to this limited range is not enough for precision measurements, but could be used to determine which kind of samples should be measured at synchrotron sources. In addition, it would allow to exclude the samples that do not show any melting.

As the energy of the photons decreases, the attenuation of the x-ray beam in the sample becomes stronger. Figure 7.1 shows the rapid decrease of transmission through a sample when the x-ray energy decreases. The ice samples used in this work were typically approximately 20 mm long. The transmission through such a sample for Cu K_α radiation is only $5 \cdot 10^{-6}$, which reduces the available dynamic range in the reflectivity experiments too much. Reducing the length of the sample to 5 mm, which is the smallest size that can be handled in sample preparation, increases the transmission to 0.05. This value might be large enough to detect signatures of thick quasi-liquid layers. Better results can be achieved by using Mo K_α radiation, which has a transmission of almost 80% through a 5 mm long ice sample.

Reducing the length of the sample can decrease the quality of the obtained reflectivity curve, since the footprint of the beam exceeds the length of the sample surface at small incident angles. This reduces the intensity reflected from the sample. For a beam size of 0.1 mm and sample length of 5 mm, the full beam gets reflected at inclinations larger than 1.15°. Using Mo K_α radiation, this corresponds to a momentum transfer of 0.4 Å^{-1}.

More problems arise from the preparation of the ice samples. The bonding process becomes difficult when the size of the sample becomes very small. The samples have to be handled with higher precision, which is difficult to achieve in cold-room conditions. In addition, they become more fragile, increasing the danger of destroying the ice single crystal during the preparation process.

When using lower energies, momentum transfers are shifted to higher angles. This makes the experiments much easier because it reduces the accuracy needed in angular positioning. Furthermore, the effect of imperfect substrate surfaces, such as residual curvature, has a much smaller impact on the quality of the reflectivity curve.

Investigating interface melting of ice at lower energies necessitates some modifications of the experimental setup. However, the access to lab sources will allow the systematic investigation of the influences of substrate properties and sample preparation. It also allows to identify the best samples for precision measurements at synchrotron radiation sources.

As has been shown in this work, radiation damage is the largest contribution to the uncertainties of the results. It is therefore important to use complementary, non-irradiative techniques. Unfortunately, the choice of techniques that can access buried interfaces is rather limited.

Optical techniques, such as ellipsometry and infrared spectroscopy, can be employed to investigate the buried interface. However, it has so far not been possible to polish ice surfaces with sufficient quality high enough for these techniques. Therefore, the light beam has to pass through the substrate. This limits these techniques to optically transparent substrates. Another problem is that the spectrometer has to be included into the experimental chamber. This seems possible, but will require a completely new setup.

Ellipsometry seems to be the least complicated setup, but its resolution is rather limited. More information can be expected from infrared spectroscopy. The most surface sensitive technique is sum-frequency spectroscopy. Unfortunately, this setup is very complicated and the results difficult to interpret. In addition, no direct information about the thickness of the quasi-liquid layer is obtained. For this reasons, IR-spectroscopy seems the optical technique of choice to complement the x-ray measurements.

Neutron reflectivity is obviously a technique using radiation. But since the interactions of neutrons with matter are very different from x-rays, the resulting radiation damage can be expected to be totally different. This would make it interesting to compare the reflectivities taken by neutrons with those taken by x-rays. Unfortunately, the brilliance of neutron sources has not developed as fast as the brilliance of x-ray sources. Neutron reflectivity measurements have been performed by Simon Engemann [3] at the high-flux reactor of the Institute Laue Langevin (ILL) in Grenoble. However, even this intense neutron source does not provide enough flux. The lack of sufficient flux combined with the higher background compared to x-rays does not allow to access a large dynamic range. For this reason only a small momentum transfer range can be probed. Quasi-liquid layers with a typical thickness as it appears in interface melting are not detectable. New sources with dedicated reflectivity beamlines might be able to overcome these problems.

An interesting set of experiments could be performed at the ice solid-liquid interface. An ideal candidate for the liquid is heptane, since it is not reacting with ice. The electron density of heptane is $\rho_{e,C7H14} = 0.24$ Å^{-3}, which is lower than the electron density of ice. Evanescent wave fields can therefore be created inside the ice, by reflecting the x-ray beam below the critical angle. This opens the possibility to use grazing-incidence diffraction (GIXD) techniques to probe the structure of the quasi-liquid layer.

Since GIXD directly probes the structural order parameter it can detect premelting even if there is no change in the electron density. At interfaces where no premelting is visible in the x-ray reflectivity (XRR), use of GIXD allows to verify whether a quasi-liquid layer does not exist or if it has the same density than the surrounding ice. If premelting is observed in XRR, GIXD allows to better understand the structure of the high-density water phase.

Other advantages of investigating a solid-liquid interface include the improved access for other techniques. It has already been demonstrated that it is possible to perform AFM measurements at the ice-decane interface [52]. The simultaneous use of x-rays and complementary techniques would certainly help to increase our understanding of interface melting.

Bonding of the substrate to the ice is not required for this experiments and the contact between the ice and the liquid is always perfect. This excludes many uncertainties from the crystal preparation. However, it is still mandatory to prepare an ice surface that is smooth on the molecular scale. This can probably only be done by freezing the ice to a smooth substrate and shearing it off before the experiment. This process is described in [64]. Unfortunately, similar problems are encountered as in the bonding of solid substrates.

The properties of such a solid-liquid interface might resemble more the properties of the free ice surface than to solid-solid interface, without suffering from the sublimation/condensation problems encountered in these investigations.

Chapter 8

Summary

Ice interfaces are ubiquitous in nature, but their molecular structure is hardly understood. The high vapor pressure of ice close to the melting point renders the use of UHV techniques impossible or very difficult. Surfaces of ice are also very dynamic at temperatures close to the melting point. In addition, it is very difficult to prepare ice surfaces and stabilize them at ambient conditions. Considering all these difficulties it is not surprising that the structural behavior of ice at temperatures close to the melting point is still not well understood.

Some solids are known to show surface melting (also called premelting) on at least some of their facets. Surface melting describes the disordering of the surface layers as the temperature of the solid approaches the melting point. The temperature, at which premelting sets in is called the *onset temperature*. The thickness of the disordered region increases with temperature and diverges at the bulk melting point. The properties of this disordered region, which are possibly modified by remnants of the crystalline structure and strong confinement, are not known. Since the premolten region is not expected to exhibit bulk-like properties, it is called a *quasi-liquid layer*. The force acting between the interfaces on both sides of the quasi-liquid layer determines the thickness of the layer. Depending on spatial decay of this forces the quasi-liquid layer growths with a logarithmic (short-range forces) or an algebraic growth law (long-range forces).

Surface melting of ice was first described in 1860 by Michael Faraday [1]. Since then, many additional experiments were performed to investigate the surface melting of ice with different methods. The existence of surface melting of ice is an accepted scientific fact. However, a full understanding is still missing due to the difficulties encountered in the investigation of free surfaces of ice. Different techniques and different research groups give very different values for the thickness of the quasi-liquid layer at a certain temperature.

Much less is known about deeply buried ice-solid interfaces. Only very few experimental techniques can probe this type of interfaces. In this work high energy x-ray reflectivity is employed to overcome the penetration problem. In x- ray reflectivity measurements the intensity of an x-ray beam that is reflected from an interface is measured as a function of the momentum transfer perpendicular to the interface. The shape of the reflectivity curve depends on the electron density profile perpendicular to the interface. Inversion formalisms, such as the Parratt and master formalism, allow to deduce the electron density profile from the measured data. X-ray reflectivity is most commonly used at medium energies up to 20 keV. In order to access deeply buried interfaces higher energy x-rays are required due to their higher penetration depth.

High energy x-ray reflectivity experiments require very high positional and angular accuracy and stability of the sample and the detector. A dedicated end-station for high energy x-ray surface and interface diffraction has been installed recently at the *European Synchrotron Radiation Facility* (ESRF)[2]. The instrument allows to follow the reflectivity to large momentum transfer values which is necessary to achieve molecular resolution. Since the reflectivity is decaying very fast at large momentum transfer values, particular attention was put to the suppression of background. This was achieved by focusing the primary x-ray beam to spot sizes of several microns, thus reducing bulk background scattering into the solid angle of the detector. With these methods the detection of up to 10 orders of magnitude of reflectivity became possible. The high brilliance required for these experiments was provided by the high energy beamline ID15 at the ESRF.

The interfaces investigated by this technique must be of very high quality with a microscopic and uncorrelated roughness well blow 10 Å. The surface of the substrate has to be completely flat. The ice has to be of similar quality. The use of polycrystalline ice was abandoned because it was not possible to produce ice samples with sufficient purity and reproducible quality. For this reasons ice single crystals were used. The crystals were provided by Jörg Bilgram (ETH Zürich). A special bonding technique is used to melt the substrate into the ice. In this way the crystalline properties of the ice interface are defined in the most reproducible way and retain most of the structure of the single crystal.

Interface melting of ice in contact with naturally grown SiO_2 on silicon (111) and (100) surfaces was studied by Simon Engemann et al. with high energy x-ray reflectivity [3]. The presence of interface melting could be confirmed. The quasi-liquid layer revealed a surprisingly high density of $1.2\rho_{water}$ and grows with a logarithmic growth law. The work presented in this thesis is based on this investigation. Different substrates were employed to shed light on the influence of the chemical and morphological properties on the interface melting.

In total, eleven samples were measured for this work. Interface melting could be observed clearly only in two cases. In the other cases it was not observed, but can not be excluded, since a quasi-liquid layer can only be detected by x-ray reflectivity if its electron density is different from the electron density of the two surrounding substrates. In some cases the quality of the obtained data was not high enough to exclude the presence of a premolten layer of different density.

The substrates for the interfaces that showed interface melting were single crystalline quartz and fused silica. Fused silica is a high purity glass. In both cases the quasi-liquid layer has a density of $1.25\rho_{water}$, similar to the value obtained by Engemann et al. [3]. Irradiating the sample with high x-ray doses induced a growth of the thickness of the quasi-liquid layer. The reason for this radiation-induced growth is not known. The thickness of the premolten region increased by 11 Å per 10^9 Gy of radiation at the ice-silica interface. At the ice-quartz sample is radiation-induced growth rate is doubled. The layer thickness can be extrapolated to obtain the thickness for a non-irradiated interface. However, due to the large experimental errors for the rate of this radiation-induced growth, the corrected layer thicknesses have large errors.

Due to the errors make it is not possible to conclude from the data whether the thickness follows a logarithmic or an algebraic growth law. Since a logarithmic growth law was obtained in previous experiments, the thickness was assumed to follow the growth law

$$L = \xi \ln \left(\frac{T_O}{(T_M - T)} \right) , \tag{8.1}$$

with the correlation length ξ, the onset temperature T_O and the bulk melting point T_M. For the silica sample $\xi_{silica} = 5$ Å and $T_{O,silica} = -9$ °C are obtained. The correlation length of the quartz sample is slightly higher, with $\xi_{quartz} = 7$ Å. The onset temperature is $T_{O,quartz} = -1$ °C, significantly higher than for the silica sample. This indicates that the structure of the substrate influences the properties of the quasi-liquid layer. The crystalline surface of the quartz has a stabilizing effect on the crystal lattice of the ice, suppressing the formation of a disordered quasi-liquid layer. When premelting sets in a higher correlation length is observed for the quasi-liquid layer in contact with the crystalline substrate.

An interesting fact is that all the x-ray reflectivity studies on premelting with show consistently the same high density for the quasi-liquid layer. This density is similar to the density of very-high-density amorphous ice (VHDA, $\rho_{VHDA} = 1.25\rho_{water}$). A density increase of this magnitude can not be explained by stress or impurities. We conclude therefore that the water molecules inside the premolten region form a high density water phase. Confined water phases of high density have also been found in zeolites [5]. The fact that the density is similar to VHDA indicates that the quasi-liquid layer has a similar structure. Some water models assume that water has a second critical point at low temperatures. Below this temperature two different phases, a high density phase (HDW) and a low density phase (LDW), might exist. Consequently, water observed at ambient conditions exhibits large fluctuations between these two phases. This gives rise to speculations whether it would be possible to stabilize the high density water phase in confinement. The x-ray reflectivity results on the interface melting of ice could be interpreted in this way.

The weak point of this investigation is that it was not possible to reproduce the results. Many of the interfaces clearly did not show interface melting even when the same substrate was used. For example, a second ice-silica sample was investigated. This interface was identical to the one described above, but did not show any signs of interface melting. This leads to the conclusion that the sample preparation is not reproducible enough. In addition, the ice-silica interface, where premelting was observed, was investigated again five months later. In this experiment no quasi-liquid layer could be detected. In order to exclude spatial inhomogeneities resulting from the sample preparation the experiment was performed at exactly the same spot on the interface. The probing spot of the previous experiment could be identified by the radiation damage in the ice. The only explanation for this result is that there are additional parameters controlling the premelting. Unfortunately, the nature of these parameters remains opaque. The experiments performed at the ice-silica interfaces proof that these parameters (or some of them) are time-dependent.

This time-dependent suppression of premelting could therefore be explained by the mobility of the water molecule. It is reasonable to assume that the water molecules in the ice lattice need a certain mobility to form the structurally different quasi-liquid layer. At natural interfaces this is always possible due to the high amount of impurities and structural disorder such as roughness. In the samples used for this work, the interfaces are almost perfect. However, some disorder is created by the sample preparation, when the substrate is molten into the ice. This additional strain and disorder could in combination with the radiation damage lead to the formation of a quasi-liquid layer in some samples. In addition the samples were kept 16 K below their melting point for extended periods of time. This annealing could relax the lattice in to a more ordered state between the two x-ray experiments performed at the ice-silica interface. This would explain why no premelting could be measured after annealing the sample for a long time.

It is clear from the results of this work that additional investigations have to be performed in order to understand the interface melting of ice. It is most important to find better ways to prepare the interfaces. This might be achieved by deposition of water molecules from the vapor phase. It is also important to reduce the x-ray radiation dose on the sample. Since radiation damage contributes the strongest uncertainties to the measurements, non-irradiative techniques should be combined with the synchrotron measurements. Additional insight might be gained from experiments performed at the interface between ice and organic liquids, such as heptane. Since the density of ice is higher than the density of heptane it is possible to produce an evanescent wave inside the ice surface. These would allow the investigation of the ice interface structure by grazing incidence experiments. Investigations of the ice-vapor interface suffer from sublimation and condensation of water on the surface. These artifacts would be suppressed in the presence of a hydrophobic organic liquid.

Appendix A

Derivation of the master formula

Figure A.1 shows a single slab illuminated by a x-ray beam. The reflectivity of a single slab is the sum of the reflectivity for rays reflected from the top interface (amplitude reflectivity $r_{t\downarrow}$) and rays transmitted from the top interface (transmittivity $t_{t\downarrow}$) and reflected from the bottom interface (reflectivity $r_{b\downarrow}$). If the wave is then transmitted by the top interface (transmittivity $t_{t\uparrow}$) it is added to the reflected wave field with the phase factor $\phi = e^{iQz_0}$ yielding a reflectivity of

$$r_1 = t_{t\downarrow} r_{b\downarrow} t_{t\uparrow} \phi, \tag{A.1}$$

z_0 being the thickness of the slab and $Q = \frac{4\pi}{\lambda} \sin\theta$. The index of r denotes that the wave has been reflected once from the bottom interface. If the wave is not transmitted through the top interface it is reflected again (reflectivity $r_{t\uparrow}$). In this case it will contribute to the reflectivity as

$$r_2 = t_{t\downarrow} r_{b\downarrow} r_{t\uparrow} r_{b\downarrow} t_{t\uparrow} \phi^2. \tag{A.2}$$

The total reflectivity of the interface is the sum of the reflectivity coefficients for all the multiply reflected waves

$$\begin{aligned} r &= r_0 + r_1 + r_2 + \ldots \\ &= r_{t\downarrow} + t_{t\downarrow} r_{b\downarrow} t_{t\uparrow} \phi + t_{t\downarrow} r_{b\downarrow} r_{t\uparrow} r_{b\downarrow} t_{t\uparrow} \phi^2 + \ldots \\ &= r_{t\downarrow} + t_{t\downarrow} r_{b\downarrow} r_{t\uparrow} \sum_{i=0}^{\infty} \left(r_{t\uparrow} r_{b\downarrow} \phi \right)^i . \end{aligned} \tag{A.3}$$

This is a geometric series, which can be rewritten as

$$r = r_{t\downarrow} + t_{t\downarrow} r_{b\downarrow} t_{t\uparrow} \frac{\phi}{1 - r_{t\uparrow} r_{b\downarrow} \phi}. \tag{A.4}$$

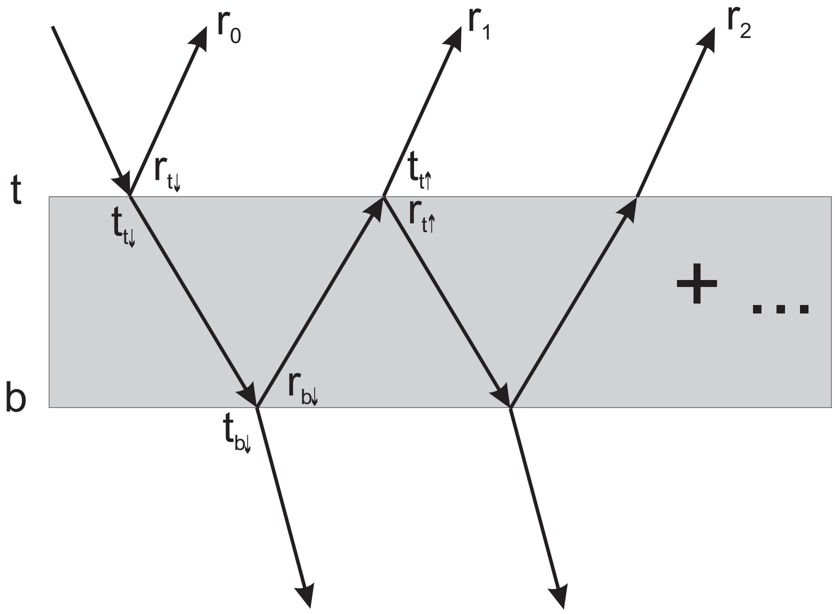

Figure A.1: Derivation of the master formula. The total reflectivity is the sum of the reflectivities r_0, r_1, r_2, etc. . $r_0 = r_{t\downarrow}$ is the contribution from the wave reflected at the top interface. $r_1 = t_{t\downarrow} r_{b\downarrow} t_{t\uparrow} \phi$ is the contribution from the wave transmitted through the top interface, reflected at the bottom and transmitted through the top. It is added to the wave r_1 with a phase factor $\phi = e^{iQz_0}$.

Using Fresnel's equations (see Eqs. 3.18 and 3.19) it follows that

$$r_{t\uparrow} = \frac{n_2 \sin\theta' - n_1 \sin\theta}{n_1 \sin\theta + n_2 \sin\theta'} = -1 \cdot \frac{n_1 \sin\theta - n_2 \sin\theta'}{n_1 \sin\theta + n_2 \sin\theta'} = -r_{t\downarrow} \tag{A.5}$$

and

$$r_{t\downarrow}^2 + t_{t\downarrow} t_{t\uparrow} = \frac{(n_1 \sin\theta - n_2 \sin\theta')^2}{(n_1 \sin\theta + n_2 \sin\theta')^2} + \frac{2n_1 \sin\theta \, 2n_2 \sin\theta'}{(n_1 \sin\theta + n_2 \sin\theta')^2} = 1. \tag{A.6}$$

Eq. A.4 can then be simplified to

$$r = \frac{r_{t\downarrow} + r_{b\downarrow}\phi}{1 + r_{t\downarrow} r_{b\downarrow}\phi}. \tag{A.7}$$

In order to calculate the reflectivity from an arbitrary dispersion profile the reflectivity of an infinitesimal slab ($z_0 \to 0$) is needed. For a continuous dispersion profile this also implies that the index of refraction on both sides of the slab is approximately the same and that $r_{t\downarrow} \approx -r_{b\downarrow}$. This simplifies Eq. A.7 further to

$$r = \frac{r_{t\downarrow}(1-\phi)}{1 - r_{t\downarrow}^2 \phi}. \tag{A.8}$$

Since the kinematical approximation is only valid for large angles we will further assume that the momentum transfer is large. This implies that $r_{t\downarrow} \ll 1$ and $r_{t\downarrow}$ can be expressed by the approximation of the Fresnel reflectivity given in Eq. 3.23. Using these approximations one finds

$$r = \left(\frac{\theta_c}{2\theta}\right)^2 (1-\phi) = \left(\frac{Q_c}{2Q}\right)^2 \left(1 - e^{iQz_0}\right) = -i\left(\frac{Q_c^2 z_0}{4Q}\right)\left(\frac{\sin\zeta}{\zeta}\right)e^{\zeta}, \quad \text{(A.9)}$$

with $\zeta = \frac{Qz_0}{2}$. The final expression for the infinitesimal slab ($\zeta \rightarrow 0$) is

$$dr \approx -i\frac{Q_c^2\, dz}{4Q}. \quad \text{(A.10)}$$

The dispersion profile of the interface is described by the dispersion function $\delta(z)$. The reflectivity of each individual slice is (using Eq. A.10)

$$dr(Q) = \frac{-i}{\delta_{-\infty} - \delta_{+\infty}}\left(\frac{Q_c^2}{4Q}\right)\delta(z)dz. \quad \text{(A.11)}$$

The factor at the front is for normalisation. Integrating A.11 while taking into account the correct phases $\phi = e^{iQz}$ leads to

$$r(Q) = \frac{-i}{\delta_{-\infty} - \delta_{+\infty}}\left(\frac{Q_c^2}{4Q}\right)\int \delta(z)e^{iQz}dz. \quad \text{(A.12)}$$

After partial integration this can be rewritten as

$$r(Q) = \frac{-i}{\delta_{-\infty} - \delta_{+\infty}}\left(\frac{Q_c^2}{4Q}\right)\left(\frac{-1}{iQ}\right)\int \frac{d\delta(z)}{dz}e^{iQz}dz. \quad \text{(A.13)}$$

Using the Fresnel reflectivity $r_f = \left(\frac{Q_c}{2Q}\right)^2$ the reflected *intensity* in the master formula is obtained

$$R(Q) = \frac{R_F(Q)}{\delta_{-\infty} - \delta_{+\infty}}\left|\int \frac{d\delta(z)}{dz}e^{iQz}dz\right|^2. \quad \text{(A.14)}$$

Appendix B

List of abbreviations

AFM atomic force microscopy

CRL compound refractive lenses

DLP method Dzyaloshinskii-Lifshitz-Pitaevskii method

DSC differential scanning calorimetry

ESRF European Synchrotron Radiation Facility

FAS fluoroalkylsilane

FCC face centered cubic

FWHM full width half maximum

GAXS glancing angle x-ray scattering

HEMD High Energy MicroDiffractometer

ID insertion device

MBE molecular beam epitaxy

MPG/MPI Max Planck Society / Max Planck Institute

OTS octadecyl-trichlorosilane

QLL quasi-liquid layer

SAM self assembled monolayer

UHV ultra high vacuum

UV ultra-violet

XRR x-ray reflectivity

Appendix C

Symbols used in equations

A area

c speed of light

D radiation dose

E energy

$\vec{E}$ electric field vector

f free energy per area or form factor

I intensity

$\vec{k}$ wave vector

L thickness of the quasi-liquid layer

M_{mol} molar mass

N_A Avogadro's number ($6.0221367 \cdot 10^{23}$ 1/mol)

n index of refraction

n_a number density

$\vec{Q}$ momentum transfer

Q_c critical momentum transfer

Q_m latent heat of melting

R Reflection coefficient

r reflectivity

r_e classical electron radius ($2.81794092 \cdot 10^{-15}$ m)

r_f Fresnel reflectivity

s_{ij} elastic compliances

T Temperature or transmission coefficient

T_M Melting point of water

T_O Onset temperature

Z atomic number

β imaginary part of the index of refraction for x-rays ($i\beta = n - 1 + \delta$)

δ real part of the index of refraction for x-rays ($\delta = 1 - n + i\beta$)

γ interface free energy per area

χ asymmetric crystal cut

λ wavelength

Ω solid angle

φ integrated flux

Φ photon flux

ρ density

ρ_e electron density or bending radius

σ roughness

τ lifetime

θ angle

θ_c critical angle

ξ correlation length

Bibliography

[1] M. Faraday. Note on regelation. *Proceedings of the Royal Society of London*, 10:440–451, 1860.

[2] J. Okasinski, H. Reichert, V. Honkimäki, and H. Dosch. A high energy microdiffractometer. To be published.

[3] S.C. Engemann. *Premelting at the ice-SiO$_2$ interface. A high-energy x-ray microbeam diffraction study*. PhD thesis, Universität Stuttgart, 2005.

[4] T. Loerting, C. Salzmann, I. Kohl, E. Mayer, and A. Hallbrucker. A second distinct structural ”state” of high-density amorphous ice at 77 k and 1 bar. *Physical Chemistry Chemical Physics*, 3:5355–5357, 2001.

[5] N. Floquet, J.P. Coulomb, N. Dufau, and G. Andre. Structure and dynamics of confined water in AlPO$_4$-5 zeolite. *Journal of Physical Chemistry B*, 108:13107–13115, 2004.

[6] P.H. Poole, F. Sciortino, U. Essmann, and H.E. Stanley. Phase behaviour of metastable water. *Nature*, 360:324–328, 1992.

[7] W.S. Benedict, N. Gailar, and E.K. Plyler. Rotation-vibration spectra of deuterated water vapor. *Journal of Chemical Physics*, 24:1139–1165, 1956.

[8] S.A. Clough, Y. Beers, G.P. Klein, and L.S. Rothman. Dipole moment of water from Stark measurements of H_2O, HDO, and D_2O. *Journal of Chemical Physics*, 59:2254–2259, 1973.

[9] V.F. Petrenko and Robert W. Whitworth. *Physics of Ice*. Oxford University Press, 1999.

[10] B. Winter and M. Faubel. Photoemission from liquid aqueous solutions. *Chemical Reviews*, 106:1176–1211, 2006.

[11] G. Tammann. Ueber die Grenzen des festen Zustandes IV. *Annalen der Physik*, 2:1–31, 1900.

[12] L. Pauling. The structure and entropy of ice and other crystals with some randomness of atomic arrangement. *Journal of the American Chemical Society*, 57:2680, 1935.

[13] W.F. Giauque and M.F. Ashley. Molecular rotation in ice at 10 K. Free energy of formation and entropy of water. *Physical Review*, 43:81, 1933.

[14] S. Kawada. Dielectric dispersion and phase transition of KOH doped ice. *Journal of the Physical Society of Japan*, 32:1442, 1972.

[15] C.M.B. Line and R.W. Whitworth. A high resolution neutron powder diffraction study of D2O ice XI. *Journal of Chemical Physics*, 104:10008–10013, 1996.

[16] S.M. Jackson, V.M. Nield, R.W. Whitworth, M. Oguro, and C.C. Wilson. Single-crystal neutron diffraction studies of the structure of ice XI. *Journal of Physical Chemistry B*, 101:6142–6145, 1997.

[17] I.A. Ryzhkin and V.F. Petrenko. Phase transition of an ice-proton system into a bernal-fowler state. *Physical Review B*, 62:11280–11283, 2000.

[18] N. Bjerrum. Structure and properties of ice. *Kongelige Danske Videnskabernes Selskab Matematisk-fysiske Meddelelser*, 27:1, 1951.

[19] R. Podeszwa and V. Buch. Structure and dynamics of orientational defects in ice. *Physical Review Letters*, 83(22):4570–4573, Nov 1999.

[20] N. Grishina and V. Buch. Structure and dynamics of orientational defects in ice I. *Journal of Chemical Physics*, 120(11):5217–5225, 2004.

[21] F.C. Frank. Descartes' observations on the Amsterdam snowfalls of 4, 5, 6 and 9 February 1635. *Journal of Glaciology*, 13:535–539, 1974.

[22] V.F. Petrenko. The effect of static electric fields on ice friction. *Journal of Applied Physics*, 76(2):1216–1219, 1994.

[23] V.F. Petrenko and Samuel C. Colbeck. Generation of electric fields by ice and snow friction. *Journal of Applied Physics*, 77(9):4518–4521, 1995.

[24] N.H. Fletcher. Reconstruction of ice crystal surfaces at low temperatures. *Philosophical Magazine B*, 66:109–115, 1992.

[25] H. Dosch, A. Lied, and J. H. Bilgram. Disruption of the hydrogen-bonding network at the surface of Ih ice near surface premelting. *Surface Science*, 366:43–50, 1996.

[26] J.F. van der Veen, B. Pluis, and A.W. Denier van der Gon. Surface melting. In *Chemistry and physics of solid surfaces VII*. Springer Verlag, 1988.

[27] J.G. Dash. Surface melting. *Contemporary Physics*, 30:89–100, 1989.

[28] B. F. Henson and J. M. Robinson. Dependence of quasiliquid thickness on the liquid activity: A bulk thermodynamic theory of the interface. *Physical Review Letters*, 92(24):246107, 2004.

[29] F.A. Lindemann. Ueber die Berechnung molekularer Eigenfrequenzen. *Physikalische Zeitschrift*, 11:609, 1910.

[30] M. Ross. Generalized Lindemann melting law. *Physical Review*, 184(1):233–242, Aug 1969.

[31] A. Lied, H. Dosch, and J.H. Bilgram. Surface melting of ice I_h single crystals revealed by glancing angle x-ray scattering. *Physical Review Letters*, 72(22):3554–3557, May 1994.

[32] J. S. Wettlaufer. Impurity effects in the premelting of ice. *Physical Review Letters*, 82(12):2516–2519, Mar 1999.

[33] N.H. Fletcher. Surface structure of water and ice. *Philosophical Magazine*, 7:255–269, 1962.

[34] M. Elbaum and M. Schick. Application of the theory of dispersion forces to the surface melting of ice. *Physical Review Letters*, 66:1713–1716, 1991.

[35] L. A. Wilen, J. S. Wettlaufer, M. Elbaum, and M. Schick. Dispersion-force effects in interfacial premelting of ice. *Physical Review B*, 52(16):12426–12433, Oct 1995.

[36] L. Makkonen. Surface melting of ice. *Journal of Physical Chemistry B*, 101:6196–6200, 1997.

[37] B.F. Henson, L.F. Voss, K.R. Wilson, and J.M. Robinson. Thermodynamic model of quasiliquid formation on h_2o ice: Comparison with experiment. *Journal of Chemical Physics*, 123:144707, 2005.

[38] I.A. Ryzhkin and V.F. Petrenko. Violation of ice rules near the surface: A theory for the quasiliquid layer. *Physical Review B*, 65:012205, 2001.

[39] T.A. Weber and F.H. Stillinger. Molecular dynamics study of ice crystallite melting. *Journal of Physical Chemistry*, 87:4277–4281, 1983.

[40] G.-J. Kroes. Surface melting of the (0001) face of TIP4P ice. *Surface Science*, 275:365–382, 1992.

[41] H. Nada and Y. Furukawa. Anisotropy in structural transitions between basal and prismatic faces of ice studied by molecular dynamics simulation. *Surface Science*, 446:1–16, 2000.

[42] L. H. de la Pena, M. S. Gulam Razul, and P. G. Kusalik. Quantum effects in ice Ih. *The Journal of Chemical Physics*, 123(14):144506, 2005.

[43] J.F. van der Veen. Melting and freezing at surfaces. *Surface Science*, 433-435:1–11, 1999.

[44] J.G. Dash, H.Y. Fu, and J.S. Wettlaufer. The premelting of ice and its environmental consequences. *Report of Progress in Physics*, 58:115, 1995.

[45] B. Gruska and A. Röseler. UV-Vis-IR Ellipsometry (ELL). In *Surface and Thin Film Analysis*. Wiley-VCH, 2002.

[46] Y. Furukawa, M. Yamamoto, and T. Kuroda. Ellipsometric study of the transition layer on the surface of an ice crystal. *Journal of Crystal Growth*, 82:665–677, 1987.

[47] D. Beaglehole and P. Wilson. Extrinsic premelting at the ice-glass interface. *Journal of Physical Chemistry*, 98:8096–8100, 1994.

[48] Y.R. Shen. 1998 Frank Isakson Prize Address: Sum frequency generation for vibrational spectroscopy: Applications to water interfaces and films of water and ice. *Solid State Communications*, 108:399–406, 1998.

[49] X. Wei, P.B. Miranda, and Y.R. Shen. Surface vibrational spectroscopic study of surface melting of ice. *Physical Review Letters*, 86(8):1554–1557, Feb 2001.

[50] X. Wei, P.B. Miranda, C. Zhang, and Y.R. Shen. Sum-frequency spectroscopic studies of ice interfaces. *Physical Review B*, 66(8):085401, Aug 2002.

[51] G. Friedbacher. Scanning probe microscopy. In *Surface and Thin Film Analysis*. Wiley-VCH, 2002.

[52] V.F. Petrenko. Study of the surface of ice, ice/solid and ice/liquid interfaces with scanning force microscopy. *Journal of Physical Chemistry B*, 101:6276–6281, 1997.

[53] T. Eastman and D.-M. Zhu. Influence of an AFM tip on interfacial melting on ice. *Journal of Colloid and Interface Science*, 172:297–301, 1995.

[54] A. Döppenschmidt, M. Kappl, and H.-J. Butt. Surface properties of ice studied by atomic force microscopy. *Journal of Physical Chemistry B*, 102:7813–7819, 1998.

[55] A. Döppenschmidt and H.-J. Butt. Measuring the thickness of the liquid-like layer on ice surfaces with atomic force microscopy. *Langmuir*, 16:6709–6714, 2000.

[56] H.-J. Butt, A. Döppenschmidt, G. Hüttl, E. Müller, and O. I. Vinogradova. Measuring the thickness of the liquid-like layer on ice surfaces with atomic force microscopy. *Journal of Chemical Physics*, 113:1194–1203, 2000.

[57] H. Bluhm, T. Inoue, and M. Salmeron. Friction of ice measured using lateral force microscopy. *Physical Review B*, 61(11):7760–7765, Mar 2000.

[58] B. Pittenger, D. J. Cook, C. R. Slaughterbeck, and Jr. S. C. Fain. Investigation of ice-solid interfaces by force microscopy: Plastic flow and adhesive forces. *Journal of Vacuum Science and Technology A*, 16:1832–1837, 1998.

[59] C. R. Slaughterbeck, E. W. Kukes, B. Pittenger, D. J. Cook, P. C. Williams, V. L. Eden, and S. C. Fain, Jr. Electric field effects on force curves for oxidized silicon tips and ice surfaces in a controlled environment. *Journal of Vacuum Science and Technology A*, 14:1213–1218, 1996.

[60] B. Pittenger, S. C. Fain, M. J. Cochran, J. M. K. Donev, B. E. Robertson, A. Szuchmacher, and R. M. Overney. Premelting at ice-solid interfaces studied via velocity-dependent indentation with force microscope tips. *Physical Review B*, 63(13):134102, Mar 2001.

[61] V. Tsionsky, D. Zagidulin, and E. Gileadi. Evidence for the existence of a ”liquid-like layer” between a metal electrode and a frozen aqueous solution. *Journal of Physical Chemistry B*, 106:13089–13091, 2002.

[62] V. Tsionsky, L. Daikhin, D. Zagidulin, M. Urbakh, and E. Gileadi. The quartz crystal microbalance as a tool for the study of a ”liquidlike layer” at the ice/metal interface. *Journal of Physical Chemistry B*, 107:12485–12491, 2003.

[63] A. Kaverin, V. Tsionsky, D. Zagidulin, L. Daikhin, E. Alengoz, and E. Gileadi. A novel approach for direct measurement of the thickness of the liquid-like layer at the ice/solid interface. *Journal of Physical Chemistry B*, 108:8759–8762, 2004.

[64] H. Dosch, A. Lied, and J.H. Bilgram. Glancing-angle x-ray scattering studies of the premelting of ice surfaces. *Surface Science*, 327:145–164, 1995.

[65] S. Engemann, H. Reichert, H. Dosch, J. Bilgram, V. Honkimaeki, and A. Snigirev. Interfacial melting of ice in contact with SiO_2. *Physical Review Letters*, 92(20):205701, 2004.

[66] M. Rauscher, H. Reichert, S. Engemann, and H. Dosch. Local density profiles in thin films and multilayers from diffuse x-ray and neutron scattering. *Physical Review B*, 72(20):205401, 2005.

[67] R.R. Gilpin. Wire regelation at low temperatures. *Journal of Colloid and Interface Science*, 77:435–448, 1980.

[68] I. Golecki and C. Jaccard. Intrinsic surface disorder in ice near the melting point. *Journal of Physics C: Solid State Physics*, 11:4229–4238, 1978.

[69] L. Palmetshofer. Rutherford back-scattering spectroscopy (RBS). In *Surface and Thin Film Analysis*. Wiley-VCH, 2002.

[70] H. Bluhm, D.F. Ogletree, C.S. Fadley, Z. Hussain, and M. Salmeron. The premelting of ice studied with photoelectron spectroscopy. *Journal of Physics: Condensed Matter*, 14:L227–L233, 2002.

[71] H. Bubert and J.C. Rivière. Photoelectron spectroscopy. In *Surface and Thin Film Analysis*. Wiley-VCH, 2002.

[72] V. Sadtchenko and G.E. Ewing. Interfacial melting of thin ice films: An infrared study. *Journal of Chemical Physics*, 116:4686–4697, 2002.

[73] C. Faivre, D. Bellet, and G. Dolino. Melting and freezing of water in ordered mesoporous silica materials. *European Physical Journal B*, 7:19–36, 1999.

[74] A. Schreiber, I. Ketelsen, and G.H. Findenegg. Melting and freezing of water in ordered mesoporous silica materials. *Physical Chemistry - Chemical Physics*, 3:1185–1195, 2001.

[75] J.G. Dash, A.W. Rempel, and J.S. Wettlaufer. The physics of premelted ice and its geophysical consequences. *Reviews of Modern Physics*, 78:695–741, 2006.

[76] A.A. Chernov, D.E. Temkin, and A.M. Mel’nikova. Theory of the capture of solid inclusions during the growth of crystals from the melt. *Soviet Physics - Crystallography*, 21:652–660, 1976.

[77] J.G. Dash. Thermomolecular pressure in surface melting: Motivation for frost heave. *Science*, 246:1591–1593, 1989.

[78] P. Jungwirth, D. Rosenfeld, and V. Buch. A possible new molecular mechanism of thundercloud electrification. *Atmospheric Research*, 76:190–205, 2005.

[79] J.G. Dash, B.L. Mason, and J.S. Wettlaufer. Theory of charge and mass transfer in ice-ice collisions. *Journal of Geophysical Research*, 106:20395–20402, 2001.

[80] D.C.B. Evans, J.F. Nye, and K.J.Cheeseman. The kinetic friction of ice. *Proceedings of the Royal Society of London A*, 347:493–512, 1976.

[81] S.C. Colbeck, L. Najarian, and H.B. Smith. Sliding temperatures of ice skates. *American Journal of Physics*, 65:488–492, 1996.

[82] J.J. de Koning, G. de Groot, and G.J. van Ingen Schenau. Ice friction during speed skating. *Journal of Biomechanics*, 25:565–571, 1992.

[83] M. Tolan. *X-Ray Scattering from Soft-Matter Thin Films*. Springer, 1999.

[84] J. Als-Nielsen and D. McMorrow. *Elements of Modern X-Ray Physics*. Wiley, 2001.

[85] ”National Institute of Standards and Technology”. X-ray form factor, attenuation and scattering tables. http://physics.nist.gov/PhysRefData/FFast/html/form.html.

[86] L. G. Parratt. Surface studies of solids by total reflection of x-rays. *Physical Review*, 95:359–369, 1954.

[87] S. Schöder, T. Wagner, H. Reichert, and H. Dosch. A novel method for the deposition of ultra-smooth metal films. To be published.

[88] H. Kuchling. *Taschenbuch der Physik*. Fachbuchverlag Leipzig, 1996.

[89] ”CrysTec Gmbh”. Crystec (supplier) data sheet. http://www.crystec.de.

[90] Center for X-ray Optics and Advanced Light Source. X-ray data booklet.

[91] V. Honkimäki, H. Reichert, J.S. Okasinski, and H. Dosch. X-ray optics for liquid surface/interface spectrometers. *Journal of Synchrotron Radiation*, 13:426–431, 2006.

[92] C. Schulze and D. Chapman. A program for the calculation of the reflectivity of cylindrically bent Laue crystal monochromators. *Review of Scientific Instruments*, 66:2220–2223, 1995.

[93] Ts-150 instruction manual.

[94] W. Press, S. Teukolsky, W. Vetterling, and B. Flannery. *Numerical Recipes in C*. Cambridge University Press, 1992.

[95] M. Mezger. *Diffuse Roentgenstreuung an Ni-Pa Legierungen*. PhD thesis, Universität Stuttgart, 2004.

[96] Y. Xie, F.F. Ludwig, G. Morales, D.E. Hare, and C.M. Sorensen. Noncritical behavoir of density fluctuations in supercooled water. *Physical Review Letters*, 71:2050–2053, 1993.

[97] L. Bosio, J. Teixeira, and H.E. Stanley. Enhanced density fluctuations in supercooled H_2O, D_2O and ethanol-water solutions: Evidence from small-angle x-ray scattering. *Physical Review Letters*, 46:597–600, 1981.

[98] J. Bilgram. Private communication.

Acknowledgments

I want to thank **Prof. Dr. Helmut Dosch** for accepting me as a student in his institute. Between all his meetings and conferences, he always found some time to discuss my newest data with him. This work benefited a lot from his experienced comments and advices. He was a great help for me to find and choose a new position after my PhD. My supervisor **Dr. Harald Reichert** always gave me the freedom to explore my research the way I wanted. I especially want to thank him for the very fast and accurate correction of my thesis. **Dr. Veijo Honkimki** co-supervised the thesis. I appreciated that he was always available for discussions. I want to thank **Prof. Dr. Jörg Wrachtrup** for accepting to do the second exam on short notice. I also want to thank **Prof. Dr. Ulrich Weiß** for accepting to chair the defense.

This thesis was based on the work done by **Dr. Simon Engemann**. His scientific results were a starting point for my work and I was able to use the experimental chamber that he designed. In addition, he taught me how to work in the cold room and at the beamline. The ice single crystals provided by **Prof. Dr. Jörg Bilgram** were fundamental for this work.

I especially want to thank my colleagues **Dr. John Okasinski**, **Heiko Schröder**, **Dr. Markus Mezger**, **Dr. Sandrine Dourdain**, **Dr. Federica Venturini** and **Sebastian Schramm**, who worked long shifts with me on the beamline. They were not only necessary for running the experiment but also for making it an enjoyable experience. Aside from helping out in the middle of the night, John also provided great help in the setup of the experiments and ensured the running of the instrument. Surely, without the dedication of the BLOMs (BeamLine Operation Manager) **Dr. Marco di Michiel** and **Dr. Thomas Buslaps** not a single x-ray photon would have ever hit our samples. The beamline technicians, **Mogens Kretzschmer** and **Anthony Mauro** were very helpful in setting up and running the experiment. I want to thank **Annette Weißhardt** and **Dr. Harald Müller** for their help with all chemical questions and setups. **Frank Adams** provided valuable support for all experiments done with the MPI x-ray lab sources. The construction, maintenance and modification of the experimental chambers was only possible with the help of **Michael Schäfer** (ITAP mechanics workshop) and

Helmut Kammerlander (MPI glass workshop) and their teams.

I want to thank my friendly colleagues of the department Dosch, who I always missed when leaving the institute after a short sample preparation stay. I especially want to thank my office mates **Dr. Ingo Ramsteiner** and **Dr. Alina Vlad** who made my stay agreeable and helped me with my work at the MPI. In addition, I had many fruitful discussions with Ingo and learned a lot from him. I enjoyed my time as part of the ID15 group very much and want to thank the team (**Dr. John Daniels**, **Dr. Kieran Drake**, **Dr. Gabriela Gonzalez Aviles**, **Dr. Nozumo Hiraoka**, **Dr. Matthew Peel** and **Dr. Diego Pontoni** in addition to the people already mentioned) for their support and their friendship.

Lastly, I want to thank my parents, who always supported me and my decision to take a path in science. In addition, I want to thank **Anne-Marie Bourgeois** for her help and support when I had to deal with French authorities and regulations.